THEORETICAL STUDIES OF AMORPHOUS AND PARACRYSTALLINE SILICON

A dissertation presented to

the faculty of

the College of Arts and Sciences of Ohio University

In partial fulfillment

of the requirements for the degree

Doctor of Philosophy

Serge Nakhmanson

March 2001

THEORETICAL STUDIES OF AMORPHOUS AND PARACRYSTALLINE SILICON

BY

SERGE NAKHMANSON

This dissertation has been approved

for the Department of Physics and Astronomy

and the College of Arts and Sciences by

David A. Drabold
Associate Professor of Physics

Leslie A. Flemming
Dean, College of Arts and Sciences

Nakhmanson, Serge, Ph.D. March 2001. Physics

Theoretical Studies of Amorphous and Paracrystalline Silicon. (190 pp.)

Director of Dissertation: David A. Drabold

Until recently, structural models used to represent amorphous silicon (a-Si) in computer simulations were either perfectly fourfold connected random networks or random networks containing only miscoordinated atoms. These models are *an approximation* to the structure of the real material and do not uniformly comply with all the experimental data for a-Si. In this dissertation we make an attempt to go beyond this approximation and construct and examine models that have two major types of defects, encountered in real material, in their structure — nanovoids and crystalline grains.

For our study of voids in a-Si we have calculated vibrational properties of structural models of a-Si with and without voids using *ab initio* and empirical molecular dynamics techniques. A small 216 atom and a large 4096 atom continuous random network (CRN) models for a-Si have been employed as starting points for our a-Si models with voids. Our calculations show that the presence of voids leads to an emergence of localized low-energy states in the vibrational spectrum of the model system. Moreover, it appears that these states are responsible for the anomalous behavior of system's specific heat at very low temperatures. To our knowledge these are the first numerical simulations that provide adequate agreement with experiment for the very low-temperature properties of specific heat in disordered materials *within* the limits of harmonic approximation.

For our study of crystalline grains in a-Si we have developed a new procedure for the preparation of physically realistic models of paracrystalline silicon based on a modification of the bond-switching method of Wooten, Winer, and Weaire. Our models contain randomly oriented c-Si grains embedded in a disordered matrix. Our technique creates interfaces between the crystalline and disordered phases of Si with an extremely low concentration of coordination defects. The resulting models possess structural and vibrational properties comparable with those of good CRN models of a-Si and display realistic optical properties, correctly reproducing the electronic bandgap of a-Si. The largest of our models also shows the best agreement of any atomistic model structure with fluctuation microscopy experiments, indicating that this model has a degree of medium-range order closest to that of the real material.

Approved: David A. Drabold

Associate Professor of Physics

ACKNOWLEDGMENTS

My deepest gratitude goes to my parents, who have always supported me and believed in me, and to my lovely wife Catherine, who makes me want to be the best that I can be.

I would also like to acknowledge the professors and researchers at St-Petersburg State University, Russia, and especially my direct scientific advisors — Prof. I. V. Abarenkov and Dr. I. Tupitsyn. They have trained and taken care of me and without them my following professional growth would have been impossible.

I also wish to thank my friends and colleagues whom I've met here in Athens, Ohio, and all over the world, people who donated their results, professional expertise and friendly advice to this dissertation: Dr. Normand Mousseau, Dr. Gerard Barkema and Dr. Paul Voyles who collaborated with me on my paracrystalline silicon project, Dr. Jianjun Dong who granted me his friendship at the time when I was just starting my career at Ohio University and needed it the most, Mr. Richard Vink who made an excellent empirical potential we employed in our molecular dynamics code. I'm grateful to Dr. W. Kamitakahara, Dr. S. Roorda, Dr. M. M. J. Treacy and Dr. J. M. Gibson who provided experimental data for this dissertation.

I want to thank the faculty and staff of the Department of Physics and Astronomy at Ohio University, their constant help and support made all these years I've spent here one of the best experiences in my life.

Finally I wish to thank my scientific advisor Dr. David A. Drabold for his care,

friendship and knowledge that he generously shared with me. Under his guidance I have turned from an apprentice to a real professional.

I'm also grateful for financial support from Ohio University and the National Science Foundation during my Ph.D. program.

Contents

List of Tables

List of Figures

Chapter 1

Introduction

1.1 Why we study amorphous silicon

Amorphous silicon remains at the center of attention of modern amorphous/glassy solid state physics community for two main reasons. First, this material — mostly in its hydrogenated and doped forms — is technologically important. Thin film transistors (TFT) made from a-Si:H are commonly found in today's electronic devices, for example, in liquid crystal flat panel displays. Other possible applications of a-Si include light sensors, microchips and solar cells — see R. A. Street's book[1] for more details.

The second reason, which is of main interest to solid state theory and computer simulation scientists, is that amorphous silicon is *one of the simplest systems* readily available to test new theoretical and simulation techniques and methods, some of which are developed especially for disordered systems. The advantages of using a-Si in particular as a model system for a disordered solid include

- a-Si being an elemental material, which makes it easier to study than binary compounds like a-GaAs or a-SiO_2,
- to a certain level of abstraction, bonds in a-Si can be considered as formed exclusively by sp^3-hybridized electron orbitals, which is also a benefit compared, for example, to a-C where numerous bonding types do exist: sp^2, sp^3 and even sp,
- a-Si forms a rigid overconstrained network, the dynamics of which can be adequately described by simple empirical 2 + 3 body potentials. A counterexample here can be a-Se that forms a network mostly consisting of weekly interacting strings that remain floppy and thus require a more advanced treatment for the calculation of interatomic forces — namely an *ab initio* method,
- an abundance (in certain fields) of experimental data for a-Si making the comparison of material properties, derived from theory or simulation, to experiment easy,
- some excellent quality atomistic models for a-Si have been recently created, which can serve as a good starting point in many theoretical or computational investigations of the properties of this material —

all of these items make a-Si an excellent "testing ground" for studies of numerous *generic* properties of amorphous and glassy materials.

The focus of this dissertation is mostly on the last item of the list presented

above: investigation of the properties of existing topological models for a-Si, study of strengths and weaknesses of their preparation methods and, most important, improvement of the models to make them resemble the real material more closely.

1.2 Beyond the continuous random network model

Up until recently, practically all the structural models for a-Si were of "continuous random network" (CRN) type. If we consider the diamond crystal, where all the interatomic distances and angles are exactly the same for all atoms (i.e. long range order is present) and only six- and eight-membered rings are allowed in the network, as a perfectly ordered case, then the difference between it and the CRN is that in the latter the disorder in bond-lengths and bond-angles is introduced and the odd-membered rings are allowed to form. A system like this has no periodicity and the long range order in it is broken while some kind of "local order" remains because for every atom it is still most energetically favorable to have four bonds, with length of the bonds and angles between them close to the crystalline values. Both crystalline silicon and CRN amorphous silicon structural models are shown in Fig. 1.1.

It has been confirmed by numerous experiments that the CRN model can successfully represent some major topological and other features of a disordered tetrahedrally bonded material[2, 3, 4] but obviously the CRN is *an approximation* and the structure of the real material is much more complicated. Experiments show that in addition to dangling bonds and other "atomic miscoordination" defects[5, 6] a-Si network

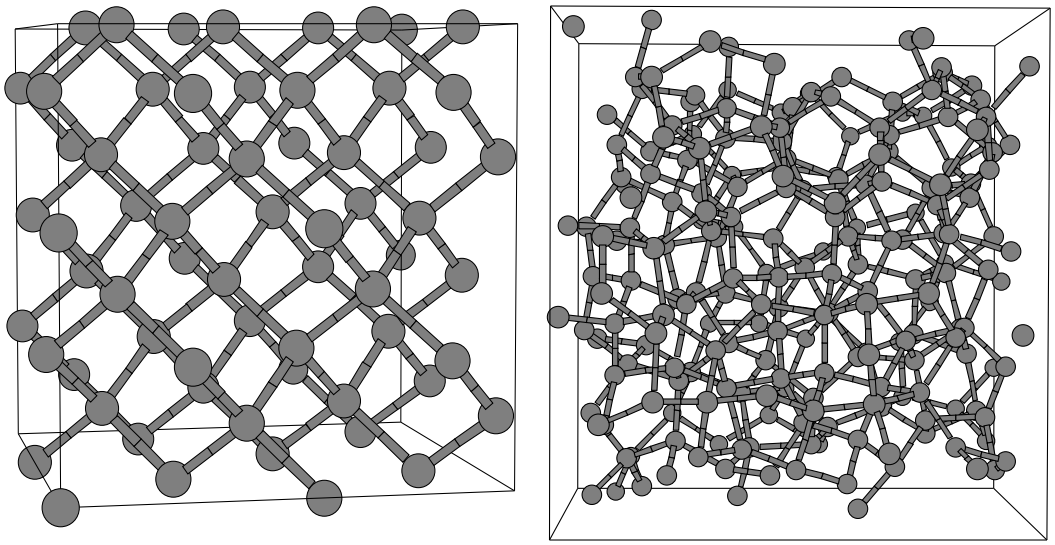

Figure 1.1: **Crystalline Si and CRN amorphous Si models. Left: 64 atom model of crystalline silicon; right: 216 atom CRN model of amorphous silicon.**

— depending on the preparation procedure of a given experimental sample — can also contain two more complicated types of defects, namely voids[7, 8, 9] of tens to hundreds of angstroms in diameter and crystalline grains (paracrystallites)[10, 11]. Usually, a certain fraction of miscoordination defects is present in the CRN models, which are well studied, so that in this dissertation we will not be particularly interested in modeling and studying the properties of this type of defect. Instead we will concentrate our attention on the two latter types — voids and crystalline grains — which are not naturally present in the CRN models and require special modeling techniques to be introduced into them, thus taking our a-Si models *beyond* the CRN approximation.

1.2.1 Voids in amorphous silicon

In the fourth chapter of this dissertation we will construct models containing hydrogenated and unhydrogenated voids in a-Si and study their vibrational properties. As we will show, the presence of voids leads to an emergence of new vibrational states in the phonon spectrum of our model systems. These states are spatially localized — on voids or in a string-like fashion between voids and strained parts of the network — and have rather low frequencies. The local nature of the states suggests that they, unlike "common" delocalized acoustic phonons, do not participate in heat conduction. The low energy (frequency) of the states rases the question of kinship of these states to the so called tunneling or two-level states[12, 13] — a theoretical construction used to explain anomalous (non-Debye) low-temperature specific heat and thermal conductivity behavior in glasses and amorphous materials. We will show that the void-associated localized low-energy states, though not being equivalent to tunneling states, also explain the deviation of low-temperature specific heat dependence from Debye's law.

1.2.2 Modeling of paracrystalline silicon

Recent state-of-the-art fluctuation electron microscopy experiments[10, 11] suggest that there are traces of order in as-deposited amorphous semiconductor thin films on the scale of approximately 10 Å. Structure at this length scale in Si is called medium-range order (MRO). The results of these experiments can be interpreted as indicating

the presence of topologically crystalline grains (10–30 Å in diameter) in the disordered network of amorphous material. As it is hard to verify this hypothesis experimentally, computer modeling can be used to create new models for a-Si that contain crystalline grains embedded into the disordered matrix and study MRO-related properties of these models.

In the fifth chapter of this dissertation we will present our technique for preparation of physically realistic models of paracrystalline silicon (an amorphous material that contains crystalline grains embedded into the disordered matrix); models that have their structural, vibrational and electronic properties in uniform agreement with experiment. We will also present the first calculation of the MRO in a large and realistic model for paracrystalline Si which is in excellent qualitative agreement with the fluctuation electron microscopy experiments. We must add that the modeling procedure we have developed can be easily adjusted to produce not only the models containing grains but also crystalline-to-amorphous interfaces in Si, SiO_2 and like materials.

In addition we will show that our models for paracrystalline silicon can be turned into models for another important semiconducting material: nano/polycrystalline silicon — consisting of relatively large randomly oriented crystalline domains and containing disordered or amorphized atomic layers only on the boundaries between these domains — by means of simulated constant temperature annealing with molecular dynamics technique.

Chapter 2

Modeling methodology for amorphous silicon

There is a wide variety of computational methods that can be applied for studying the structural, vibrational and electronic properties of various phases of silicon, ranging from the state-of-the-art *ab initio* molecular dynamics techniques to simple empirical potentials. In this chapter we will review the underlying physical ideas, discuss and classify the actual implementations of such methods, point out their strengths and weaknesses, and draw some conclusions on situations and particular studies in which certain methods should be used.

The first and the most important task this method should perform is generation of the trajectories of atomic motion in molecular dynamics (MD) or Monte Carlo (MC) schemes used for modeling of our material under the limitations of a particular statistical ensemble we are working in.[1] This means that the method should produce

[1]The ensembles widely used the modeling procedures are the microcanonical const-NVE, the canonical const-NVT, the isothermal-isobaric const-NPT and the isoenthalpic-isobaric const-NPH ensemble.

accurate forces acting on atoms in our model system. Physically reasonable atomic forces combined with appropriate preparation techniques will result in a model exhibiting physically reasonable structural properties, which is paramount for successful investigations of more complicated properties of our models, like, for example, heat transport or interaction with light.

Secondly, if we need to obtain the phonon spectrum of our model system, the method should be able to create a physically reasonable dynamical matrix[14] for it. *Ideally* this stipulation is equivalent to the one mentioned above (accurate interatomic forces) but for many empirical or semiempirical methods this means additional fitting to experimental data, like positions of acoustic/optical phonon peaks in the experimental Raman spectra or vibrational density of states.

Finally, if we want to study the electronic properties of our model material we need a method that could produce the electron bandstructure energies and possibly their conjugate eigenvectors.

In an ideal situation, of course, we would prefer to have a *single* computational method that can perform all of the aforementioned duties and — which is also beneficial — give us a *uniform view* on the properties of our model (i.e. we do not switch techniques to study different properties). Currently the closest methods to this ideal case are the first principles or *ab initio* methods. Unfortunately, due to the substantial computational effort involved, today's level of computer development restricts the use of such methods to relatively small model systems (tens to a couple of hundred of atoms). Simpler and less computationally demanding methods are required to study

larger models, but the algorithm simplifications and the increase in computational effectiveness can be achieved only by the simplification of the underlying physics, some loss of precision, poorer transferability[2] and increasing *specialization* of the method, which means that it can't perform all of the three main tasks.

In the succeeding sections we will review and classify all the main techniques used to compute atomic forces in silicon and discuss the limits of their applicability and their merits and drawbacks.

2.1 *Ab Initio* methods

2.1.1 Density functional theory and pseudopotentials

The *ab initio* methods employed in solid state MD computations provide the most flexible and accurate ways to calculate the forces acting on atoms in the model system and the models' electronic and vibrational properties. Both methods that we are going to discuss in more detail below as well as the majority of other methods available make use of the local density approximation within the limits of the density functional theory (DFT). Here we present a short summary of the DFT and some additional concepts. An exhaustive review of the *ab initio* MD and total-energy calculations can be found in the paper of Payne *et al.*[15]

In general, the accurate determination of the atomic forces and the nature of

[2]Under transferability of a method we understand its ability to be applied to different topological systems (for example, different phases of Si) *without* explicitly refitting the method: i.e. *one and the same* fitting works for *all* systems.

chemical bonding in the system requires a precise calculation of its quantum electronic structure. In order to accomplish that, the many-body Schrödinger equation should be solved:

$$H_{MB}\Phi\big(\{\vec{r}_i\},\{\vec{R}_\mu\}\big) = E_{MB}\Phi\big(\{\vec{r}_i\},\{\vec{R}_\mu\}\big), \tag{2.1}$$

where Φ is a true many-body wave function of the system (possessing the correct symmetry), E_{MB} is the eigen energy, $\{\vec{r}_i\},\{\vec{R}_\mu\}$ are the sets of electronic and ionic coordinates where indexes i and μ number all electrons and ions respectively. The system Hamiltonian

$$H_{MB} = \sum_\mu \frac{\hat{P}_\mu^{\,2}}{2M_\mu} + \sum_i \frac{\hat{p}_i^{\,2}}{2m} + \frac{1}{2}\sum_{i,j}\frac{1}{|\vec{r}_i-\vec{r}_j|} - \sum_{\mu i}\frac{Z_\mu}{|\vec{r}_i-\vec{R}_\mu|} + \frac{1}{2}\sum_{\mu,\nu}\frac{Z_\mu Z_\nu}{|\vec{R}_\mu-\vec{R}_\nu|}, \tag{2.2}$$

where Z_μ and M_μ are ionic charges and masses and $\hat{P}_\mu$ and $\hat{p}_i$ are momentum operators for ions and electrons respectively.

Obviously an attempt to solve this equation rigorously in a solid is almost futile. Numerous simplifications are required for this problem to become tractable and the first one is to decouple the electron and ionic motions — the Born-Oppenheimer approximation[16]:

$$H_{MB} = \sum_\mu \frac{\hat{P}_\mu^{\,2}}{2M_\mu} + E\big(\{\vec{R}_\mu\}\big), \tag{2.3}$$

$$\Big(H_{MB} - \sum_\mu \frac{\hat{P}_\mu^{\,2}}{2M_\mu}\Big)\Psi_{\{\vec{R}_\mu\}}\big(\{\vec{r}_i\}\big) = E\big(\{\vec{R}_\mu\}\big)\Psi_{\{\vec{R}_\mu\}}\big(\{\vec{r}_i\}\big). \tag{2.4}$$

Here $E\big(\{\vec{R}_\mu\}\big)$ is the ground state energy of an electron system with frozen ionic

coordinates $\{\vec{R}_\mu\}$ and $\Psi_{\{\vec{R}_\mu\}}(\{\vec{r}_i\})$ is the many-body electron wave function (which should be antisymmetric).

The atomic forces can then be obtained by taking partial derivatives of $E(\{\vec{R}_\mu\})$:

$$\vec{F}_\nu = -\frac{\partial E(\{\vec{R}_\mu\})}{\partial \vec{R}_\nu}, \tag{2.5}$$

but the calculation of the derivatives as well as $E(\{\vec{R}_\mu\})$ itself is still impossible at the current level of complexity — a new simplification step is required which can be done with the mean field theory approach by applying of the density functional theory[17, 18]. Density functional methods are based on the Hohenberg-Kohn theorem[17] which states that

(i) The total energy of a system of interacting electrons can be represented as a functional depending *only* on the electron charge density

$$\rho(\vec{r}) = N_e \int |\Psi_{\{\vec{R}_\mu\}}(\vec{r}, \vec{r}_2 \ldots \vec{r}_{N_e})|^2 d\vec{r}_2 \ldots d\vec{r}_{N_e},$$

where N_e is the number of electrons in our system. Thus $E \equiv E[\rho]$ effectively maps our *many-electron* problem into a *one-electron* problem.

(ii) The ground state electron density $\rho_{gs}(\vec{r})$ minimizes the functional $E[\rho]$:

$$E[\rho(\vec{r})] \geq E[\rho_{gs}(\vec{r})].$$

The energy $E[\rho_{gs}(\vec{r})]$ represents the electronic part of the total system energy $E(\{\vec{R}_\mu\})$:

$$E(\{\vec{R}_\mu\}) = E[\rho_{gs}(\vec{r})] + \frac{1}{2}\sum_{\mu,\nu} \frac{Z_\mu Z_\nu}{|\vec{R}_\mu - \vec{R}_\nu|}. \tag{2.6}$$

Here instead of solving the true many-body equation 2.4 in order to find $E(\{\vec{R}_\mu\})$ we only need to find a minimum of the functional $E[\rho]$. The cost for this great simplification is that we actually don't know the exact form of the functional $E[\rho]$. Nevertheless, this problem can be solved by applying the method of Kohn and Sham[18]. In this method the electronic energy functional $E[\rho(\vec{r})]$ is split into four parts:

$$E[\rho] = T_e[\rho] + E_{ion}[\rho] + E_H[\rho] + E_{xc}[\rho], \tag{2.7}$$

where $T_e[\rho]$ is the kinetic energy of electrons, $E_{ion}[\rho]$ is the energy of electron-ion interaction

$$E_{ion}[\rho] = \int V_{ion}(\vec{r})\rho(\vec{r})d\vec{r}, \quad V_{ion}(\vec{r}) = -\sum_\mu \frac{Z_\mu}{|\vec{r} - \vec{R}_\mu|}, \tag{2.8}$$

$E_H[\rho]$ is the energy of classical Hartree electron-electron interaction

$$E_H[\rho] = \frac{1}{2}\int V_H(\vec{r})\rho(\vec{r})d\vec{r}, \quad \text{Hartree potential } V_H(\vec{r}) = \int \frac{\rho(\vec{r}')}{|\vec{r} - \vec{r}'|}d\vec{r}', \tag{2.9}$$

and finally E_{xc} is the term that accounts for electronic exchange and correlation effects and is unknown. We can write a formal expression for an exchange-correlation potential using the functional derivative:

$$V_{xc}(\vec{r}) = \frac{\delta E_{xc}[\rho]}{\delta \rho(\vec{r})}. \tag{2.10}$$

Since it is difficult to evaluate the kinetic energy of electrons $T_e[\rho]$ directly from the electron charge density $\rho(\vec{r})$ Kohn and Sham suggested use of single-electron orbitals $\phi_i(\vec{r})$ (Kohn-Sham orbitals) to define $\rho(\vec{r})$ as $2\sum_{i\,occ}|\phi_i(\vec{r})|^2$ and $T_e[\rho]$ as the kinetic energy of a system of *non-interacting* electrons with electron-charge density equal to

$\rho(\vec{r})$:

$$T_e = 2\sum_{i\ occ}\langle\phi_i| - \frac{1}{2m}\nabla^2|\phi_i\rangle. \tag{2.11}$$

Now the variational principle can be applied to equation 2.7 resulting in a set of equations for Kohn-Sham orbitals $\phi_i(\vec{r})$:

$$\left[-\frac{1}{2m}\nabla^2 + V_{ion}(\vec{r}) + V_H(\vec{r}) + V_{xc}(\vec{r})\right]\phi_i(\vec{r}) \equiv \left[-\frac{1}{2m}\nabla^2 + V_{[\rho]}(\vec{r})\right]\phi_i(\vec{r}) = \varepsilon_i\phi_i(\vec{r}), \tag{2.12}$$

where ε_i is the Kohn-Sham eigenvalue for orbital $\phi_i(\vec{r})$ and $V_{[\rho]}(\vec{r})$ is the *self-consistent* potential[3]:

$$V_{[\rho]}(\vec{r}) = V_{ion}(\vec{r}) + \int \frac{\rho(\vec{r}')}{|\vec{r} - \vec{r}'|}d\vec{r}' + \frac{\delta E_{xc}[\rho]}{\delta\rho(\vec{r})}. \tag{2.13}$$

The only problem that still remains in simple Schrödinger-type single-electron equation 2.12 is that the exchange correlation potential $V_{xc}(\vec{r}) = \delta E_{xc}[\rho]/\delta\rho(\vec{r})$ is unknown. If the functional $E_{xc}[\rho]$ were known, then the Kohn-Sham method would give us the exact value of the ground state energy $E\left(\{\vec{R}_\mu\}\right)$ from which the atomic forces could be obtained. Unfortunately we don't know the form of $E_{xc}[\rho]$, so that an approximation should be made for it. A very straightforward (and successful) approximation for the form of the exchange-correlation functional is the so called local density approximation (LDA) in which $E_{xc}[\rho]$ is assumed to be smooth and reasonably slow varying functional of ρ:

$$E_{xc}^{LDA}[\rho] = \int \epsilon_{xc}(\rho)\rho(\vec{r})d\vec{r},$$

[3]In the sense that it depends on the electron-charge density $\rho(\vec{r})$

where $\epsilon_{xc}(\rho)$ is the exchange-correlation density of a *homogeneous* electron gas of electron density ρ. $\epsilon_{xc}(\rho)$ has been computed by Ceperley and Alder[19] with quantum Monte Carlo technique and later parametrized by Perdew and Zunger[20].

Finally, one additional technique we would like to mention in this review is *pseudopotentials* that are used in the first-principles MD calculations to simplify the interactions with core electrons. The pseudopotential method exploits the fact that for the most of the atomic species the core electrons only weakly participate in chemical bonding in the solid and thus their contributions can be approximated by a smooth and slow varying potential, which can greatly increase the efficiency of computations. For example, in silicon instead of considering all 14 electrons on a single atom we can use only four valence electron orbitals, "hiding" the contribution of all the rest inside the pseudopotential.

2.1.2 Implementations: local basis vs. plane-wave basis sets

There exist various implementations of the first-principles MD methods which can be roughly divided into two families: one where the Kohn-Sham orbitals $\phi_i(\vec{r})$ are expanded into the plane-wave basis set and another where they are expanded into a local basis set.

A widely known example of the former type is the method of Car and Parrinello[21] (CP). In this method the self-consistent Kohn-Sham equation 2.12 is solved with no further approximations except for the plane-wave basis cutoff. In order to avoid repeated matrix diagonalizations (the typical size of the Hamiltonian matrix in the CP

method is $10^5 \times 10^5$), which is required in a direct self-consistent approach to solving Eq. 2.12, CP introduce a fictitious Lagrangian technique which treats electronic and ionic degrees of freedom as well as any external constraints imposed on the system simultaneously. The electron-ion interactions in this method are usually described in a form of "soft" (for example, Trouillier-Martins type[22]) or "ultrasoft" pseudopotentials, so that fewer plane waves can be used, and exchange and correlation energies and potentials are used in the parametrized form of Perdew and Zunger[20]. Unfortunately the CP method has extremely high computational demands, partially because a *very large number* of plane waves is required for an accurate expansion of Kohn-Sham orbitals.

As an example of the latter type we can examine the local-basis *ab initio* tight-binding method of Sankey-Niklewski-Drabold[23] (SND) which has been successfully applied to studies of amorphous Si and C and chalcogenide glasses. In addition to the LDA and the use of pseudopotentials in the form of the nonlocal, norm-conserving Hamann-Schlüter-Chiang type[24] parametrized by Bachelet *et al.*[25] this method exploits the following major approximations aimed at boosting the efficiency of computations.

(i) The total energy functional $E[\rho]$ can be replaced with the non self-consistent Harris functional[26]. The idea here is to replace the self-consistent electron density $\rho(\vec{r})$ with the sum of some reference density $\rho_0(\vec{r})$ (in the SND method it is taken to be the sum of neutral-atom spherical atomic densities) and a *small* term $\delta\rho(\vec{r})$ which accounts for the difference between the reference and the true densities. The $\rho_0(\vec{r})$

then is used as an "input density" in the Kohn-Sham eigenvalue equation 2.12 to generate the wave functions and construct an approximation for $\delta\rho(\vec{r})$:

$$\begin{aligned}\left[-\frac{1}{2m}\nabla^2 + V_{[\rho_0]}(\vec{r})\right]\tilde{\phi}_i(\vec{r}) &= \tilde{\varepsilon}_i\tilde{\phi}_i(\vec{r}),\\ \tilde{\rho}(\vec{r}) = 2\sum_{i\,occ}|\tilde{\phi}_i(\vec{r})|^2 &= \rho_0(\vec{r}) + \delta\tilde{\rho}(\vec{r}).\end{aligned}$$

Here the density change $\delta\tilde{\rho}(\vec{r})$ reflects the formation of bonds in the system and can be used as the first-order approximation to the self-consistent bond formation represented by $\delta\rho(\vec{r})$. The Harris functional can be successfully used in systems where charge transfer between orbitals is not too large and the bonding is largely covalent, not ionic.

(ii) The Kohn-Sham wave functions are expanded as a linear combination of pseudo-atomic-orbitals (PAO's):

$$|\phi_i(\vec{r})\rangle = \sum_{\mu\alpha} a_i^{\mu\alpha}|\varphi_\alpha^{PAO}(\vec{r} - \vec{R}_\mu)\rangle,$$

where index α represents all the valence orbitals on a single atom (for example, in case of C or Si atom we need four PAO's — s, p_x, p_y and p_z). Another requirement imposed on the form of PAO is the boundary condition that it should vanish outside some predetermined radius r_c:

$$\varphi^{PAO}(\vec{r})|_{r=r_c} = 0,$$

which has the physical effect of mixing in slight amounts of excited orbitals of the atom inside r_c. This condition shortens the interaction range of PAO's thus effectively

reducing the number of the Hamiltonian matrix elements required to be computed for them.

The Harris functional and the use of local pseudo-atomic-orbital basis make the SND *ab initio* MD method much more computationally effective than its plane-wave counterpart.

2.1.3 Merits and demerits

In this section we present the advantages and disadvantages of using the first-principles methods for computer modeling of materials.

Merits:

- ⊕ The interatomic forces and electronic eigenstates are computed from first principles requiring no fitting to any external parameters. The method is transferable to different material phases and can be used for modeling of complicated bonding environments like glasses and amorphous solids. It can be also used for modeling materials for which no experimental (fitting) data is available.

- ⊕ The interatomic forces and electron eigenvalues/eigenvectors produced are usually *very accurate*. Structural, electronic and vibrational properties of a model material can all be computed employing *one and the same* technique.

- ⊕ Numerous atomic species can be easily incorporated into the computations by the use of appropriate pseudopotentials.

Demerits:

⊖ Substantial computational effort is required thus limiting the applicability of the method to relatively small systems.

2.2 Empirical Tight-Binding Hamiltonians

2.2.1 Tight-Binding method

In order to investigate the properties of larger model systems a simpler and less computationally demanding method is required. One of the straightforward simplifications over the first-principles LDA techniques still sometimes capable of producing accurate atomic forces and electronic structure is the tight-binding (TB) Hamiltonian method. The details of this method have been described by Harrison[27].

In this method the ground state total energy E of the system can be approximated as a sum of two terms — the band-structure energy E_{BS} and the repulsive potential U_{rep}:

$$E(\{\vec{R}_i\}) = E_{BS} + U_{rep} = \sum_n \varepsilon_n + U_{rep}, \tag{2.14}$$

where $\{\vec{R}_i\}, i = 1 \ldots N$, is a set of atomic positions. The band-structure energy E_{BS} is the sum of the occupied electron eigenvalues ε_n, where $\{\varepsilon_n\}$ is a set of the eigenvalues of the system Hamiltonian H:

$$H|\psi_n\rangle = \varepsilon_n|\psi_n\rangle. \tag{2.15}$$

The electron eigenvalues ε_n, of course, may have an extremely complex dependence on the atomic coordinates $\{\vec{R}_i\}$).

In order to find the electron energies $\{\varepsilon_n\}$ we need to construct and diagonalize the Hamiltonian matrix $\{H_{mn}\}$ which elements

$$H_{mn} = \langle\psi_m|H|\psi_n\rangle. \tag{2.16}$$

The true eigenfunctions $\{\psi_n\}$ of Hamiltonian 2.15 are, of course unknown, so that, as usual, we need to expand them in a basis of functions that we know. In molecules or solids a convenient basis for such an expansion is *naturally available:* our eigenfunctions can be expanded in a linear combination of atomic orbitals (LCAO):

$$|\psi_n\rangle = \sum_{i,\alpha} C_n^{i\alpha}|\phi_{i\alpha}\rangle. \tag{2.17}$$

Here index i spans all the atoms in the system and index α — all the basis orbitals positioned on a given atom. For example, in the case of Si or C we can choose our minimal atomic orbital basis to be the valence s, p_x, p_y and p_z orbitals located on every atom in the system. Then the total number of the basis functions in our system will be $4N$.

Depending on whether or not we consider the basis functions $|\phi_{i\alpha}\rangle$ orthogonal to each other our method will fall into either orthogonal TB (OTB) or nonorthogonal TB category.

Now, if we substitute expansion 2.17 for $|\psi_n\rangle$ into equation 2.16, we can see that the matrix elements H_{mn} can be obtained as linear combinations of matrix elements between the basis orbitals:

$$H_{i\alpha,j\beta} = \langle\phi_{i\alpha}|H|\phi_{j\beta}\rangle. \tag{2.18}$$

If we consider the simplest case of two silicon atoms with their p_x, p_y and p_z orbitals parallel to each other respectively and p_z orbitals lying on the same axis, matrix elements $H_{i\alpha,j\beta}$ can be all represented by a small set of terms, that depend *only* on the interatomic distance R_{ij}. Two different diagonal terms are just "atomic orbital energies" E_s and E_p:

$$E_\alpha = H_{i\alpha,i\alpha}, \quad \alpha = s, p,$$

and four offdiagonal terms are "hopping elements"

$$\begin{aligned} V_{ss\sigma} &= H_{is,js}, \\ V_{sp\sigma} &= H_{is,j\alpha}, \quad \alpha = p_x, p_y, p_z, \\ V_{pp\sigma} &= H_{ip_z,jp_z}, \\ V_{pp\pi} &= H_{ip_x,jp_x} = H_{ip_y,jp_y}. \end{aligned}$$

Matrix elements between p-functions perpendicular to each other (like H_{ip_x,jp_y}) are considered to vanish due to the othogonality of the basis functions.

In a general case (for example, in real crystalline Si lattice), when atomic orbitals are not arranged in such a simple way, p-orbitals can be geometrically decomposed as vectors which enables us to reduce this problem to the previous case and still express offdiagonal elements $H_{i\alpha,j\beta}$ as linear combinations of terms $V_{ss\sigma}, V_{sp\sigma}, V_{pp\sigma}$ and $V_{pp\pi}$. The generalised method for performing such kind of decomposition has been proposed by Slater and Koster[28] (Slater-Koster table).

As we now see, the key element required for constructing the Hamiltonian matrix $\{H_{mn}\}$ is knowing the terms $V_{ss\sigma}, V_{sp\sigma}, V_{pp\sigma}, V_{pp\pi}$ and their dependence on interatomic

distance. In the empirical tight-binding (ETB) approach these terms are fitted to the results of first principles calculations and parametrised in a form of simple functions depending on distance.

The repulsive potential U_{rep} in 2.14 consists of two terms: the repulsive energy between nuclear charges Z_i and the term that corrects for the double counting of the electron-electron energy in the band-structure term E_{BS}:

$$U_{rep} = \frac{1}{2}\sum_{i,j}\frac{Z_i Z_j}{R_{ij}} - E_{DC}. \tag{2.19}$$

Here we assume that U_{rep} has a simple dependence from the atomic geometry and can be represented as a sum of short-range two-body potentials, each depending only on the distance between the corresponding atomic pairs. In the same way as for the TB-Hamiltonian matrix elements the repulsive potential can be fitted to the *ab initio* data.

Finally, the atomic forces are calculated with the help of the Hellmann-Feynman theorem[29]. In the case of fixed (not moving with the atoms) basis orbitals the forces look as follows:

$$\vec{F}_i = -\sum_n \frac{\partial \varepsilon_n}{\partial \vec{R}_i} = -\sum_n \langle \psi_n | \frac{\partial H}{\partial \vec{R}_i} | \psi_n \rangle. \tag{2.20}$$

2.2.2 Implementations

There exist more than a few empirical tight-binding Hamiltonians for silicon. The first TB-Hamiltonian for Si worth noting is due to Chadi[30] who used it to calculate the electronic densities of states and the bandstructure of diamond-like

and zincblende crystals and the atomic structure of silicon surfaces. Other well known ETB Hamiltonians are the orthogonal Hamiltonians of Goodwin, Skinner and Pettifor[31], Mercer and Chou[32], Kwon *et al.*[33], Wang *et al.*[34] and Lenosky*et al.*[35] and the nonorthogonal Hamiltonians of Menon and Subbaswamy[36] and Frauenheim *et al.*[37]. Another nonorthogonal TB-Hamiltonian for Si has been recently proposed by Bernstein *et al.*[38].

2.2.3 Merits and demerits

Merits:

- ⊕ The method provides information about the electronic structure of model material.
- ⊕ Still is relatively transferable if the atomic geometry is not too distorted comparing to the phase it has been fitted to.
- ⊕ Much more computationally efficient than *ab initio* methods.

Demerits:

- ⊖ Depends on fitting to experimental data or *ab initio* calculations. Fitting the TB-Hamiltonian to *simultaneously* reproduce phases with different bonding/geometry (for example, liquid *and* amorphous phase) is a matter of art and sometimes is not possible at all.

⊖ The repulsive energy term can only be defined by an empirical formula (i.e. can not be fitted to *ab initio* calculations).

⊖ Fitting to certain data makes the method somewhat "more specialized" than *ab initio* techniques. For example, the TB-Hamiltonian of Kwon, Biswas *et al.*[33] is good for force and total energy calculations but not for vibrational spectrum or band-structure calculations.

⊖ Still requires to solve at least one matrix eigenvalue/eigenvector problem *on every step* of the MD simulation. This limits the applicability of the method to systems containing hundreds but not thousands of atoms.

⊖ Practically all of the ETB Hamiltonians have problems reproducing the optical part of the phonon spectrum of a-Si.

2.3 Empirical potentials

2.3.1 Major families of empirical potentials for silicon

An empirical interatomic potential is one of the most simple and straightforward methods available to study the dynamical and structural properties of solids. Such a potential looks like a simple "prescription" describing the atomic interactions in a solid and containing a number of adjustable parameters. These parameters are fitted to experimental data and the results of *ab initio* calculations, usually in such a way that the potential reproduces as closely as possible the cohesive energy curves for different

highly symmetric phases of solid under investigation. For silicon the most popular symmetric fitting phases are diamond-cubic (dc), simple-cubic (sc), face-centered-cubic (fcc), body-centered-cubic (bcc) and hexagonal-close-packed (hcp) structures.

The general idea for constructing this "prescription" for atomic interactions is the following: for a system containing N identical particles the total energy of the system can be expanded into one-body, two-body, three-body, etc. contributions:

$$E(\{\vec{R}_i\}) = \sum_i v_1(\vec{R}_i) + \sum_{<i,j>} v_2(\vec{R}_i, \vec{R}_j) + \\ + \sum_{<i,j,k>} v_3(\vec{R}_i, \vec{R}_j, \vec{R}_k) + \ldots + \sum_{<i_1,\ldots,i_N>} v_N(\vec{R}_{i_1}, \ldots, \vec{R}_{i_N}). \quad (2.21)$$

The single particle potential v_1 usually describes an external force applied to the system; in most situations we can consider any external forces to be absent and consequently can ignore this term.

In order for the expansion 2.21 to be practically useful for computations the component functions v_n must fall quickly to zero with increasing n. Obviously this property strongly depends on the nature of cohesion in a material under investigation. For example, for the liquified noble gases (Ar, Kr, Xe) only pair interactions are important, which reduces 2.21 to

$$E(\{\vec{R}_i\}) = \sum_{<i,j>} v_2(\vec{R}_i, \vec{R}_j),$$

where pair potential v_2 can be represented by the famous Lennard-Jones potential

$$v_{LJ}(R_{ij}) = -4\epsilon\left[(\sigma/R_{ij})^{12} - (\sigma/R_{ij})^6\right].$$

Of course, for covalent materials such as Si, pair potentials alone are inadequate to describe the cohesion — the equilibrium diamond lattice is unstable without three-body forces. The natural way to solve this problem is to use more terms in expansion 2.21 in order to account for non pair interactions in the material.

One of the oldest well known interatomic potentials for Si is the potential of Keating[39] which has been successfully applied to studies of the strain energy in the diamond-like crystals. This potential incorporates two- and three-body interaction terms:

$$E(\{\vec{R}_i\}) = \frac{3}{16}\frac{\alpha}{R_0^2}\sum_{ij}\left(R_{ij}^2 - R_0^2\right)^2 + \frac{3}{8}\frac{\beta}{R_0^2}\sum_{ijk}\left(\vec{R}_{ij}\cdot\vec{R}_{ik} + \frac{1}{3}R_0^2\right)^2. \qquad (2.22)$$

Here α and β are the bond-stretching and bond-bending force constants and R_0 is the equilibrium interatomic bond length in the diamond structure. The interaction range for both two- and three-body terms is limited to the first shell of neighbors, so that indexes j and k mark *only the nearest neighbors* of a given atom i (exactly four for a perfect diamond lattice). For small distortions that do not alter the bonding topology of the network, the Keating model can provide some insight into the network's structure but for more drastic reconstructions a better model is required.

A model that is currently widely used for studies of the structural and dynamical properties of silicon is the empirical interatomic potential of Stillinger and Weber[40] (SW), which has been originally fitted to the crystalline (c-Si) and liquid (l-Si) silicon phases. Like Keating model this potential also consists of sums of two- and three-body

interaction contributions:

$$E(\{\vec{R}_i\}) = \sum_{<i,j>} v_2(R_{ij}) + \sum_{<i,j,k>} v_3(\vec{R}_{ij}, \vec{R}_{ik}), \tag{2.23}$$

where the two-body term

$$v_2(R_{ij}) = \epsilon A \left[B\Big(\frac{R_{ij}}{\sigma}\Big)^{-p} - 1 \right] \exp\left\{ \frac{1}{R_{ij}/\sigma - a} \right\} \Theta(R_{ij}/\sigma - a), \tag{2.24}$$

and the three-body term

$$v_3(\vec{R}_{ij}, \vec{R}_{ik}) = \epsilon\lambda \exp\left[\frac{\gamma}{R_{ij}/\sigma - a} + \frac{\gamma}{R_{ik}/\sigma - a} \right] \times$$
$$\times \left(\cos\theta_{jik} + \frac{1}{3} \right) \Theta(R_{ij}/\sigma - a)\, \Theta(R_{ik}/\sigma - a). \tag{2.25}$$

Here $\Theta(x)$ is the Heaviside step function, θ_{jik} is the angle between bonds R_{ij} and R_{ik} and ϵ, A, B, σ, p, a, λ and γ are the fitting parameters (see Table 2.1). The interaction range of the potential is governed by parameters σ and a that place the interaction cutoff at approximately 3.77Å — between the first and second-neighbor distances for c-Si. The main property of the three-body term is that it penalizes any deviation from an ideal diamond structure bond angle (for which $\cos\theta_{jik} = -\frac{1}{3}$) thus favoring perfect tetrahedral bonding in the material.

Another example of the 2 + 3 body interatomic potential is the potential of Biswas and Hamann. The generalized Morse two-body potential has been used to describe pair interactions in this potential:

$$v_2(R_{ij}) = A_1 e^{-\lambda_1 R_{ij}} + A_2 e^{-\lambda_2 R_{ij}},$$

Table 2.1: **Parameters for the standard SW and the modified SW potentials.**

Parameter	standard SW	modified SW
ϵ (eV)	2.16826	1.64833
A	7.049556277	7.049556277
B	0.6022245584	0.6022245584
σ (Å)	2.0951	2.0951
p	4	4
a	1.80	1.80
λ	21.0	31.5
γ	1.20	1.20

and the three-body term has been expanded in spherical harmonics (which can also be done for the SW potential):

$$v_3(\vec{R}_{ij}, \vec{R}_{ik}) = \sum_l C_l \phi_l(R_{ij}) \phi_l(R_{ik}) P_l(\cos\theta_{jik}).$$

The key simplification here is an assumption that for each l the dependence on R_{ij} and R_{ik} is a *separable* and symmetric product of functions ϕ_l of each bond length, which leads to computations of the energy and atomic forces in n^2 steps instead of n^3 for a general three-body potential. Another peculiar feature of this potential is its long range. A cutoff of 15Å is *barely* adequate — this corresponds to counting all two-body interactions out to fifteen shells of neighbors and three-body contributions to forces for all neighbors within 20Å.

One more widely employed model that uses a different potential-construction strategy is the family of interatomic potentials developed by Tersoff[42]. The main

idea incorporated into this potential is that bonding in the material depends upon local environment, i.e. for different local atomic coordinations (or the number of competing bonds) the "prescription" formula should favor different bonding geometries. The form of the potential is as follows:

$$E(\{\vec{R}_i\}) = \sum_{<i,j>} v_2(\vec{R}_i, \vec{R}_j),$$

where v_2 is the generalized Morse-type potential:

$$\begin{aligned} v_2(\vec{R}_i, \vec{R}_j) &= f_c(R_{ij}) \Big[A e^{-\lambda_1 R_{ij}} - B(\vec{R}_i, \vec{R}_j) e^{-\lambda_2 R_{ij}} \Big], \\ B(\vec{R}_i, \vec{R}_j) &= B_0 \exp \Big\{ - Z(\vec{R}_i, \vec{R}_j)/b \Big\}. \end{aligned}$$

Here $f_c(R_{ij})$ is a cutoff function which truncates the potential at a point between the first- and second-neighbor distances for c-Si (around 3Å) and $B(\vec{R}_i, \vec{R}_j)$ is the term that describes *all* deviations from a simple pair potential via the dependence upon the local atomic environment. The term

$$Z(\vec{R}_i, \vec{R}_j) = \sum_{k \neq i,j} \Big[\frac{w(R_{ik})}{w(R_{ij})} \Big]^n \Big(c + \exp(-d \cos\theta_{jik}) \Big)^{-1},$$

where $w(r)$ is the "bare" bonding potential, $w(r) = f_c(r) \exp(-\lambda_2 r)$, is a weighted measure of the number of bonds competing with the bond R_{ij}, and b determines how rapidly the bond strength falls off with increasing effective coordination.

The Tersoff potential has been fitted to a wide set of different bulk phases of Si and is considered to be somewhat more transferable than SW potential.

Quite recently a new environment-dependent interatomic potential (EDIP) for silicon has been introduced by Bazant, Kaxiras *et al.*[43, 44] which can be regarded as

a "crossbreed" between the SW and Tersoff potential formats. Like the SW potential it consists of two- and three-body terms, but both of these terms depend on the local-environment parameter Z_i:

$$\begin{aligned} E(\{\vec{R}_i\}) &= \sum_{<i,j>} v_2(R_{ij}, Z_i) + \sum_{<i,j,k>} v_3(\vec{R}_{ij}, \vec{R}_{ik}, Z_i), \\ Z_i &= \sum_{m \neq i} f(R_{im}), \end{aligned}$$

where $f(R_{im})$ is a cutoff function that measures the contribution of neighbor m to the coordination of atom i in terms of interatomic separation R_{im}.

The two-body term includes repulsive and attractive interactions

$$v_2(R_{ij}, Z_i) = A\left[\left(\frac{B}{R_{ij}}\right)^{\rho} - p(Z_i)\right] \exp\left\{\frac{\sigma}{R_{ij} - a}\right\},$$

which go to zero at the cutoff distance a (approx. 3.12Å). The environment dependent part is represented by a Gaussian function: $p(Z_i) = \exp(-\beta Z_i)$.

The three-body term contains radial and angular parts:

$$v_3(\vec{R}_{ij}, \vec{R}_{ik}, Z_i) = g(R_{ij})g(R_{ik})h(\cos_{jik}, Z_i),$$

where the radial function $g(r)$ has the SW form: $g(r) = \exp(\frac{\gamma}{r-a})$ and goes to zero smoothly at the cutoff distance a. The angular function $h(\cos\theta, Z)$ has strong dependence on the local coordination through two functions that control the equilibrium angle and the interaction strength and will not be discussed here in further detail.

The potential has been fitted to reproduce not only the *ab initio* cohesive energies but also the elastic constants of the diamond-cubic structure.

2.3.2 Flaws in empirical potentials fitted to highly ordered Si phases

Unfortunately none of the above mentioned potentials can correctly describe the phonon spectrum of a-Si, especially its high-frequency part — the correct height and position of the transverse-optical peak (see section 3.2.2 and references in Table 3.2). This is partially because the reproduction of the phonon dispersion curves in Si or Ge is a problem barely tractable without high quality *ab initio* calculations[45], but another important contribution to the occurring errors is fitting to the properties of highly ordered Si phases *only*. Obviously the potential that is intended to be used for calculations of properties of the amorphous phase of silicon should be fitted to this actual phase.

In case of the popular SW potential a new set of fitting parameters has been found, that can provide an adequate simultaneous description of crystalline and amorphous phases (but not the liquid phase). More than ten years ago it has been noticed that the 50 to 100% increase in strength of the three-body term in the SW potential produces a-Si models with structural properties in a much better agreement with experiment than for standard SW[46, 47] but in order to further improve the description of the vibrational properties of a-Si models created or studied with this potential additional changes in the fitting procedure are required.

Recently Vink *et al.*[48] have explicitly fitted the SW potential to reproduce the correct positions of experimentally measured (see Ref. [4]) transverse-acoustic (TA)

and transverse-optical (TO) peaks of the vibrational density of states (VDOS) of a-Si. It turns out that these modifications also lead to structural properties of models relaxed with this potential that are in excellent agreement with experiment (see section 3.4 for more details). The adjusted potential will be referred to in what follows as the modified Stillinger-Weber (MSW) potential. The fitting parameters for the MSW potential are presented in Table 2.1.

2.3.3 Merits and demerits

Merits:

- ⊕ Very computationally effective.
- ⊕ Very easy to implement in a form of program code.

Demerits:

- ⊖ Poor transferability to phases the potential has not been fitted to. Reproduction of the amorphous phase of Si requires explicit fitting to this phase.
- ⊖ Very poor transferability between phases with different bonding environment (Example: a-Si and l-Si).
- ⊖ Electronic structure properties are unavailable.

Chapter 3

Modeling of amorphous silicon

The generally accepted topological model used to represent the structure of amorphous tetrahedral semiconductors is a so called "continuous random network" (CRN) first proposed by Zachariasen[49] in 1932. In this model the main building blocks of the material are the same as in its crystalline incarnation — i.e. tetrahedra for silicon or germanium — but unlike in a perfect crystal these blocks can be randomly oriented and connected, allowing "play" in atomic bond lengths and angles.

The first mechanical CRN model was constructed by Polk[50] in 1971. It reflected the general topology of elementary amorphous semiconductors but, due to physically unmotivated construction procedure, contained free surfaces in its structure. It was obvious that next generation CRN models should be created on a computer and employ physically relevant topology building algorithms.

In this chapter we will present all the major computer based methods for generating the CRN models of amorphous tetrahedral semiconductors, analyze their advantages and disadvantages and study the properties of the models created with

these methods. Our discussion will be mostly focused on three major issues that can be used to characterize a particular modeling technique:

- model's template i.e. a starting structural configuration (a list of atomic coordinates and sometimes an additional list of bonds between atoms) from which the model will be created,
- a recipe (potential) describing interatomic interactions in the model,
- a procedure that tells us how to rearrange the initial configuration's geometry to turn it into a structure with specified properties.

3.1 Bond-switching method of Wooten, Winer and Weaire

3.1.1 Method description

The bond-switching method of Wooten, Winer and Weaire (WWW), introduced in 1985, was successfully applied to modeling of CRN structures for a-Si, a-Ge and amorphous diamond[51, 52]. In this section we give a description of this method.

The initial structure used in the WWW method is a perfect diamond crystal. Periodic boundary conditions are imposed on the cubic supercell containing the structure, so that every atom is 4-fold coordinated and there are no dangling bonds anywhere. We may regard this representation of our system as a list of N atoms and a list of

$2N$ bonds between these atoms.

The interactions between the atoms are described by 2 + 3 body harmonic (Keating) potential[39]:

$$E = \frac{3}{16}\frac{\alpha}{R_0^2}\sum_{ij}\left(R_{ij}^2 - R_0^2\right)^2 + \frac{3}{8}\frac{\beta}{R_0^2}\sum_{ijk}\left(\vec{R}_{ij}\cdot\vec{R}_{ik} + \frac{1}{3}R_0^2\right)^2, \qquad (3.1)$$

where α and β are the bond-stretching and bond-bending force constants, R_0 is the equilibrium strain-free interatomic bond length in the diamond structure, index i spans all the atoms in the system and indexes j and k — the nearest neighbors (exactly four) of a given atom i.

And finally the main structural rearrangement used to transform the perfect crystal into the CRN is a so called WWW bond transposition or bond switch shown in Fig. 3.1. For a bonded pair of atoms BC a pair of nearest neighbors A and D is chosen, so that A is the neighbor of B and not the neighbor of C, and D is the neighbor of C and not the neighbor of B. Then bonds AB and CD are broken (deleted from the bond lists for atoms B and C) and new bonds AC and BD are created (added to the appropriate bond lists), i.e. atoms B and C exchange neighbors. This procedure effectively introduces five- and sevenfold rings — which are a characteristic structural feature of the CRN — in the network while *preserving the tetrahedral bonding in it.*

Turning the initial highly ordered structure into an amorphous structure is done in two stages. On the first stage, the initial diamond structure is randomized by a large number of WWW bond transpositions at temperature close to the melting point of the model. Bond transpositions are accepted with the Metropolis acceptance

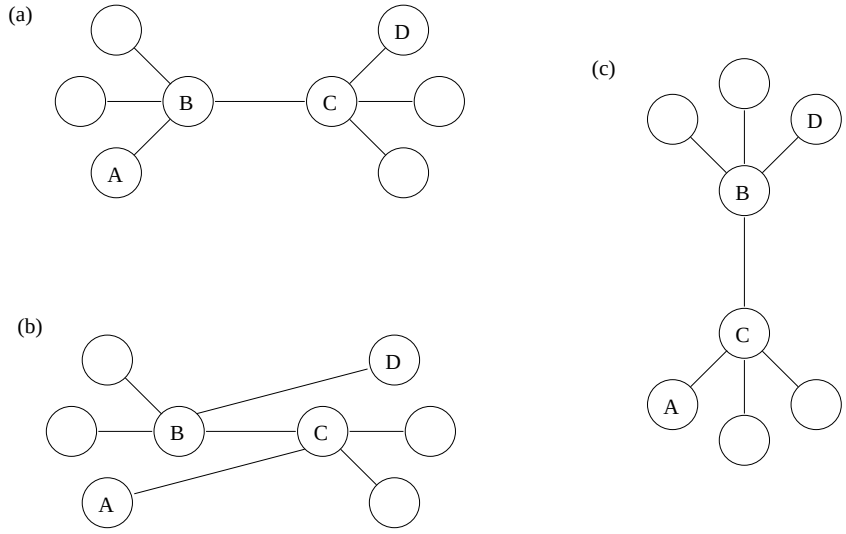

Figure 3.1: **Wooten, Winer, Weaire bond transposition. (a) configuration before the bond transposition, (b) configuration after the bond transposition, (c) configuration after the bond transposition (unfolded).**

probability[53]

$$P = \mathrm{Min}\left[1, \exp((E_b - E_f)/k_b T)\right], \tag{3.2}$$

where k_b is the Boltzmann constant, T is the temperature, E_b is the total energy of the system before the proposed bond transposition and E_f the total energy of the system after the bond transposition *and a full structural relaxation* succeeding this transposition. The aim of this procedure is to get rid of the crystallinity, so that subsequent bond rearrangements at lower temperatures do not return the system to the perfect diamond structure.

On the next stage the system is subjected to many more bond-switching events that are accepted or rejected with Metropolis probability while the temperature is

lowered in small steps, and thermal equilibrium is established at each new temperature. The resulting structure appears to be a well relaxed CRN with low strain, physically reasonable bond-angle and bond-length distributions and practically 100% 4-fold coordination of atoms (see section 3.2 for the discussion of properties of a-Si models created with this method).

3.1.2 Improvements over the method of WWW

Despite the fact that the WWW method allows us to create the CRN models of very high quality it suffers from a number of disadvantages: **(i)** since the initial configuration of the system is a crystal, even after a substantial number of bond transpositions the system may retain its memory of the crystalline state[54], **(ii)** for a model, presented in Ref. [51] the bond-angle distribution width $\Delta\theta$ (see below) is slightly wider[1] than the experimental value[3], **(iii)** the acception/rejection and relaxation procedures are not effective enough to try all combinations of bond transpositions.

Recently Barkema and Mousseau have introduced an improved version of the WWW bond-switching method[55] (called the modified WWW method in what follows) that does not have the aforementioned problems. In the next few paragraphs we summarize the advantages of the improved bond-switching method.

(1) The initial configuration for the model is completely random which guarantees

[1]Generally, the value of $\Delta\theta$ depends on the MC annealing time. With slower anneals it may be possible to receive smaller bond-angle distribution widths.

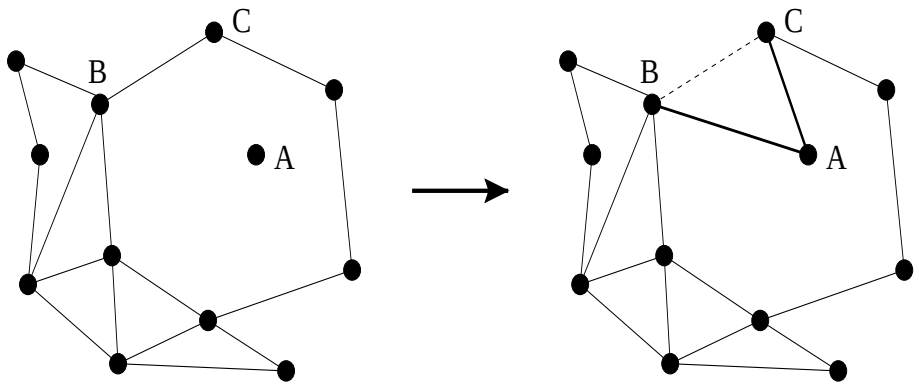

Figure 3.2: **Bond list construction procedure for modified WWW method. One step in the expansion of the loop, that eventually visits all atoms four times. Three atoms A, B, and C are involved, of which B and C are bonded, while A is bonded to neither B nor C, and of which A is not four-fold coordinated. The bond BC is then replaced by bonds AB and AC.**

that it is not contaminated by any memory of the crystalline state. The atoms are randomly placed in a cubic box with periodic boundary conditions and volume corresponding to the crystalline density under constraint that no two atoms are closer than 2.3Å to each other. After all the atoms are positioned in the box, the bond list is constructed by finding a loop visiting four atoms somewhere in the network, so that every two atoms that are neighbors in the loop are closer than some cutoff distance to each other. The loop is then expanded until it visits each atom exactly twice, and the steps of the loop become the bonds in the tetravalent network. The loop-expansion step is made as follows (see Fig. 3.2): a group of three atoms A, B and C is randomly selected, such that A is not four-fold coordinated and is within a distance of r_c from B

and C but not bonded to either, while B and C are bonded. The bond BC is replaced by bonds AB and AC.

This procedure results in a configuration where every atom has exactly four bonds, but of course this structure has a very wide bond-angle distribution and a vast number of bonds that are unphysically long. We should stress that these bonds are *not intended* to represent real physical bonds in the material, instead they are merely mathematical abstractions stating that atom A is connected to atom B. During the quenching procedure these bonds will be surely broken — their energy is too high — and new, physically relevant bonds will be formed.

(2) A trial bond transposition can be rejected *without* doing full relaxation of the model system. In order to do that, a so called threshold energy E_t is evaluated before the proposed bond switch:

$$E_t = E_b - k_B T \ln(s), \tag{3.3}$$

where s is a random number between 0 and 1. The bond transposition is then accepted *only* if $E_f \leq E_t$. Since in a well relaxed configuration the energy is harmonic around the minimum, then the decrease in energy due to further relaxation can be estimated as the square of force times some proportionality constant:

$$E - E_f \approx c_f |F|^2.$$

If at any moment during the relaxation $E - c_f|F|^2$ becomes bigger than E_t the trial bond switch is rejected and a new one is started.

With a conservatively chosen c_f (well below 1 in well relaxed systems) this method is equivalent to the usual Metropolis procedure, but it allows us to reject a trial bond switch as soon as it becomes evident that the threshold energy can't be reached, i.e. *before* the full relaxation of the system is over. Since in a well quenched model system only a few percent of proposed bond transpositions are eventually accepted, this improved "rejection procedure" provides us with a significant increase in computational efficiency.

(3) Efficient quenching techniques: **(i)** to reduce the number of force calculations the relaxation of atomic positions is being done only locally (up to the third neighbor shell) during the first ten relaxation steps. In combination with technique (2) this makes the computation effort per bond transposition almost independent of the size of the system. **(ii)** in case of zero temperature quenching, the threshold energy 3.3 remains constant, which means that a bond transposition that is once rejected will keep on being rejected as long as no other bond transpositions are accepted in the meantime. Then all the bond transpositions rejected since the last accepted bond transposition can be marked to avoid retrying them. When all possible bond transpositions have been tried and rejected the quenching process is regarded to be complete. At this point the model system is not only in the local energy minimum but no single bond transposition can lower its energy.

With all the aforementioned advantages the modified WWW modeling method works in the following way. First a truly random atomic configuration is created (see point (1) above) and the atoms in it are connected, so that each one of them

has exactly four neighbors. Then this initial configuration is alternately subjected to the Metropolis MC bond-switching runs at temperatures of 0 and 0.25 eV until the desired structural properties of the model (usually the narrowing of the bond-angle distribution width $\Delta\theta$ down to 10° or less) are reached. Due to the fact that in the Keating's model atoms interact only with their bond-list neighbors, some atoms might get close to each other without being bonded. In this case they are bonded together and the bonds between them and their neighbors are rearranged in such a way that the four-fold coordination is preserved. The decrease in energy mostly takes place during the 0 eV quenching runs, while the 0.25 eV annealing runs are used merely to provide a fresh starting point for the next quench. Once the angular spread $\Delta\theta$ is brought down to 11-12° the alternating annealing/quenching procedure yields smaller and smaller energy drops. In order to lower energy even further the system is slightly expanded or compressed and the annealing is done again.

The described modeling procedure produces perfectly 4-fold networks that are structurally and electronically better than those created with the standard WWW method. The properties of the models created with both of these methods are presented in the next section.

3.2 Properties of a-Si models, created with the WWW and modified WWW methods

In this section we will discuss structural, vibrational and electronic properties of two families of models for a-Si that are extensively used in our research projects. The first family is the set of models created by Djordjević, Thorpe and Wooten[52] with standard WWW bond-switching method. Models of two sizes will be discussed: a small 216-atom model, called DTW216, and a large 4096-atom model, called DTW4096 (which exists in two variants — with and without 4-membered rings). The second family is the set of models constructed by Barkema and Mousseau using the modified WWW technique[55]. We will present the properties of 1000-atom (BM1000) and 4096-atom (BM4096) models of Barkema and Mousseau.

We *do not* discuss here the properties of the original 216-atom model of Wooten, Winer and Weaire. Its structural and vibrational properties can be found in Ref. [51, 54] and electronic properties in Ref. [56, 57].

3.2.1 Structure

The structural properties of a CRN model of a-Si can usually be estimated as a collection of certain parameters and distributions. The most important parameters are model's density, average coordination number, bond length $\langle r \rangle$ with its distribution spread Δr and bond angle $\langle \theta \rangle$ with its distribution spread $\Delta \theta$.

The coordination number shows how many nearest neighbors (or bonds) on average each atom in the model has. It can be derived from experimental data by careful integration of the area under the first peak of the radial-distribution function $g_2(r)$[2, 3] (see below). As we know, the real amorphous silicon has a very low density of point defects[1] — 0.1% or lower. It is then paramount for a good model of a-Si to have as few coordination defects as possible — the presence of an unphysically large number of coordination defects (more than a couple of tenths of a percent) in a model ruins its electronic properties, turning it from a semiconductor to a poor metal (see subsection 3.2.3 for a detailed discussion).

Another important parameter which is a *de facto* figure of merit for the CRN models of tetrahedral amorphous semiconductors is the bond-angle distribution width $\Delta\theta$. When it is close to the experimentally measured value of 9–10°, it means that the model is well relaxed and contains few if any strained regions. The experimental value for $\Delta\theta$ can be inferred from the X-ray diffraction[3] (structure factor) or Raman spectra measurements.

Important distributions that help us gain insight of the structural properties of a-Si are different forms of atomic position-correlation functions[58] — the most widely used one is the pair-correlation or radial-distribution function — bond- and dihedral-angle distributions and ring statistics.

The position-correlation function of order n $g_n(r_1, r_2, \ldots, r_{n-1})$ measures a probability for a given atom i to have a neighbor at certain distance r_1 and simultaneously

another neighbor at distance r_2 and another at r_3 etc. up to a neighbor at r_{n-1}, averaged over all the atoms in the system $i = 1, \ldots, N$. With the increasing order this function gives more and more complete description of geometrical structure of our material. It is, of course, relatively easy to calculate the high order atomic position-correlation functions for a model but unfortunately the experimental data commonly available for comparison usually comes in a form of the lowest order pair-correlation function $g_2(r)$[2, 3], which, for the sake of shortness, we will call in what follows $g(r)$. Only the most recent state-of-the-art fluctuation microscopy experiments allow us to probe for the fourth order correlation function $g_4(r_1, r_2, r_3)$[10, 11].

According to the more general definition given in the previous paragraph the radial-distribution function $g(r)$ measures the probability for a given atom i to have a neighbor at a certain distance r, averaged over all the atoms in the system, i.e.

$$g(r) = \frac{1}{4\pi\rho N r^2} \sum_{i=1}^{N} \sum_{j \neq i} \delta(r_i - r_j), \tag{3.4}$$

where ρ is system's density.

In the case of an ordered solid (crystal) the long-range environment for every atom is exactly the same, so that the pair-correlation function of the system will have a form of a set of δ-functions positioned at the distances corresponding to the distance between an atom and a certain shell of its neighbors. For example, for diamond-type Si crystal we will get peaks at 2.35Å (first shell of neighbors), 3.8Å (second shell of neighbors), 4.5Å (third shell of neighbors) etc.

In an amorphous solid the long- and medium-range order is broken and consequently the local environment for every atom is different. The interatomic distances are not fixed any more, so that δ-functions in Eq. 3.4 will not be all concentrated at certain values of r like in the crystal case — instead they will be *spread around* these values. Usually, before plotting out the pair-correlation function, δ-functions are thermally broadened (by representing them as δ-shaped Gaussian functions), which gives us a smooth curve for $g(r)$. For a specially normalized pair-correlation function the integration of the area under its first peak provides information about the average number of the nearest neighbors for an atom, i.e. average coordination number.

The $g(r)$ can be inferred from experimental data by taking the Fourier transform of the structure factor $S(q)$ obtained by the X-ray diffraction[2, 3]. It is useful to note that a comparison of the model $g(r)$ to an experimental one should not be regarded as an ultimate test of model's quality. The good agreement of both is a *necessary condition* for a CRN model to serve as a good representation of amorphous material, but it is *not sufficient*! The geometrical structure of the material is three-dimensional while the $g(r)$ "flattens" all this information into a single curve, which makes it possible to create absolutely unphysical models that still perfectly agree with the experimental pair-correlation function data[2].

We collect the structural properties of the large DTW and BM models in Table 3.1. Note that we do not present any information about the coordination of the models because *by the virtue of construction procedure* all of these models are almost perfectly

[2] One of the recent examples of this kind of approach can be found in Ref. [59]

four-fold coordinated. We also stress that this data refers to the models that are *not relaxed* by the means of any MD technique. Relaxation with a potential, poorly fit for the job, may ruin the perfect tetrahedral coordination of the model, which is the case, for example, for the standard SW potential[44, 55].

Table 3.1: **Structural properties of models relaxed with the Keating potential. The first two models, DTW4096$^{(1)}$ and DTW4096$^{(2)}$ are prepared with the WWW method (Ref. [52]) and refer, respectively, to a model with and without four-membered rings. The models BM1000A and B are 1000-atom models and BM4096 is a 4096-atom model prepared with the modified WWW method. All three models are without four–membered rings. The ring statistics are for irreducible rings and ρ_0 is based on $r_0 = 2.35$ Å.**

	DTW4096$^{(1)}$	DTW4096$^{(2)}$	BM1000A	BM1000B	BM4096
ρ/ρ_0	1.000	1.000	1.043	1.040	1.051
$\langle r\rangle/r_0$	0.996	0.997	0.982	0.982	0.980
$\Delta r/r_0$ (%)	2.52	2.65	3.94	3.71	4.17
$\langle\theta\rangle$	109.24	109.25	109.30	109.27	109.28
$\Delta\theta$	10.51	11.02	9.21	9.20	9.89
Rings/atom					
4	0.015	0.000	0.000	0.000	0.000
5	0.491	0.523	0.472	0.480	0.490
6	0.698	0.676	0.761	0.750	0.739
7	0.484	0.462	0.507	0.515	0.467
8	0.156	0.164	0.125	0.116	0.148
9			0.034	0.033	0.035

The radial-distribution function and the bond- and dihedral-angle distributions for all the DTW and BM models of a-Si look pretty much the same. In Fig. 3.3 we present the curves only for BM4096 model which can serve as a good example. Notice the clear gap between the first and the second-neighbor peaks in the $g(r)$ plot.

3.2.2 Vibrational properties

To investigate vibrations in a-Si we compute the vibrational density of states (VDOS) or phonon spectrum for our DTW and BM models and study spatial localization of the associated vibrational states. We do not simulate Raman spectra because both widely used theoretical models for its calculation (Alben *et al.*[60] and Marinov-Zotov[61]) do not provide good agreement with experimental results[62].

We calculate the VDOS for a model system, constructing and then directly diagonalizing its dynamical matrix. In order to do that the system is first relaxed to its equilibrium geometry by simulated quenching with an appropriate MD technique, so that all the forces on every atom are close to zero. Once the equilibrium state is reached, we proceed with the dynamical matrix calculation, displacing every atom in the supercell in three orthogonal directions (by 0.03Å, which is suitable for this purpose) and computing the resulting spring constants as second derivatives of the total energy of the system. The size of the dynamical matrix is $3N \times 3N$. Diagonalizing the dynamical matrix we receive all of its eigenvalues $\omega_i^2, i = 1 \ldots 3N$, together with the corresponding eigenvectors. The details of this procedure can be found in Ref. [63].

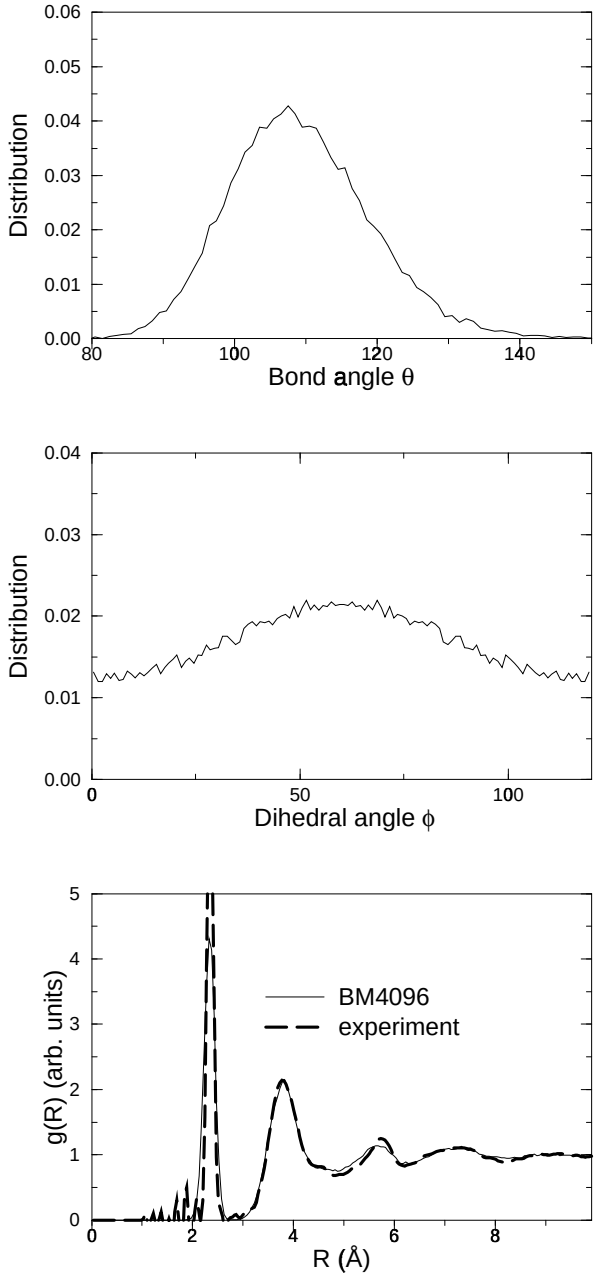

Figure 3.3: **Structural properties of BM4096 model. Upper panel: bond-angle (θ) distribution. Middle panel: dihedral-angle (ϕ) distribution. Lower panel: radial-distribution function $g(R)$; the experimental results (dashed line) are taken from Ref. [2, 3].**

We plot out the vibrational density of states (VDOS)

$$VDOS(\omega) = \frac{1}{3N} \sum_{i=1}^{3N} \delta(\omega - \omega_i) \tag{3.5}$$

for the set of phonon frequencies $\omega_i, i = 1 \ldots 3N$ (usually the lowest three frequencies corresponding to the elementary supercell translations are discarded), which gives us the information about vibrational states distribution along the energy axis. As in the case with $g(r)$ representation we use Gaussian broadened form for $\delta(\omega - \omega_i)$ to make our curves look smooth.

In Fig. 3.4 we present the VDOS for DTW216 model calculated with *ab initio* local basis TBMD code "Fireball-96" based on the SND method[23, 63] (black line), the environment-dependent interatomic potential of Bazant *et al.*[43, 44] (red line) and the modified SW potential[40, 48]. The experimental data (diamonds) is taken from the paper of Kamitakahara *et al.*[4]. For all the above mentioned calculations we have found no negative eigenvalues ω_i^2 in our dynamical matrix which means that our system is at a true local energy minimum.

As we can see from Fig. 3.4 the modified SW potential gives the best agreement with the positions of the experimental TA and TO peaks at $\omega_{TA} = 184.8$ and $\omega_{TO} = 467.6$ cm^{-1} which is not surprising because this potential has been explicitly fitted to these peak positions[48]. The *ab initio* and EDIP curves are in pleasing agreement with each other at high frequencies but they are both shifted to the right from the experimental TO peak. We have two comments about this remarkable shift. First, as we have mentioned in Chapter 2, the extreme flattening of the optical phonon

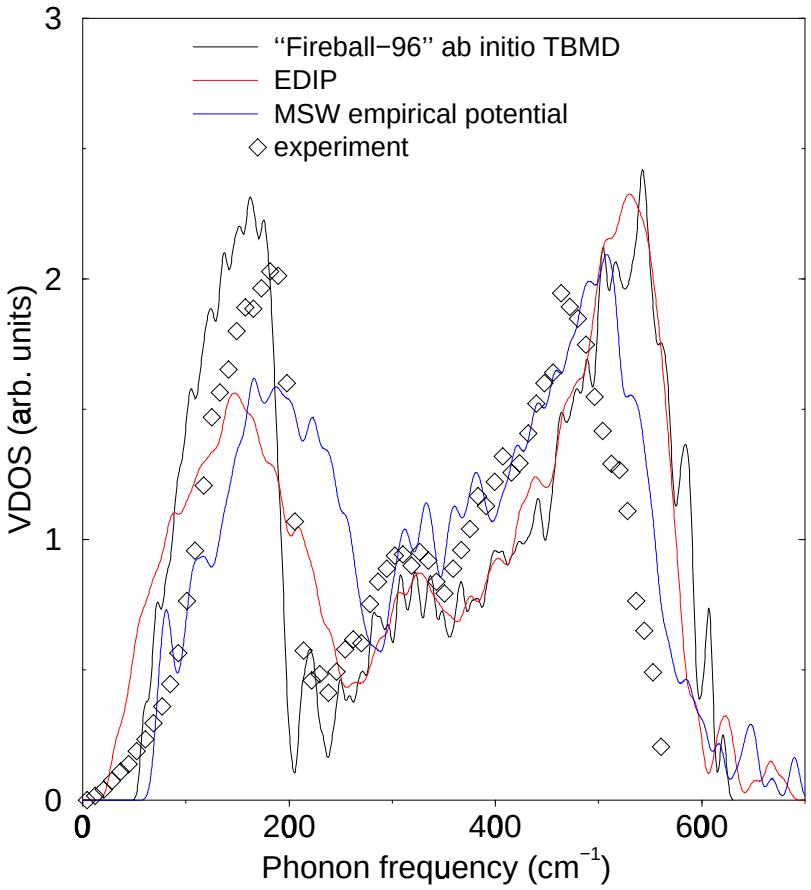

Figure 3.4: **The vibrational density of states for DTW216 model. Black line: calculated with *ab initio* TBMD code "Fireball-96" (SND method). Red line: calculated with EDIP. Blue line: calculated with MSW empirical potential. The experimental results ($\diamond$) are taken from Ref. [4].**

dispersion curves in Si makes simulating the high-frequency part of the vibrational spectrum of a-Si an intricate problem. Second, vibrational properties of a-Si also weakly depend on sample preparation procedure and thus can vary slightly from sample to sample.

The gap present in the calculated curves at low frequencies is an artifact of the finite size of the model — obviously low-frequency phonons with wave length longer than the size of our simulation supercell cannot be excited in the model. In our opinion, out of three different simulation curves presented in Fig. 3.4 the *ab initio* curve gives the best overall description of the low-frequency region of the VDOS.

In Fig. 3.5 we present the VDOS for BM1000 model calculated with the modified SW potential. For this model the VDOS has an additional TO peak shift to higher frequencies. This is because this model's density has been slightly rescaled to fit the equilibrium zero pressure density for Keating and modified SW potentials.

An important issue is the connection between the coordination in the model system and its VDOS. We do not know of any works devoted to the investigation of this question *specifically* for amorphous silicon[64] but numerous calculations of the VDOS of this material by different authors and our own experience with the VDOS computations tell us that the VDOS for a-Si is *not very sensitive* to small changes of average coordination or changes in material composition (i.e. number of three-, four-, five-fold coordinated atoms etc.) which leave its average coordination unchanged.

In order to understand the nature of the spatial localization of vibrational states in our models, we use the dynamical matrix eigenvectors (which 3N components are

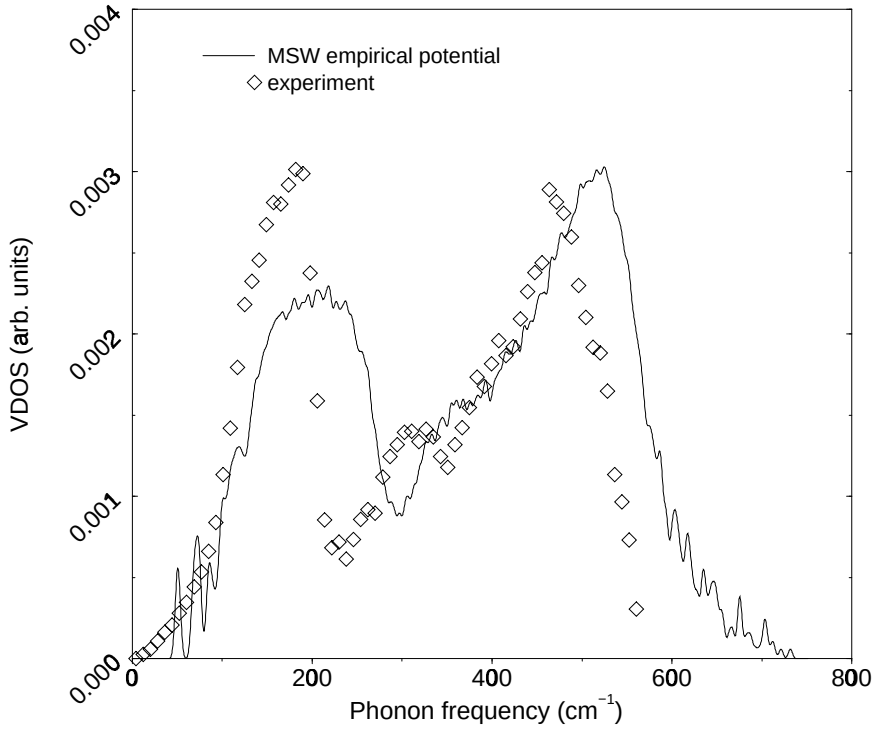

Figure 3.5: **The vibrational density of states for BM1000 model calculated with MSW empirical potential. The experimental results ($\diamond$) are taken from Ref. [4]. The shift of the TO peak to higher frequencies in the model's VDOS is due to rescaled model's density (see Table 3.1 and comments in text).**

just the displacements of every atom in the system along the X, Y and Z axes) to construct the inverse participation ratio (IPR) graphs for these states. The IPR measures the degree of spatial localization for a state (eigenvector) and for *phonons* can be defined as

$$IPR(\omega_i) = 3N \frac{\sum_{k=1}^{N} (\vec{u}_k^i \cdot \vec{u}_k^i)^2}{\left[\sum_{k=1}^{N} (\vec{u}_k^i \cdot \vec{u}_k^i) \right]^2}, \tag{3.6}$$

where $(u_k^i)_x$, $(u_k^i)_y$ and $(u_k^i)_z$ are the displacement components of atom k along the X, Y and Z axes, i.e. an eigenvector $\vec{U}_i$ conjugate to the eigenvalue ω_i^2 in this representation would look like this:

$$\vec{U}_i = \Big\{ (u_1^i)_x, (u_1^i)_y, (u_1^i)_z, (u_2^i)_x, (u_2^i)_y, (u_2^i)_z, \ldots, (u_N^i)_x, (u_N^i)_y, (u_N^i)_z \Big\}. \tag{3.7}$$

Of course, for an orthonormal set of eigenvectors $\{\vec{U}_i\}$ the denominator in 3.6 is equal to unity. With this definition a vibrational mode localized on a single atom would have an IPR of N and a mode that is completely delocalized (i.e. present in approximately equal proportions on every atom in the system) — an IPR of 1.

Finally, for any vibrational mode ω_i we can estimate the activity of every separate atom, examining the components of the eigenvector 3.7 "belonging" to this particular atom and comparing, for example, the sum of their squares on the reference atom, with the sum over all atoms in the supercell. After forming this chart of individual atomic IPRs we can employ this information for dynamical animation of the vibrational mode (for example, by creating a file, consisting of set of frames, each containing coordinates and displacement vector components for every atom in the supercell,

which can be used as an input for *Xmol* molecular display and animation program[65]) or for creating its static equivalent in a form of a gray scale or color map (where atoms are assigned different shades of gray or colors according to their vibrational activity).

3.2.3 Electronic properties

Analogous to vibrations, the electronic properties of a model can be investigated by computing its *electronic* density of states (EDOS) by diagonalizing system's Hamiltonian matrix H_{ij}:

$$\begin{aligned} H_{ij} &= \langle\psi_i|H|\psi_j\rangle, \\ H|\psi_i\rangle &= \varepsilon_i|\psi_i\rangle, \\ |\psi_i\rangle &= \sum_{k,\alpha} C_i^{k\alpha}|\phi_{k\alpha}\rangle, \end{aligned}$$

where H is an *ab initio* or ETB Hamiltonian and $\{\phi_{k,\alpha}\}$ is the basis set (for simplicity, we present the equations for orthogonal basis). Index k counts all the atoms in the system and index α — all the basis orbitals on a single atom. The size of our basis set governs the size of H_{ij}. In case of minimal basis for Si ($\alpha = 4$) the size of the Hamiltonian matrix will be $4N \times 4N$.

The EDOS can then be written out analogously to equation 3.5:

$$EDOS(\varepsilon) = \frac{1}{\alpha N}\sum_{i=1}^{\alpha N}\delta(\varepsilon - \varepsilon_i). \tag{3.8}$$

As usual we use Gaussian broadened form for the members of the sum in 3.8 to plot out a smooth curve. Of course, when H is an *ab initio* Hamiltonian we commit a

usual sin of taking the Kohn-Sham eigenvalues ε_i "literally" i.e. as if they were the real eigenstates of our system.

If the information about the electronic eigenvectors $\{C_i^{k\alpha}\}$ is available, we can also investigate the spatial localization of the electron states and create electron-charge grayscales or colormaps in the same fashion we did that for vibrations in the previous subsection. Of course (see Eq. 3.6) for a given electronic eigenvector its components belonging to some single atom do not form a vector of any kind (like displacement vector for vibrations). Instead they show how much charge density of an electronic state associated with the aforementioned eigenvector is concentrated on the basis functions "belonging" to this atom. For electrons we need to slightly adjust our definition of the IPR:

$$IPR(\varepsilon_i) = \frac{\sum_{k=1}^{N} \sum_{\alpha} (C_i^{k\alpha})^4}{\left[\sum_{k=1}^{N} \sum_{\alpha} (C_i^{k\alpha})^2 \right]^2}. \tag{3.9}$$

A very important question is the connection between the average coordination in our model a-Si system and the features of its EDOS curve. Here, unlike in the VDOS case, it turns out that the bandtail and bandgap regions of the EDOS are *extremely sensitive* to fluctuations of the average coordination. Numerous calculations show that the dangling-bond defect (three-fold coordinated atom) in Si produces a very localized electron state right in the middle of the bandgap. The floating-bond defects (five-fold coordinated atoms) or even four-fold coordinated atoms that are severely strained — i.e. some of atomic bond lengths and/or bond angles deviate significantly from their perfect crystalline values — can also contribute to the bandgap EDOS[66, 67].

As we cross the bandgap going from the valence to the conduction bandtail the spatial localization of the electron states changes dramatically — from completely delocalized Bloch-type in the valence band to exponentially localized in the bandgap (defect states) to delocalized again in the conduction band. The nature of these states and the mechanism of local-to-extended transition in a-Si have been recently explained by Dong and Drabold[68].

For CRN models of a-Si this sensitivity in dependence of the EDOS on the average coordination means that the presence of numerous coordination defects or poorly relaxed pieces of the network in a model makes its electronic properties completely unphysical: even if only one percent of atoms in the model is under/overcoordinated[3], the defect electron states associated with these atoms fill out the bandgap-bandtail region making the bandgap nonexistent. The explanation of this picture is quite simple. Let us imagine a CRN network with a very low concentration of coordination defects. Obviously these defects are situated far away from each other and, because of their local nature, the overlap between the electron wave functions of these defect states is effectively zero. Due to the lack of overlap, the Pauli exclusion principle does not forbid these states to have the same energy. Consequently, what we have in the bandgap is a set of *discrete* energy levels corresponding to the intrinsic defect types in our system, i.e. one level for all dangling-bond defects with approximately the same local environment, one for all floating-bond defects, a couple of levels for various strained four-fold defects etc. Now, when the concentration of defects starts

[3]This is true, of course, for relatively large models, containing 500–1000 atoms or more.

to grow, they become closer and closer to each other in space until they are so close that the overlap integral between their wave functions is nonzero. In this case, if these defects have similar energies (which will eventually happen as the concentration grows) a single defect level has to split into a band due to the Pauli exclusion principle. Finally when we have a whole family of various intrinsic defects with different energies in our system at some point their defect bands start to overlap and conduction percolates across the bandgap. Our experience from studying the spatial localization of the defect states in silicon shows that, despite the exponential behavior of this localization, a state like this still extends out up to the third or even fourth shell of neighbors from its localization center (which is usually a defective atom). This means that a model that has only a few percent of under/overcoordinated atoms *can already be in the percolated state* i.e. — a poor metal instead of a semiconductor. As we know, a-Si is a semiconductor, and consequently this behavior is *wrong* and a model that has nonzero EDOS everywhere across the bandgap cannot be accepted as a reasonable representation of this material, at least for any studies that involve electronic properties of this model.

As we have pointed out earlier in this section, the DTW and BM models are almost perfectly four-fold coordinated and should have no problems reproducing the correct EDOS for a-Si including the bandgap region. In Fig. 3.6 we show the EDOS (Kohn-Sham states) for DTW216 and BM1000 models calculated with the *ab initio* local basis TBMD code "Fireball-96" (SND method). Both models have a well defined bandgap but due to the improvements in the modeling procedure which we have

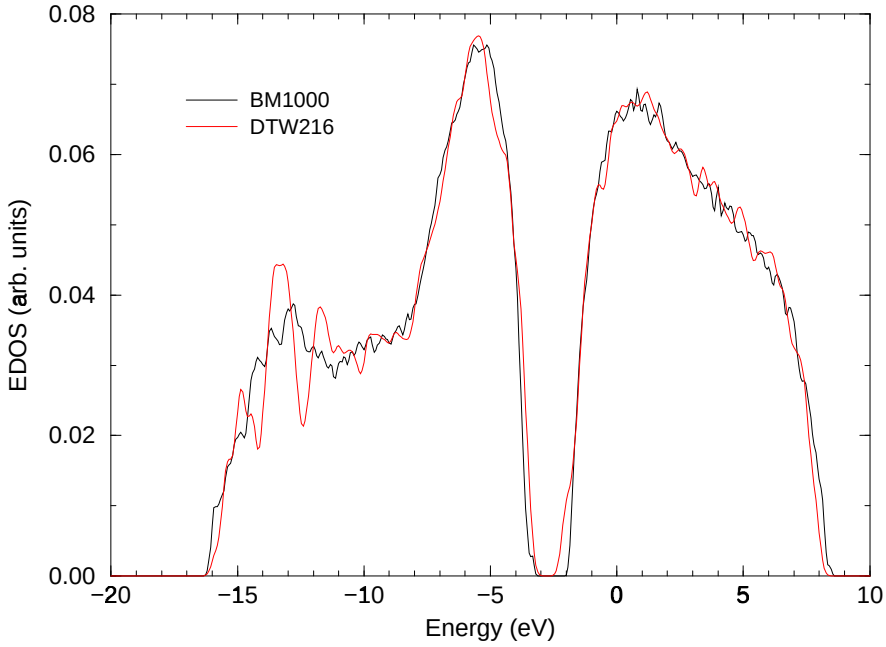

Figure 3.6: **The electronic density of states for DTW216 and BM1000 models calculated with *ab initio* TBMD code "Fireball-96" (SND method).**

discussed in the first section of this chapter the model of Barkema and Mousseau appears to be a better relaxed structure consequently possessing the wider bandgap. This behavior is in agreement with experimental results[69].

In Fig. 3.7 we present the band-gap region and the total EDOS, the bandgap and bandtail states IPRs and the DC conductivity calculated by Dong and Drabold for DTW4096 model[68]. An orthogonal TB Hamiltonian of Kwon *et al.*[33] was used to construct the Hamiltonian matrix for the model. The maximum entropy method[70] was then employed to compute the total EDOS. The eigenvectors of the bandgap

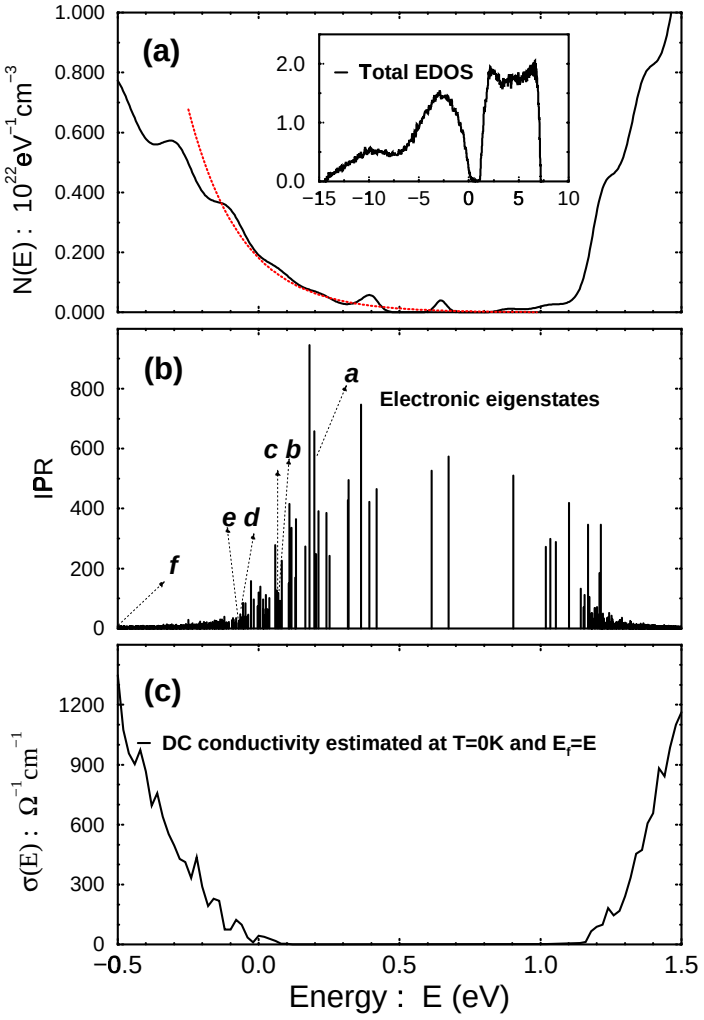

Figure 3.7: **The electronic properties of DTW4096 model (from Ref. [68], reproduced by kind permission). Upper panel: the band-gap region of the EDOS; the valence-band tail is approximated with an exponential (red line). The total EDOS is shown on the insert. Middle panel: spatial localization — represented in the form of the inverse participation ratios (IPR) — of the band-tail and band-gap electron states in the model. Large IPR implies more spatial localization. Lower panel: the estimated DC conductivity as a function of doping (location of the Fermi level).**

region eigenstates were obtained with the Lanczos technique[71] and electrical conductivity of the model was estimated with the Kubo formula[72]. As we can see from the picture, this large model has a significant number of the bandtail states and a few defect states sitting deep in the gap but it is definitely well below the conduction percolation point, which means that the model has a reasonable amount of coordination defects.

Calculation of electronic properties of a CRN model of tetrahedral amorphous semiconductor is probably one of the most stringent tests of model's credibility. The data presented here makes us believe that both families of a-Si models discussed in this section can be regarded as reasonable representations of real material.

3.3 Failure of the "quench-from-the-melt" method for modeling a-Si

3.3.1 Description of the method and its problems

Another well known method for modeling a-Si is the so called "quench-from-the-melt" (QFM) method. The idea of the method is to use MD to mimic the experimental procedure for preparation of a-Si by cooling from the liquid state. Diamond-like Si crystal is taken as initial structure for modeling. The crystal is then melted and the liquid state is formed. After the liquid has equilibrated it is gradually cooled down into an amorphous phase. Finally the amorphous phase is let to equilibrate at

constant temperature or temperature and pressure (the usual temperature is 300 K).

In the QFM method, the simulation procedure requires modeling of the liquid-to-amorphous transition in silicon which is a challenging problem because **(i)** the liquid silicon (l-Si) phase has an average coordination of 6–6.4 and **(ii)** the a-Si phase is four-fold coordinated, and l-Si phase is 10% more dense than the amorphous phase. Due to such drastic difference in coordination and consequently the bonding geometry of the two phases a modeling MD technique is required to adequately describe both of them, which is not always the case. Evidently, *ab initio* or good ETB MD algorithm is preferable here. Due to the difference in the density of phases (the system is supposed to expand while being cooled from the liquid into the solid phase) the MD algorithm should also include some kind of pressure control. Usually in the absence of any pressure-controlling routines the simulation is run at constant volume corresponding to the experimental density of c-Si or a linear rescaling from the l-Si to c-Si equilibrium volume during the phase transition is performed. Both these techniques are of course too crude to give an adequate description of the liquid-to-amorphous transition in silicon. Finally, it is well known that quenching of *real* liquid silicon will result in *crystalline* and not amorphous silicon phase.

Another major difficulty experienced by the QFM method is that on the current level of computer development it is impossible to simulate equilibration/annealing times comparable to their experimental analogs with conventional MD techniques. Right now simulated annealing MD times for a system of hundreds of atoms treated by two- and three-body empirical potential (the most computationally effective case)

are in the order of tens to hundreds of nanoseconds, while during the experiment an a-Si sample could be annealed for minutes and even hours. Because of these incomparably shorter equlibration times the QFM amorphous models almost always have some remains of the "parent" liquid phase in them that did not have enough time to fully relax. These remnants usually manifest themselves in the model's structural properties as a small peak at 60° in the bond-angle distribution, and an unphysically large number of coordination defects, especially five-fold atoms — obvious features showing that some atoms in the network still have their local environments close to hexagonal (six-fold) and not tetrahedral.

Unlike the WWW method, the QFM modeling procedure does not incorporate any mechanism *to enforce* the four-fold coordination, so that, due to the aforementioned difficulty with equilibration times, the coordination defects and highly strained regions of the network do not have time to fully relax. And as we have pointed out earlier, the presence of an unrealistically high number of coordination defects in a model deteriorates its electronic properties making them completely unphysical (metallic instead of semiconducting in the case of a-Si), and this is a *major flaw* experienced by the models created with the QFM method.

3.3.2 Review of the existing models

During the last twelve years, modeling of a-Si with the QFM method has been a very active field. Models have been constructed with every MD technique available (see Chapter 2). Here we discuss the properties of the existing QFM models starting,

analogously to our methodology review, with those created with *ab initio* MD.

The first attempts to model a-Si with *ab initio* MD have been made by Štich, Car and Parrinello[73], and Drabold *et al.*[74]. The former group has used a plane-wave basis MD code based on the method of Car and Parrinello[21] and the latter — a local basis TBMD code utilizing the Sankey-Niklewski-Drabold method[23]. The model of Štich, Car and Parrinello (SCP) is the real QMD model, it has been created by rapid cooling of the liquid and subsequent constant temperature annealing without any serious pressure control: during the simulation of liquid cooling to the amorphous phase the volume of a supercell has been simply linearly expanded from the equilibrium l-Si to c-Si phase volume. The model of Drabold *et al.* cannot be regarded as a true QFM model: in order to overcome the mentioned above difficulty of "freezing in" too many unrelaxed defects by rapid cooling of the liquid, Drabold *et al.* have elected to quench to the amorphous phase from a so called "incompletely melted" configuration that is sufficiently disordered not to quench back to c-Si phase but much closer to a-Si in bonding geometry than l-Si. This deviation from the standard QFM routine results in the electronic properties of model of Drabold *et al.* being much more reasonable than that of SCP model. The former one has a band gap with only three defect states in it — two due to three-fold coordinated dangling-bond states and one due to a highly strained four-fold atom. The latter has approximately 3.5% of coordination defects and no clear band gap. We must point out that both of these models are very small (only 64 atoms per supercell) which presents an additional computational difficulty:

the Brillouin zone for such a small supercell is large enough to render the Γ-point approximation (flat electronic bands) invalid. To receive correct interatomic forces, not only the Γ-point but other points in the Brillouin zone should be sampled[74]. Due to much higher computational efficiency of their MD scheme Drabold and coworkers have been able to do that, while SCP have evaluated their forces at the Γ-point only which makes their results even less reliable.

Other *ab initio* MD models for a-Si we can mention as well are of Lee and Chang[75] (64 atoms, "incompletely melted" starting configuration), Takeuchi and Garzón[76] (a-Ge: 64 atoms, no pressure control) and Cooper, Goringe and McKenzie[77] (64 atoms, no pressure control). All of these models have a few percent of coordination defects which result in a substantial density of defect states in the band gap.

Some of the structural properties of Štich-Car-Parrinello and Cooper, Goringe and McKenzie models are presented in Table 3.2.

Of the ETB based QFM models of a-Si we would like to mention the ones constructed by Servalli and Colombo[78] (SC), Kim and Lee[79] (KL), and the recent models of Urbassek and Klein[80] (UK).

Both SC and KL employ the TB Hamiltonian of Goodwin, Skinner and Pettifor[31] in their MD scheme. Neither of the schemes has true pressure control. The KL simulation has been performed at constant volume corresponding to the experimental density of c-Si and resulted in a model with only approximately 83% of four-fold

Table 3.2: **Structural properties of "quench-from-the-melt" models for a-Si created by Štich, Car and Parrinello (CP), Cooper, Goringe and McKenzie (CGM), Kim and Lee (KL), Urbassek and Klein (UK), Kluge, Ray and Rahman (KRR), Luedtke and Landman (LL) and Justo *et al.* (JBK). C_n is the percentage of atoms with coordination n; n_C is the average coordination.**

	SCP	CGM	KL	UK	KRR	LL	JBK
Ref.	[73]	[77]	[79]	[80]	[82]	[84]	[44]
Type	LDA	LDA	ETB	ETB	SW	SW	EDIP
N	64	64	64	128	216	588	1728
T (K)	300	300	0	300	472	360	300
C_3 (%)	0.2	4.7	3.2	1.5	0	0.5	0.23
C_4 (%)	96.6	92.6	82.8	96.9	88	87.8	94.43
C_5 (%)	3.2	1.6	12.5	1.6	12	11.5	5.34
n_C	4.03	3.96	4.28	4.001	4.12	4.12	4.054
$\langle\theta\rangle$	108.32	107.38	106.7		108.4	108.3	108.6
$\Delta\theta$	15.5	15.2	16.3		13.6	14.7	14.0

coordinated atoms and $\Delta\theta = 16.3^o$ (see Table 3.2 for more properties). With such coordination and residual strain the electronic properties of the model are quite poor. In the SC simulation the linear volume rescaling scheme is used. Their best 64 atom model has approx. 96% of four-fold coordinated atoms (average coordination of 4.02). The EDOS for their 216 atom model which is claimed to have the same structural properties as the 64 atom models still shows significant density of defect states in the bandgap region.

The models of Urbassek and Klein have been constructed with the TB Hamiltonian of Frauenheim *et al.*[37] which includes s, p and d orbitals. The simulations have been conducted at zero pressure, employing the pressure control technique developed by Klein[81]. The resulting models, although having some coordination defects, possess a clear bandgap which can probably be attributed to the absence of the external pressure induced strain in the model. The structural properties of 128 atom UK model are presented in Table 3.2. We consider these models to be the best models created with the QFM method. Unfortunately the models are very small — 64 and 128 atoms — and can hardly be used in serious investigations of bulk properties of a-Si.

The first QFM models for a-Si and a-Ge created with classical (empirical potential) MD in the late eighties are due to Ding and Andersen[46] (DA), Kluge, Ray and Rahman[82] (KRR), Biswas, Grest and Soukoulis[83] (BGS) and Luedtke and Landman[84] (LL). DA have created 216 and 512 models of a-Ge and studied their

phonon dispersion curves using constant volume MD with the SW potential refitted for germanium.

KRR and LL have also employed the SW potential in their MD schemes but in their case the zero pressure simulations have been made using the pressure control techniques of Andersen[85] and/or Parrinello-Rahman[86]. The serious problem encountered was that at zero pressure the standard SW potential is incapable to quench the liquid into an amorphous structure directly and forms a supercooled liquid state instead[87]. Different approaches have been taken to overcome this difficulty: KRR have applied negative pressure to the liquid to help it expand and LL have magnified the three-body interaction term in the potential during the cooling procedure. In both cases the resulting models contain numerous coordination defects (see Table 3.2). The VDOS curves for both models show the same shift of the TO peak to higher frequencies. Mercer and Chou[88] have calculated the EDOS of the LL model with the TB Hamiltonian of Chadi[30] and found high density of defect states in the bandgap region.

BGS have made use of Biswas-Hamann potential[41] and constant volume MD technique in their simulations creating 216, 512 and 2000 atom models of a-Si with 10–15% atomic density of coordination defects. The VDOS curve for their models also has the TO peak shift to the higher frequencies. The 216 atom BGS model has been then used to study the electronic structure of dangling and floating bonds in a-Si[66]. The EDOS curve for the model, presented in Ref. [66], clearly shows the presence of numerous defect states that effectively fill out the band gap.

The more recent empirical potential QFM models have been constructed by Ishimaru, Munetoh and Motooka[89] (IMM), Justo *et al.*[44] (JBK) and Bording[59] (for a-Ge). Both IMM and Bording have used the Tersoff potential[42] in their simulations and received structures containing approximately 10% of coordination defects. No pressure control has been applied in IMM's case, while Bording has used crude volume rescaling procedure to perform constant pressure MD. Surprisingly the VDOS curve for the IMM model is in good agreement with the experimental results of Kamitakahara *et al.*[4] displaying no TO peak shift.

The JBK model has been constructed with the environment-dependent interatomic potential of Bazant and Kaxiras[43] (EDIP). The standard pressure control techniques[85, 86] have been used for performing zero pressure MD. Unlike the SW potential, EDIP has been able to quench the liquid directly into the amorphous phase with almost 95% of four-fold coordinated atoms. The structural properties of the model are presented in Table 3.2. The EDOS for the model has been calculated by Bernstein *et al.*[38] and shows significant density of defect states in the bandgap region.

Finally we would like to mention one additional work where the WWW model of a-Si has been used for close to the melting point temperature empirical MD simulations. In 1991 Holender and Morgan created large (up to 10^5 atoms) models of a-Si[90, 47] stacking up the 216 atom WWW model supercells and heating them to get rid of periodicity. The SW potential was used with normal as well as with magnified three-body interaction term; the pressure control algorithm was implemented with the

technique of Andersen[85]. After the heating and subsequent relaxation to 0 K the perfect tetrahedral bonding was lost and the resulting models had 6% of coordination defects[4]. Holender and Morgan have also calculated the EDOS for their models[91] with the TB Hamiltonian of Chadi[30]. The best EDOS curve with only a couple of defect states in the band gap has been obtained for a variant of their model where eight 216 atom WWW blocks were put together but only 12.5% of the randomly chosen atoms were given high kinetic energy to destroy the periodicity.

In conclusion of this section we would like to point out that in our opinion the QFM method is inferior in quality of generated models to the WWW method because it consistently produces models with unphysically large amount of coordination defects and does not allow for adequate relaxation times to reduce strain in the model's network. As a result the electronic properties of the models are ruined which *does not happen* for the models created with the WWW method.

3.4 Other methods

3.4.1 Reverse Monte Carlo method

The reverse Monte Carlo (RMC) method is a technique for creating structural models of materials using experimental data as an input fitting information. Multiple atomic species materials and materials of unknown stochiometric composition

[4]When the SW potential with magnified three-body interaction term was used. For the standard SW potential the coordination defects concentration raises to 26%.

can be modeled (like ternary chalcogenide glasses)[92]. Almost any experimental or computed with a higher precision numerical method curve can be used for fitting. The most widely used fitting data sets are:

- the desired system coordination,
- the desired bond angle distribution,
- the pair correlation function $g(r)$,
- the x-ray diffraction data like structure factor $S(q)$,

but even the VDOS or EDOS curve can be employed in the same fashion. This fitting data is regarded as *constraints* imposed on the system.

The short description of the RMC modeling strategy is the following (the details are given in Ref. [93, 94]):

1. The starting configuration of particles at the desired density is created. A set of "constraint curves" $F_i^c(x)$ is calculated for it, i.e. if we want to fit to the experimental $g(r)$, we calculate the model's pair correlation function $g^c(r)$; for an additional fit to the experimental $S(q)$, we calculate the $S^c(q)$ for the model etc.

2. The goodness-of-fit factor

$$\chi_0^2 = \sum_i \frac{1}{\sigma_i} \sum_x \left(F_i^c(x) - F_i^e(x) \right)$$

is calculated, where $F_i^e(x)$ are the experimental data sets (constraints) to which the model is being fitted to. σ_i is the standard deviation of the experimental data set i.

3. A new trial configuration is created by randomly moving one particle. The set of $F_i^c(x)$ and factor χ^2 (χ_n^2) are calculated for the new configuration.

4. If $\chi_n^2 < \chi_0^2$ the move is accepted. If not, the move is accepted with the Metropolis-like probability $p = \exp\{-\frac{1}{2}(\chi_0^2 - \chi_n^2)\}$.

The modeling process progresses by repeating steps 3 and 4; the model is regarded to have achieved structural equilibrium when the goodness-of-fit factor starts to oscillate around a given value (which depends on σ_i) without any further improvement of the fit. Note that this method does not require any interatomic potentials which is of course an advantage.

The RMC method has been applied to modeling of a-Si by Pusztai and Kugler[95] and a-Si, a-C and a-Ge by Gereben and Pusztai[96]. In both cases models were fitted to experimentally measured structure factor with an additional requirement of 100% four-fold coordination and bonding close to tetrahedral. The constructed models contained up to 99% of four-fold coordinated atoms but they also contained a lot of internal strain due to completely artificial preparation procedure. Recently Rosato and Celino[97] have attempted to relax an RMC-produced model of a-Si with ETB MD (empirical TB Hamiltonian of Kwon *et al.*[33]) and study its vibrational and electronic properties. As constructed, their model had 88.5% of four-fold coordinated

atoms but after the relaxation procedure this value dropped to 75% (with the average coordination of 4.5), which resulted in very poor vibrational and electronic properties.

Our general conclusion about the applicability of this method is that the RMC is a useful technique for modeling systems where *no other modeling method is available.* It is definitely not a method of choice for modeling amorphous silicon.

3.4.2 Activation-relaxation technique

The activation-relaxation technique (ART) is a powerful method of investigating the long-time dynamics of glassy materials that can also be used for modeling. It was introduced by Barkema and Mousseau[98, 99] in 1996 and applied for modeling of a-Si and a-GaAs[100] and studying of relaxation and diffusion mechanisms in a-Si[101].

As we have pointed earlier, the major problem of the conventional MD techniques is their short simulation timescale comparable to only a few atomic oscillations. But in disordered or glassy materials many important microscopic structural phenomena often occur at timescales that are orders of magnitude longer than typical phonon frequencies. Instead of following the atomic oscillations (like in MD), ART allows us to sample the energy landscape for a system of interest in an attempt to find its global energy minimum, thus performing more radical structural relaxations of our system than those that are possible with MD techniques. The general idea of the method is given below.

At low temperatures our system remains at some local energy minimum in the configurational energy landscape. The energy barriers surrounding this minimum

are typically much higher than system's temperature and only rare fluctuations of system's thermal parameters will allow it to jump over a barrier and move to a different energy minimum. For an MD simulation this means that our system can spend all its time around this minimum and never escape it because a fluctuation required to push it over an energy barrier is so rare that it never occurs during the typical time interval an MD simulation can achieve. ART has been developed to overcome this difficulty by providing the relaxation scheme based not on individual atomic motions but rather on *events* which can include complex simultaneous motions of many atoms.

An event in ART is defined as a move from one local energy minimum to another. Each move contains of two separate steps: *activation* and *relaxation*. The activation step starts with pushing the system out of equilibrium (energy minimum). Then the system is moved "uphill" in the configurational energy landscape to the nearest saddle point along a path of minimal energy. After the system reaches the saddle point it is brought "downhill" to the next energy minimum. For a system of N particles this technique effectively reduces the $3N$-dimensional configurational space (most of which is highly energetically unfavorable and is never visited at low temperatures) to a space consisting only of the local energy minima and paths connecting them.

ART can use any method for computing atomic forces — from classical interatomic potentials to full *ab initio* techniques. At the same time, even when employing the *ab initio* forces it stays much more computationally efficient than first principles MD.

Using ART, Barkema and Mousseau[98] have constructed 1000 atom model for

a-Si with average coordination of 3.97 and $\Delta\theta = 9.97°$. The atomic forces have been obtained with the SW potential with the three-body term increased by 50%. The initial configuration have been taken as a random closely packed structure at c-Si density. In general, models created with ART employing the modified SW potential have structural properties as good as the properties of the best QFM models created with *ab initio* or accurate ETB MD.

Chapter 4

Vibrational signatures of nanovoids in a-Si and a-Si:H

The computational project, presented in this chapter, investigates two important issues related to vibrational properties of a-Si and a-Si:H. It is well known that a-Si/a-Si:H, grown using conventional techniques like chemical vapor deposition, contains nanovoids in its structure[1, 7, 8, 9]. Vibrational properties of voids and coordination defects introduced in the a-Si CRN models have been studied by Biswas *et al.*[102, 103] and by Chehaidar *et al.*[104]. Both groups have used models of average quality and empirical potentials to perform MD simulations and compute dynamical matrices and their results appear to be in contradiction. However in both cases a conclusion can be made that the presence of defects (like voids) in the CRN gives rise to low-energy (low-frequency) vibrational states that are spatially localized on these defects. An immediate question arises: what is the connection between these states and the celebrated tunneling or two-level states in glasses[12, 13] that are utilized to explain

anomalous (non-Debye) low-temperature specific heat behavior in these materials? Both groups have only speculated on this subject but failed to make any rigorous conclusions about the nature of these localized low-energy states and their possible kinship to the two-level states. Finally, a recent experimental work with a new hot wire form of a-Si:H has been reported[105] which connects the absence (very low concentration) of voids in the material with the absence of low-energy vibrational excitations in it (and consequently excellent semiconducting properties of the new material).

Motivated by these results we have performed studies of CRN models for a-Si, and models with hydrogenated and unhydrogenated voids introduced into the network, to understand how the presence of voids changes vibrational properties of the material and what is the relation between these properties and the two-level states. On the first stage of our investigation we have examined small models of a-Si without voids and a-Si:H with hydrogenated voids using *ab initio* MD technique[106] and on the second stage we have studied large models of a-Si without voids and a-Si with voids employing empirical MD technique[107, 108]. The detailed description of the project and the discussion of the obtained results are given below.

4.1 *Ab Initio* MD studies of vibrational properties of voids in a-Si:H

4.1.1 Model construction and calculations

Before we can actually study the vibrational properties of voids in a-Si/a-Si:H an appropriate model of the material containing a void should be constructed. In this section, due to the limitations of the *ab initio* MD technique that we plan to use, we build only small models with voids (less than 216 silicon atoms). The 216 atom model for a-Si (without voids) generated with the WWW scheme[51] by Djordjevic, Thorpe and Wooten[52], DTW216, is employed as a "base" for construction of models for a-Si:H with voids in the bulk. The structural, vibrational and electronic properties of DTW216 are presented in section 3.2.

For our MD simulations we use the *ab initio* local basis TBMD code "Fireball-96" developed by Sankey and coworkers[23]. In equilibrium geometry search, we consider our models fully relaxed when total forces on any atom in the supercell are less than 0.03 eV/Å.

In the first step (which we need to perform only once) we relax the DTW216 model, obtaining its equilibrium geometry configuration by dynamical quenching. In our case relaxing the model resulted only in minor network rearrangements. The radial distribution function, obtained for the relaxed model, appeared to be in good agreement with experimental data, as was the case for the original model before

relaxation.

In the second step we remove a cluster of Si atoms, thus creating a void in the silicon network. The removal of these atoms out of the network results in dangling bonds; we terminate them with hydrogen atoms. In the models, presented here, we consider entirely passivated networks, where *every* dangling bond in the network is terminated by a hydrogen atom, initially placed directly on the bond 1.5 Å away from a Si atom. This procedure is illustrated with Fig. 4.1.

After discarding the chosen cluster of Si atoms and saturating the dangling bonds on the surface of the void with hydrogen atoms we perform the third step — another MD quench, which gives us the equilibrium configuration for the new structure with void. At this point the actual number of relaxation steps required to make forces on every atom sufficiently small varies greatly, depending on the size and form of the void.

When the equilibrium geometry for the model is obtained we construct and diagonalize the dynamical matrix for it[63] and then, using its eigenvalues and eigenvectors, compute model's VDOS, IPR and "vibrational activity" colormaps for certain vibrational modes.

4.1.2 Discussion of results

In this subsection we discuss our results received for two different a-Si:H models with voids. The first model has five Si atoms removed and twelve H atoms added (we refer to it as "small void" model), the second one has 23 Si atoms removed and 36 H

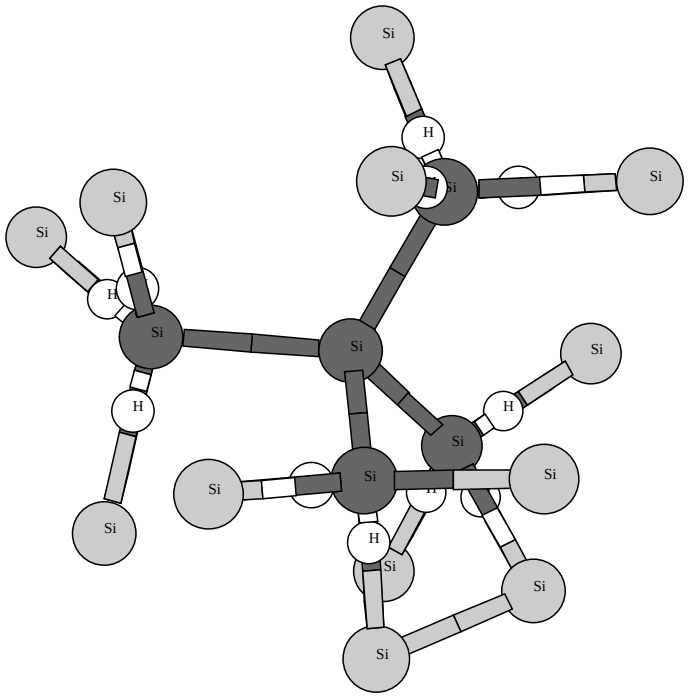

Figure 4.1: **Creating a hydrogenated void in CRN model. Here Si atoms pictured in dark gray are the ones we intend to remove, thus creating a void. Si atoms represented by light gray are the nearest neighbors of the atoms that we are removing. H atoms represented by small white spheres are placed on the bonds between the atoms that we are removing and their nearest neighbors 1.5 Å away from the latter.**

atoms added ("large void" model).

To be able to compare the results for our a-Si:H models and results, obtained for voidless DTW216 model, which serves as our "reference" model, we have performed the set of all calculations, described in the previous subsection, for DTW216 as well as for both models containing voids.

In Fig. 4.2 we present our results for voidless DTW216 model of a-Si; note that the calculations show that for a model of this size there are no vibrational states present with frequencies up to approximately 55–60 cm^{-1}. Now, if we compare these results with the results obtained for the "small void" model, shown in Fig. 4.3, and restrict our attention only to low energy states, we can see that for a model with void a new vibrational mode emerges at 32 cm^{-1} and this mode has high IPR and can be considered spatially localized. The colormap for the aforementioned mode is presented in Fig. 4.4. It enables us to estimate where this vibration is localized in the supercell and how it decays in space. We can see that the mode has rather complicated structure, although it is mostly localized around the surface of the void and decays very rapidly when we move away from the void; there are certain directions where it decays more slowly and a whole cluster of vibrationally active atoms to the side of the void. For comparison in Fig. 4.5 we present one of the low-energy (64.4 cm^{-1}) modes for "small void" model that has relatively low IPR and, according to the picture, is rather uniformly distributed in space.

Now comparing the results for the first two models, discussed in the previous paragraph, with the results received for the "large void" model (Fig. 4.6) we can see

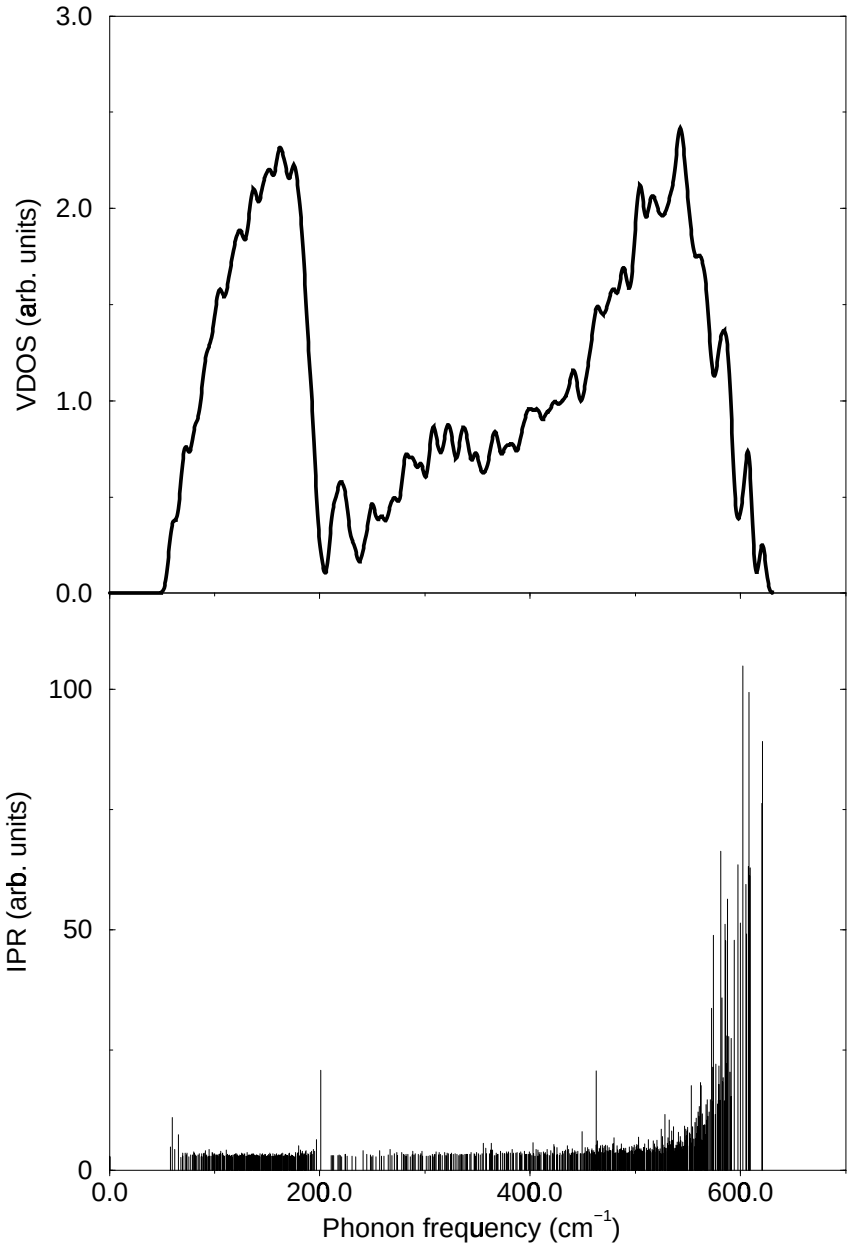

Figure 4.2: **VDOS and IPR for DTW216 model calculated with "Fireball-96".**

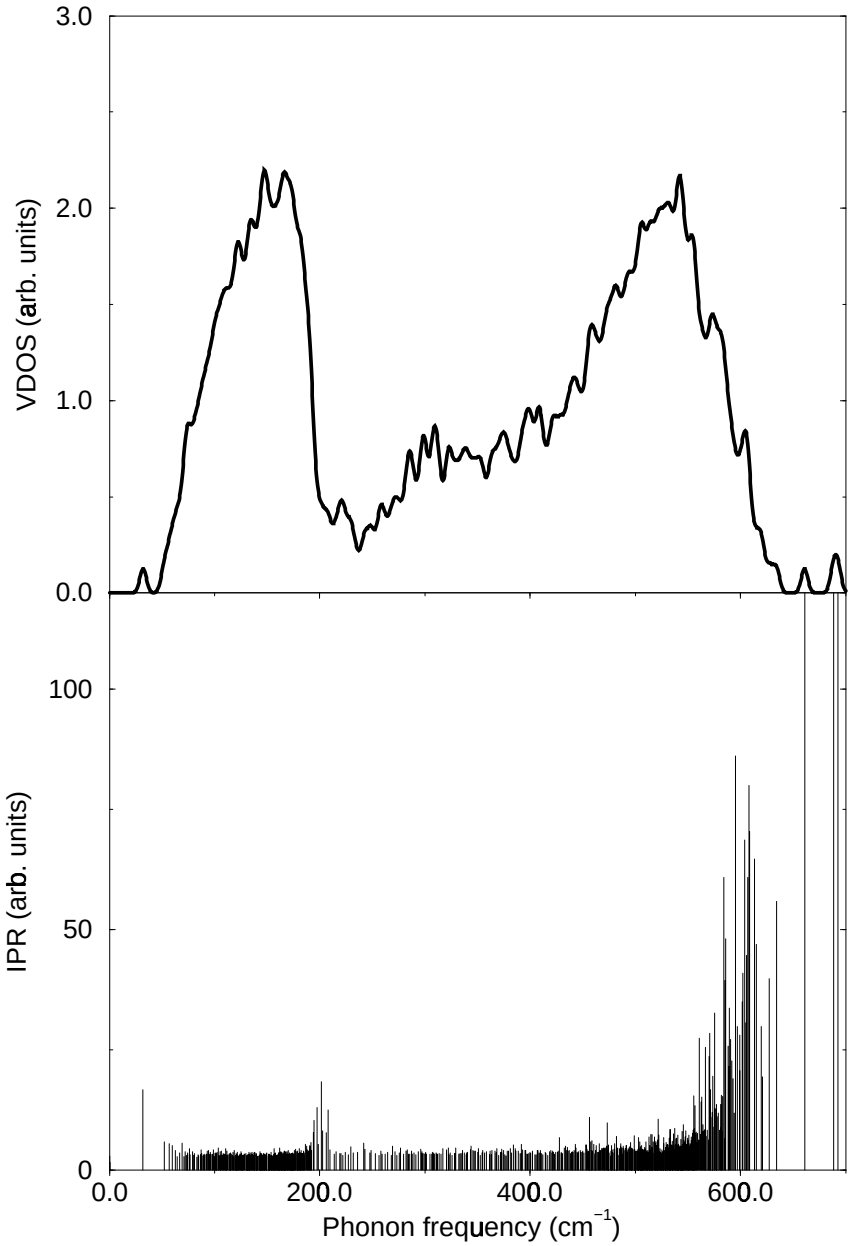

Figure 4.3: **VDOS and IPR for "small void" model (211 Si atoms, 12 H atoms) for a-Si:H with void (high energy modes are not shown) calculated with "Fireball-96".**

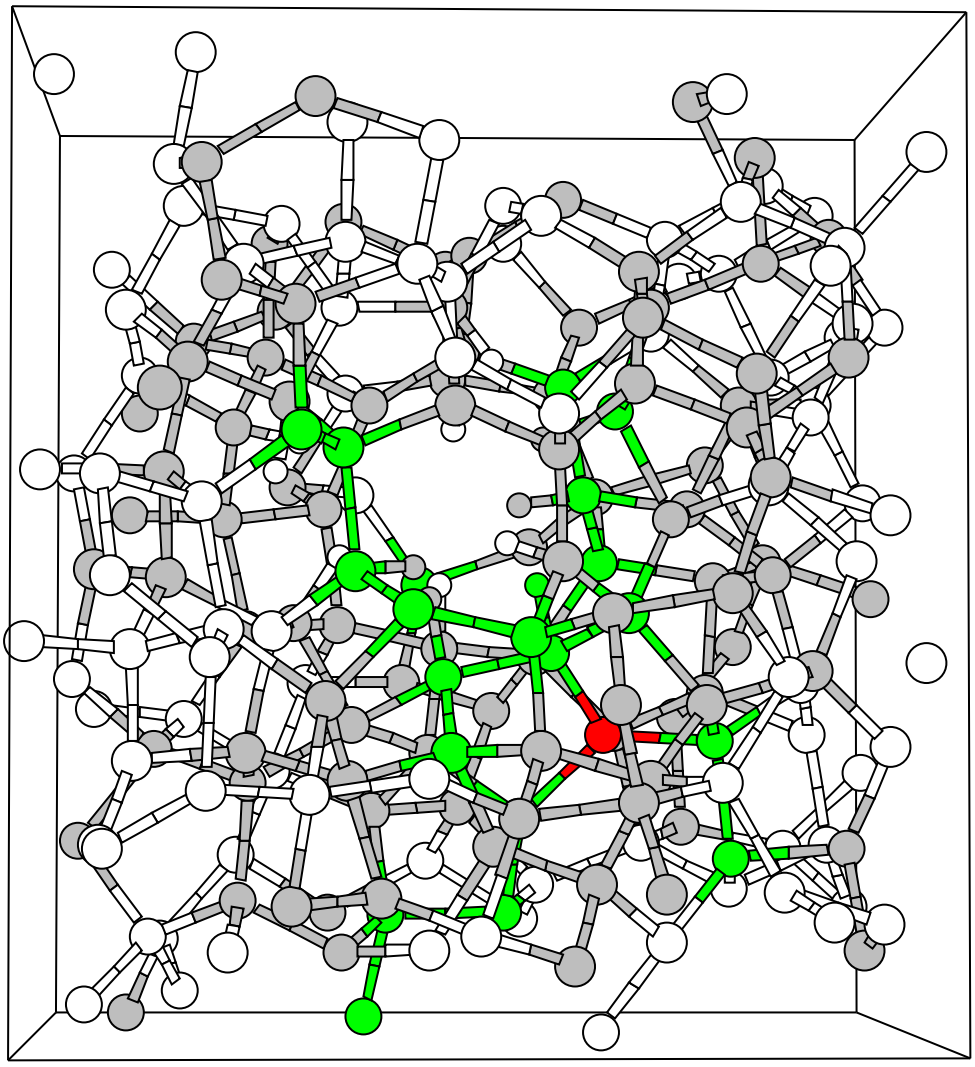

Figure 4.4: **Localized low-energy vibrational mode for "small void" model. Phonon frequency is 32.0 cm^{-1}. Here atom pictured in red accounts for more than 10% of total supercell excitation. Atoms, represented by green, light gray and white, account for more than 1 and up to 10%, more than 0.1 and up to 1% and less than or equal to 0.1 % of total supercell excitation accordingly.**

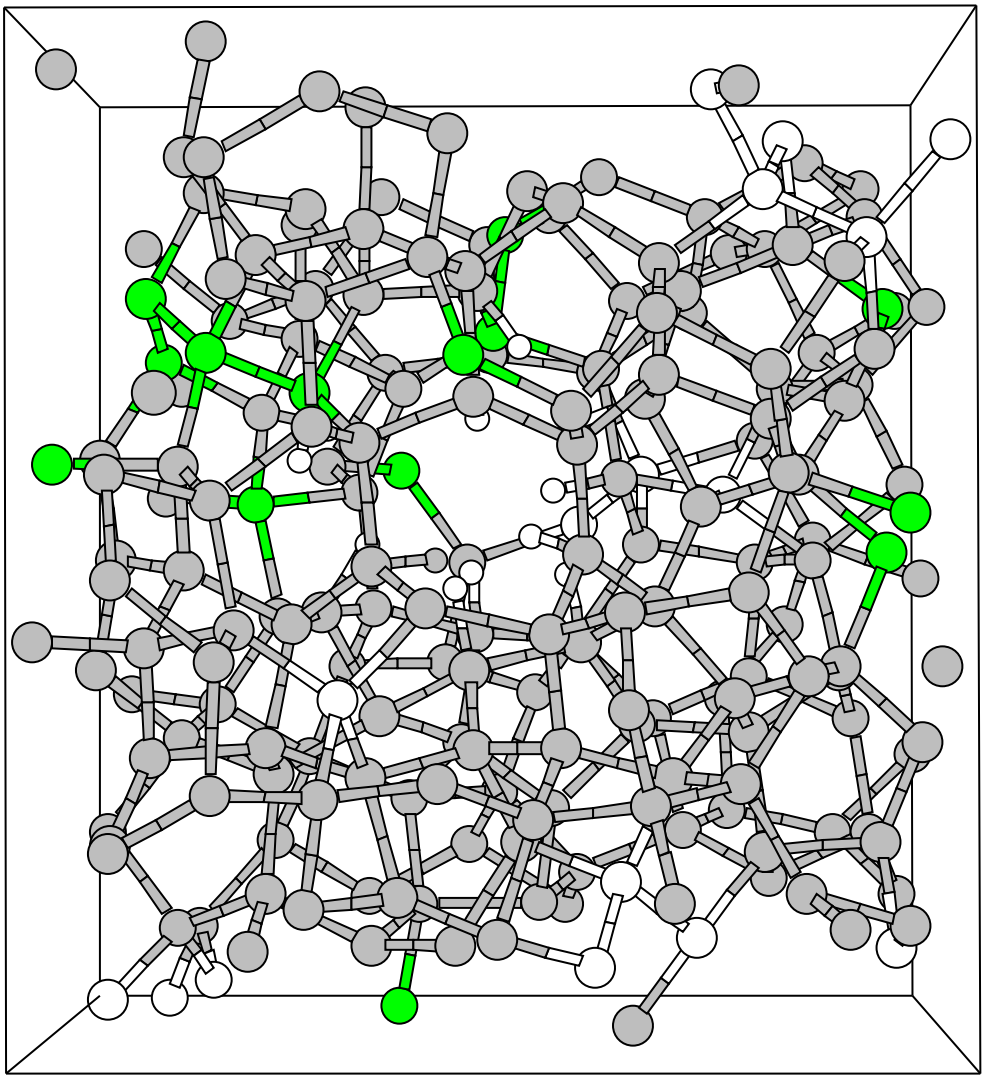

Figure 4.5: **Low-energy vibrational mode for "small void" model which is delocalized. Phonon frequency is 64.4 cm^{-1}. Color conventions the same as for Fig. 4.4.**

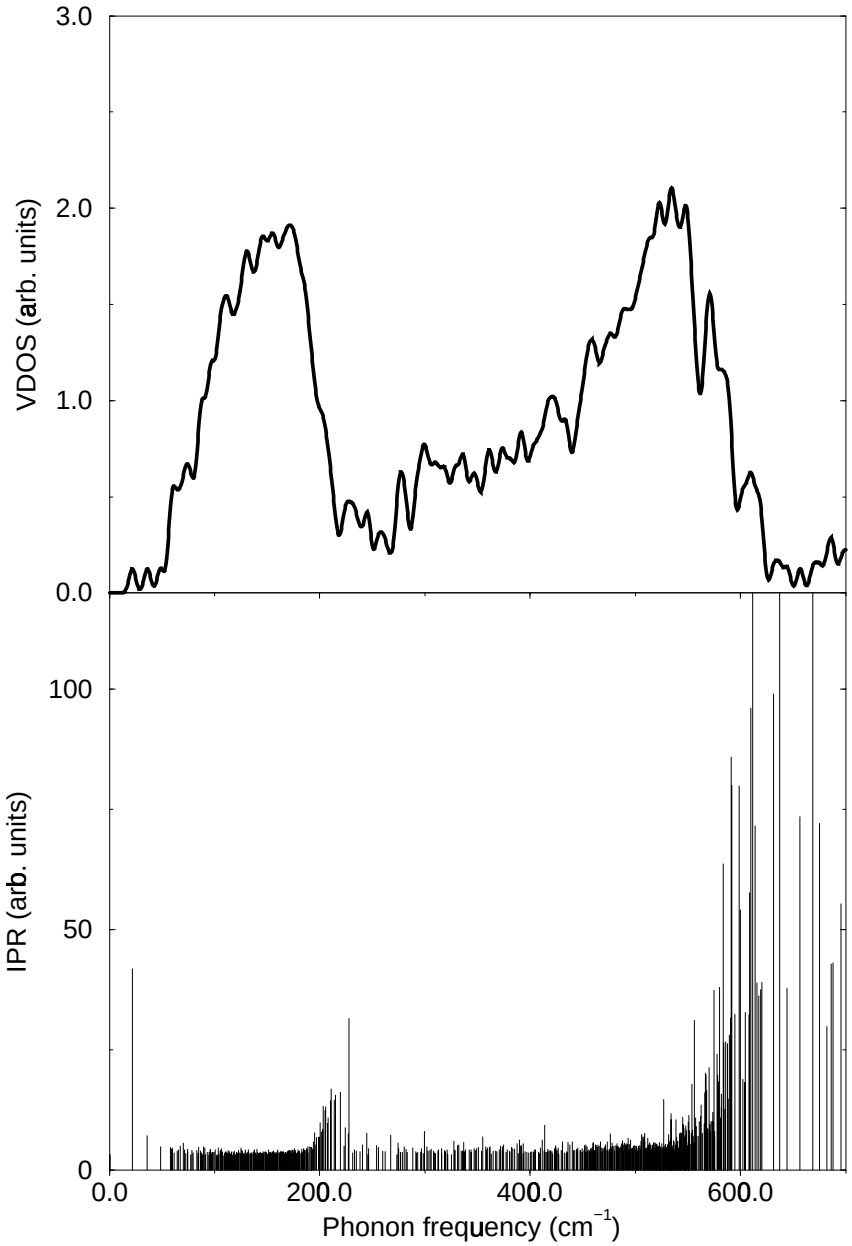

Figure 4.6: **VDOS and IPR for "large void" model (193 Si atoms, 36 H atoms) for a-Si:H with void (high energy modes are not shown) calculated with "Fireball-96".**

that now we have three new low energy states, but only one of them, at 21.8 cm^{-1} has high IPR (more than two times larger than for the similar mode in "small void" model) or is localized. Examining the colormap for this mode, presented in Fig. 4.7 we also notice that spatial localization of the mode is quite similar to "small void" model mode with the exception that the former decays much faster and its localization on a cluster of Si atoms to the side of the void is much sharper.

Our hydrogenated models also produce highly localized states at 600–630 cm^{-1} (hydrogen bend) and 2000–2200 cm^{-1} (hydrogen stretch). Other hydrogen related states, corresponding to mixing of the first two, fill out the region of 700–1000 cm^{-1}. A colormap for one of these modes is shown in Fig. 4.8.

4.1.3 Some conclusions

Studying the models for a-Si:H with voids we have found localized low-energy modes in their vibrational spectrum, which is in general agreement with the results of Chehaidar *et al.*[104]. The nature of these modes is quite complicated but evidently connected with the existence of voids — for both localized low-energy modes considered a number of silicon atoms located close to the surface of the void exhibits high vibrational activity.

The principal shortcoming of the calculations presented here is of course the very small size of the models, which leads to artificial interaction between a void and its "ghost" images in the neighbor supercells. For the "small void" model, this problem is apparently less serious, since the void-induced low-energy state is well localized. The

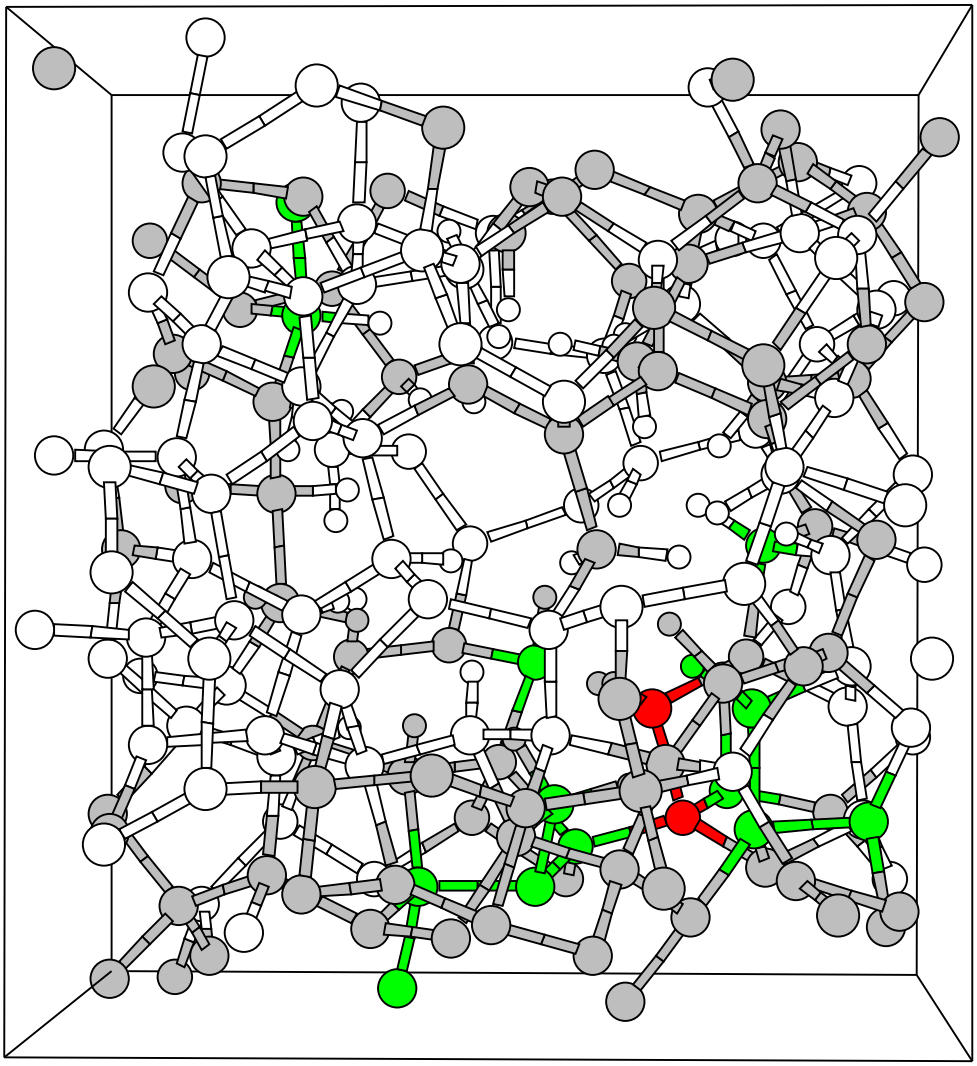

Figure 4.7: **Localized low-energy vibrational mode for "large void" model. Phonon frequency is 21.8 cm^{-1}. Color conventions the same as for Fig. 4.4.**

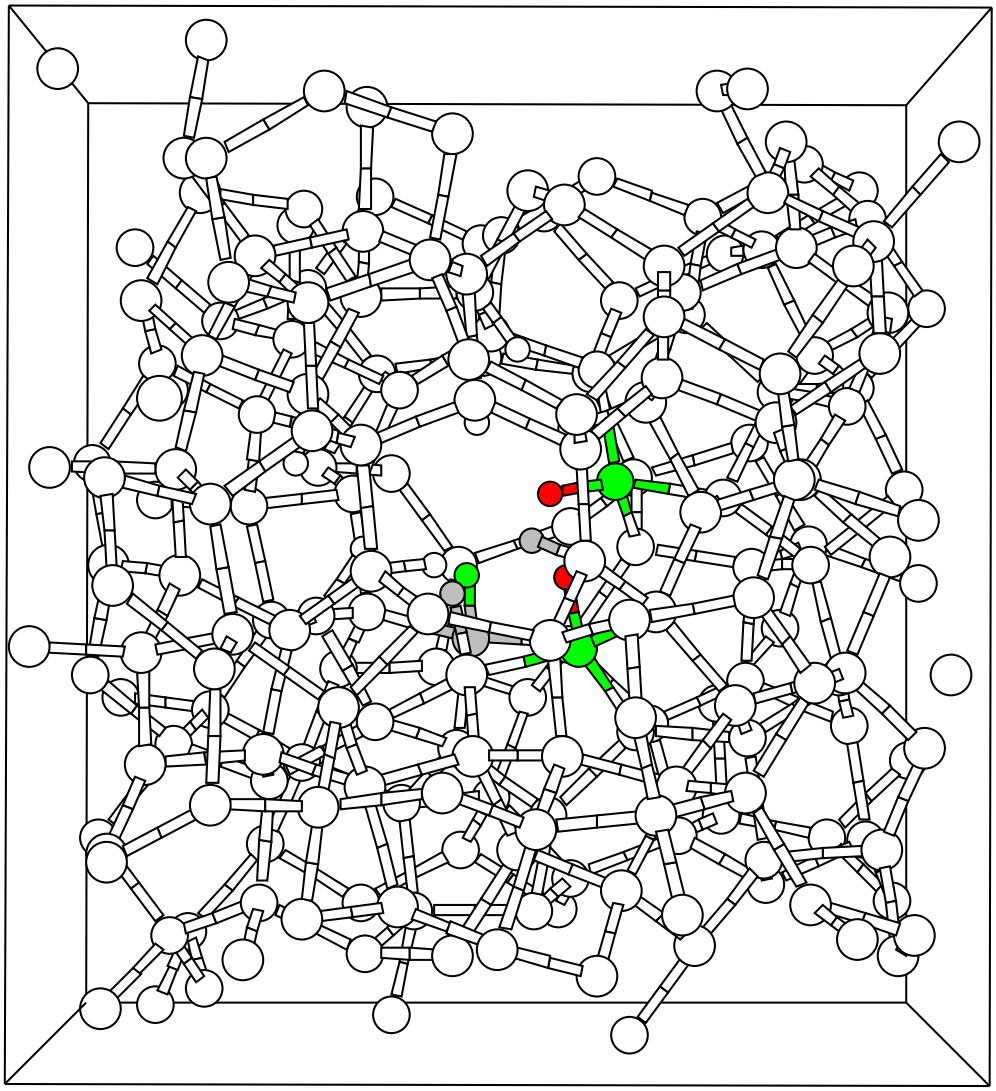

Figure 4.8: **An example of localized high-energy hydrogen mode for "small void" model. Color conventions the same as for Fig. 4.4.**

main point of this work is that voids lead to low-frequency modes, and contribute (along with extended low-frequency modes) to the vibrational spectrum. Because they are localized, they would not be relevant to thermal conduction, and might have a long lifetime.

Finally, making a connection between our results and the peculiar properties of the new hot wire form of a-Si:H developed by X. Liu *et al.*[105], our work suggests that indeed the small density of voids in their material should lead to a reduction in low-energy vibrational excitations.

4.2 Empirical MD studies of vibrational properties of voids in a-Si

As we have pointed out earlier an obvious disadvantage of our previous calculation[106] is a very small size of the supercell containing a void. In order to gain better understanding of the nature of the void-related vibrational modes we need to perform similar calculations with larger and consequently more realistic models for a-Si. Of course as the size of a model increases we have to "downgrade" our computational techniques to empirical potentials, thus losing all the merits of rigorous *ab initio* approach.

We use the empirical potential of Bazant and Kaxiras (EDIP)[43] in our MD simulations and for construction of the dynamical matrices for our large models. Due to the fact that this potential is **(i)** relatively new and **(ii)** has been fitted to simulate

only the bulk properties of amorphous silicon (and not surfaces — like we get when making a void in the network) it is also interesting to test its accuracy for calculations of vibrational properties of models for a-Si with and without voids, especially small ones — to verify that EDIP can reproduce (at least, qualitatively) the features we have obtained with more advanced *ab initio* method. As atoms of only one type — silicon — can be used in calculations with EDIP at this stage we are unable to use hydrogen atoms to terminate dangling bonds on void surface in our models.

4.2.1 Test of empirical potential

In this section we present some testing results for the DTW216 model for a-Si and 211 atom model with a void constructed from it by removing a single atom from the network together with its four nearest neighbors and then quenching the resulting structure to its equilibrium geometry with EDIP (as we have mentioned earlier, no H atoms are used here to terminate the dangling silicon bonds). The results of our VDOS and IPR calculations with EDIP are shown in Fig. 4.9. It's easy to notice that the model with void has a localized state in the low-energy gap which is general agreement with our previous results shown in Fig. 4.3. Of course, in this comparison we neglect all of the hydrogen motion in our "small void" a-Si:H model which is reasonable because hydrogen atoms do not "participate" in vibrational excitations of such low energy. It is clear that despite the fact that EDIP, comparing to the *ab initio* calculation, gives us different shape of the VDOS curve in the low-energy region, it is capable of reproducing the localized low-energy excitations. A "vibrational activity"

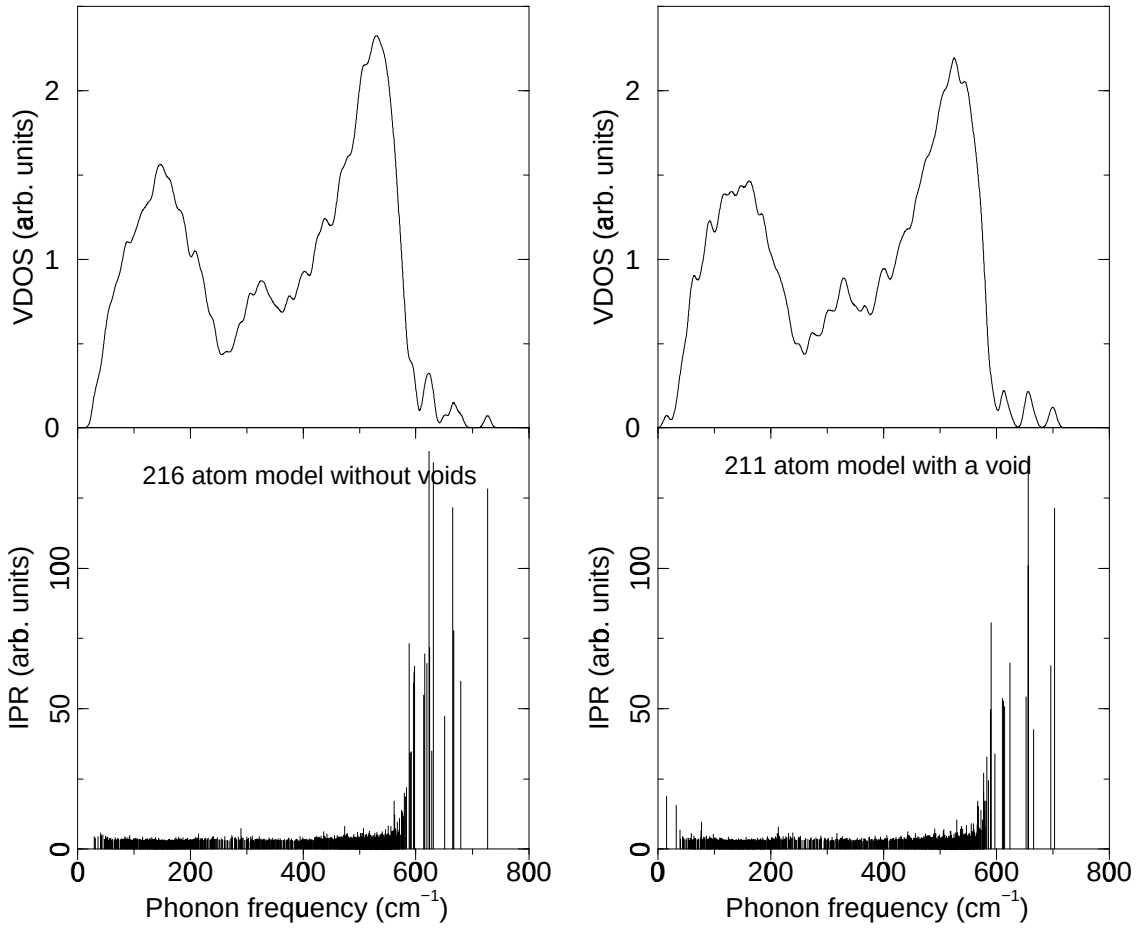

Figure 4.9: **VDOS and IPR for DTW216 and 211 atom model with a void made out of it calculated with EDIP.**

colormap for the localized low-energy mode we see in 211 atom model with void is shown in Fig. 4.10 has localization pattern quite similar to our previous result for "small void" model treated with *ab initio* technique (see Fig. 4.4).

4.2.2 Model construction and computational procedures

We employ the large Djordjevic, Thorpe and Wooten 4096 atom model[52] for a-Si as a base for building a family of models with voids. At first we optimize the geometry of the basic model by performing an MD quench with EDIP, which results only in minor network rearrangements. Due to less computationally demanding method for force calculations compared to the *ab initio* technique employed in the previous section we can use a more stringent force tolerance threshold for simulated quenching regime in our MD program: in all of its applications mentioned here we consider the models well relaxed when forces on all atoms are smaller than 0.01 eV/Å. The relaxed variant of DTW4096 is then used to produce all of the models with voids. To cut out a void we pick an arbitrary atom in the network and remove it as well as the consecutive spherical shells of its neighbors. We find that our results do not depend much on which atom we select for this procedure.

By applying this technique we have constructed three models with voids of different diameter: a 4091 atom model with a "small void" (only one atom and four of its nearest neighbors removed) — a void of approximately 5 Å in diameter, 4069 atom "medium void" model with 10 Å void and 4008 atom "large void" model with

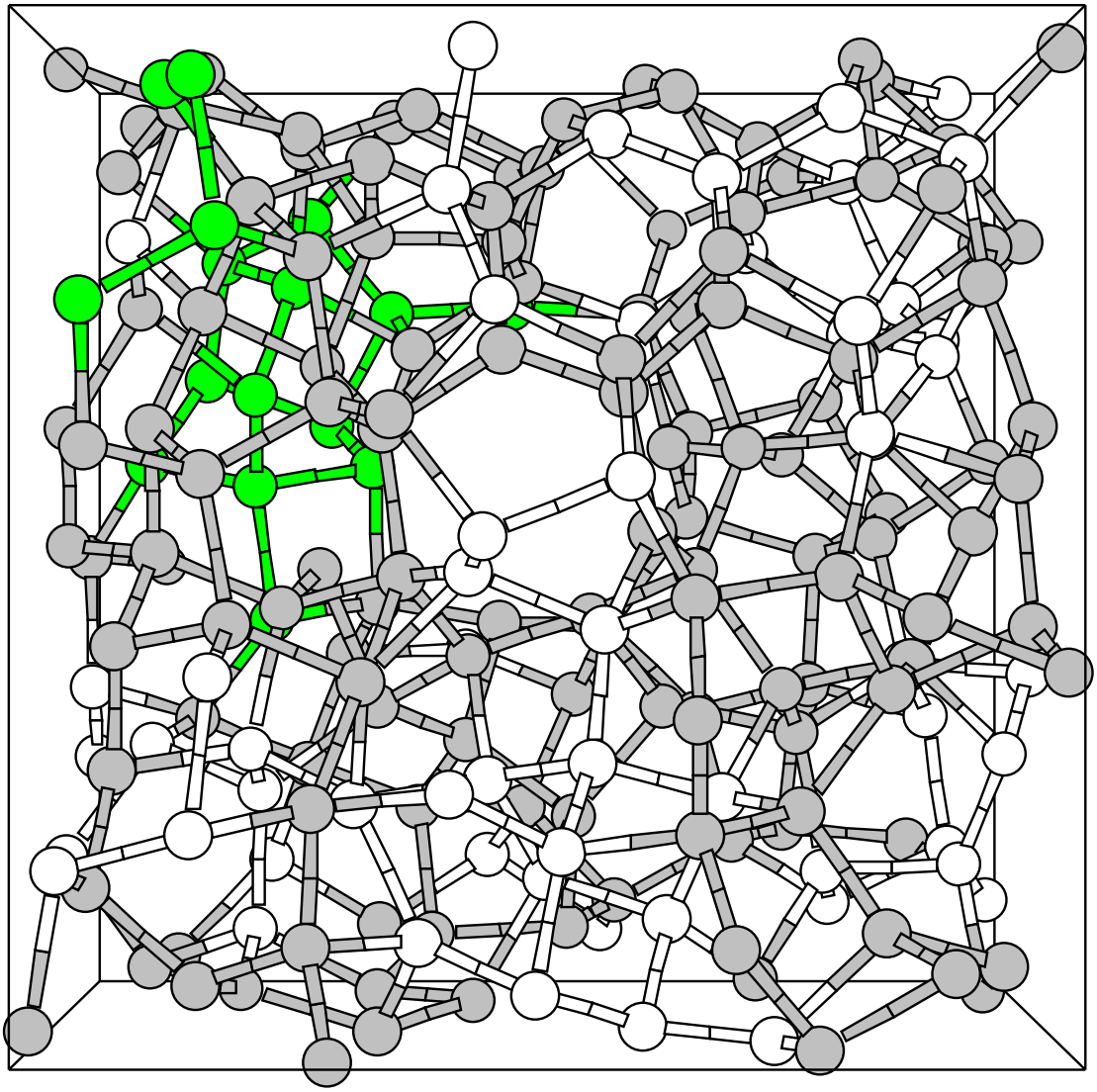

Figure 4.10: **Localized low-energy vibrational mode for 211 atom model with a void derived from DTW216 model. Color conventions the same as for Fig. 4.4.**

15 Å void. We refrain from building models with even larger voids to prevent possible interaction of a void with its own "ghost" images in the neighboring periodically translated supercells.

Every model with void is then quenched again to minimize the forces acting on atoms in the new configuration. After that we calculate the dynamical matrix for the model in exactly the same way as in the previous section with only difference that the interatomic forces for the dynamical matrix calculation are computed with EDIP and not the *ab initio* method. Of course, for a system of thousands atoms the dynamical matrix is very large, and this often causes problems in storing it on disk or in computer memory. Fortunately the dynamical matrix is also very sparse, because in most cases the displacement of a single atom generates significant forces only on its closest neighbors but not in the whole supercell. We extensively exploit this property of dynamical matrices in our calculations, discarding terms smaller than $10^{-4}\text{eV}\text{Å}^{-2}a.u.m.^{-1}$, which is a good compromise between accuracy and compactness of the output. Once the sparse dynamical matrix for the system is obtained we use a separate routine to exactly diagonalize the whole matrix and obtain all of the eigenvalues and eigenvectors. Again, for the same reasons as already mentioned above, we do not write out all of the eigenvectors (however, we do keep all their IPRs) but rather only those that exhibit properties we look for: **(i)** small energy/eigenvalue (less than 200 cm^{-1}) and **(ii)** relatively high IPR, showing that the vibrational mode we are dealing with is localized. All this data is then used to produce the VDOS and IPR graphs for the model and create the spatial localization/delocalization colormaps

for some of its low-energy vibrational modes.

Finally we need to make an important comment on the calculation of vibrational properties with EDIP. For all of our large models including the voidless DTW4096 we found that model's dynamical matrix has a few negative eigenvalues. The models with voids tend to have more negative eigenvalues than the model without voids, and the larger is the diameter of the void the more negative eigenvalues are found for the model's dynamical matrix. Regarding the voidless model, we believe that the negative eigenvalues found in its dynamical matrix are due to the fact that model's equilibrium structure (produced with the WWW method) creates an energy landscape which may be far from a real minimum for EDIP. In such situation computer discretization errors and the fact that dynamical matrix is calculated by finite differencing and not by taking analytical derivatives may lead to the emergence of negative eigenvalues in the matrix' spectrum. In models with voids, in addition to all these points, the restoring force on atoms located on void's boundary can become anharmonic which makes it close to zero in dynamical matrix calculation (harmonic approximation) which might also lead to negative matrix eigenvalues. It is important to remember that even the most advanced simulation methods like *ab initio* MD are *approximate* and in certain cases they may not produce realistic results. Of course, in an absolutely precise ideal calculation of vibrational spectrum of a system, states that have imaginary frequencies (negative eigenvalues) in the *approximate* dynamical matrix calculation mentioned above should all have very close to zero *positive* frequencies.

4.2.3 Vibrational properties and localization

The results of our calculations of the low-energy regions for VDOS and IPR for all the four models introduced above are shown in Fig. 4.11. We can see that the large models for a-Si (both, with and without voids) exhibit quite a complicated vibrational behavior, much more complex than that of smaller 216 atom based families of models, we have studied before[106, 107]. The most important difference here is that a-Si model *without voids* has two localized low-energy modes that are associated with strained regions of the network: we have checked bond lengths and bond angles for the atoms in these regions and found that these modes are localized on atoms with bond angles deviating from the perfect tetrahedral angle by more than 30 degrees. The vibrational activity colormaps for both modes are shown in Figures 4.12 and 4.13.

Consequently, now we have two types of *phonon traps* in our models with voids — the voids themselves and the strained regions of the network. Keeping this in mind we can attempt to introduce a rough classification of the localized low-energy modes according to the type of phonon trap they fall into. First, we can see a significant number of vibrational modes in our models with voids that generally show the same kind of localization properties that we have encountered in our previous calculation: they are exponentially localized with the center of localization positioned to the side of the void. We classify these excitations as void type modes. The colormaps with some examples of void type vibrational modes in all three of our models with voids

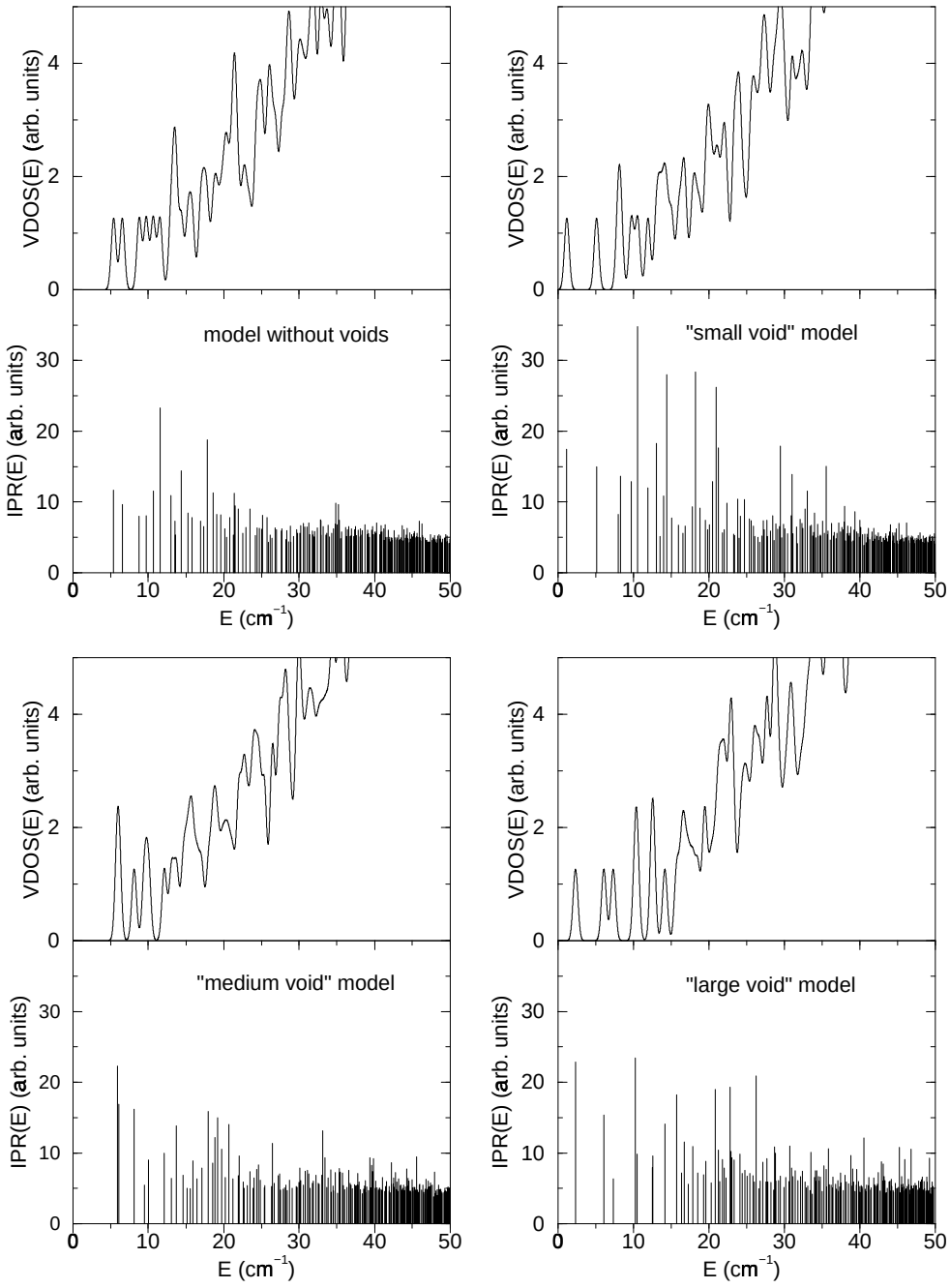

Figure 4.11: **Low-energy VDOS and IPR regions for 4096 atom DTW model without voids (upper left set of panels), 4091 atom "small void" model (upper right), 4069 atom "medium void" model (lower left) and 4008 atom "large void" model (lower right).** E **is phonon frequency.**

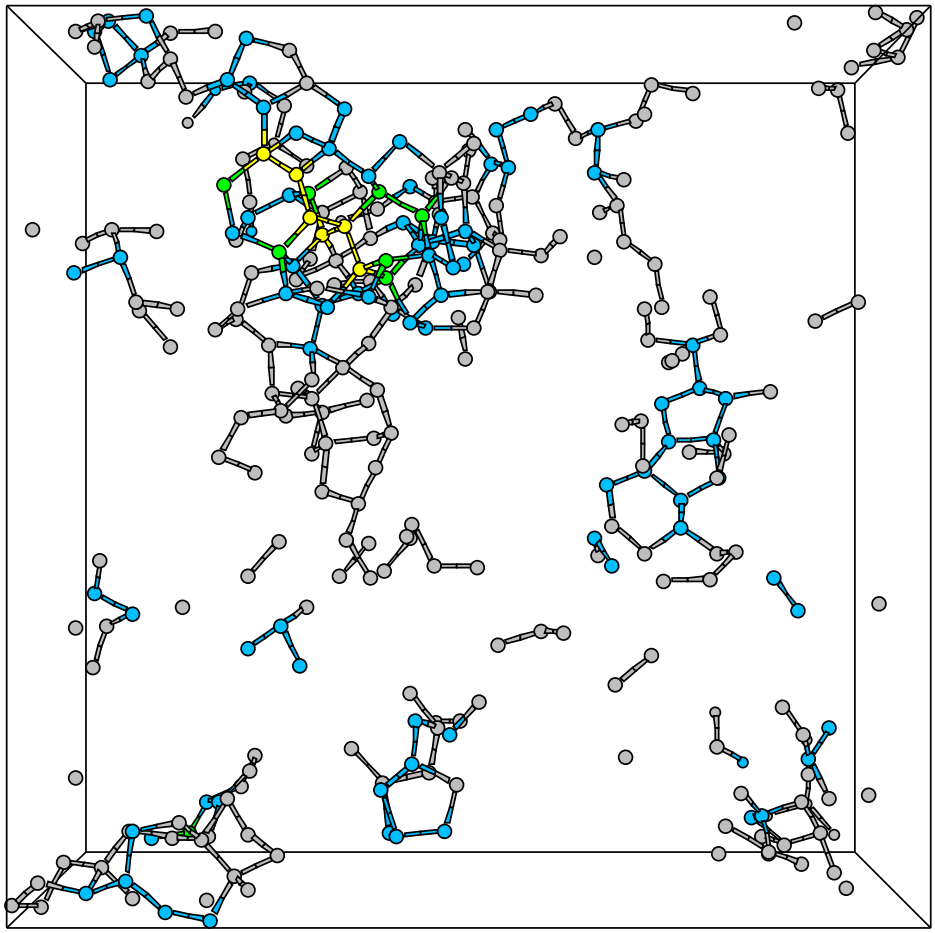

Figure 4.12: **Localized low-energy vibrational mode for DTW4096 model without voids. Phonon frequency is 12 cm^{-1}. IPR is 23.3. Atoms pictured in yellow account for more than 1 and up to 5% of total supercell excitation. Atoms, represented by green, blue and gray account for more than 0.5 and up to 1%, more than 0.1 and up to 0.5% and more than 0.05 and up to 0.1% of total supercell excitation accordingly. Atoms responsible for less than or equal to 0.05% of total supercell excitation are not shown except around the voids (atoms pictured in white).**

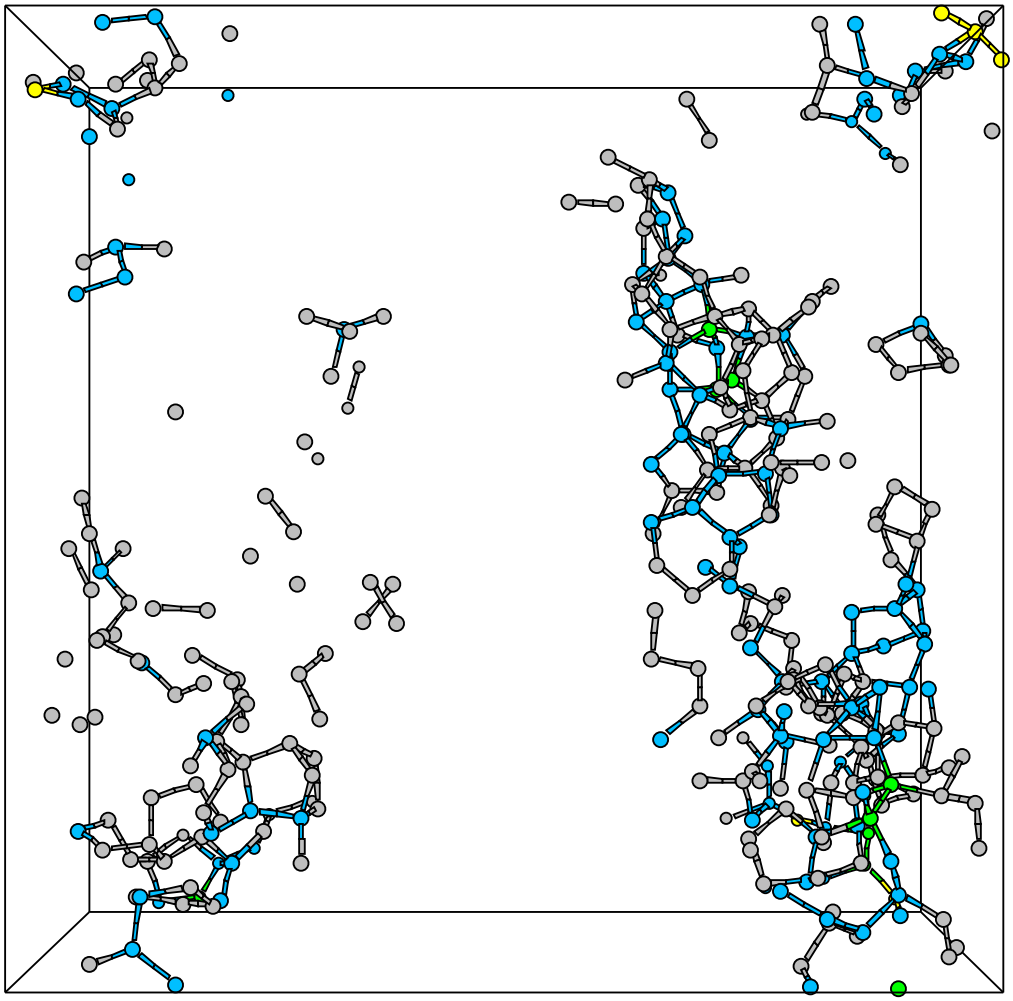

Figure 4.13: **Another localized low-energy vibrational mode for DTW4096 model without voids. Phonon frequency is 18 cm^{-1}. IPR is 18.8. Color conventions the same as for Fig. 4.12.**

are shown in Fig. 4.14, 4.15, 4.16 and 4.17. Secondly, the modes we might attribute to the *strained network region phonon trap* type in models with voids exhibit a different kind of behavior in comparison to the voidless model. These modes do not localize *exactly* on the strained regions in the supercell; instead they form a string extended between one of these strained regions and the void. The possible explanation of this behavior is that these modes can be regarded as a superposition of void type modes and the localized excitations in the model without voids. In our classification we call them mixed type modes. The examples of such modes in all three of our models with voids are presented in Fig. 4.18, 4.19, 4.20 and 4.21. We have to stress once again that the classification we propose is only approximate and is based mostly on the colormaps (i. e. pictures) we get for our models *not* on rigorous mathematical arguments. We must also add that all the low-energy modes, that appear localized in our *finite* models, will be pseudolocalized in an infinite sample[109].

We must admit that in our current investigation we were not able to find any simple connection between the size of the void and the energy and type of resulting localized modes. Our data shows that for different models with voids modes of different types dominate in the low-energy region. In the "small void" model a mode with the highest IPR at 10.58 cm^{-1} is of void type (see Fig. 4.14), but the succeeding three modes with high IPR at 14.43 (Fig. 4.18), 18.25 and 20.97 cm^{-1} are of strongly pronounced mixed type. In the "medium void" model, to the contrary, all three low-energy localized modes at 5.89 (Fig. 4.19), 6.12 and 8.13 cm^{-1} are of mixed type. The mode with strong void type behavior is also present but it is shifted to 17.97 cm^{-1} (see

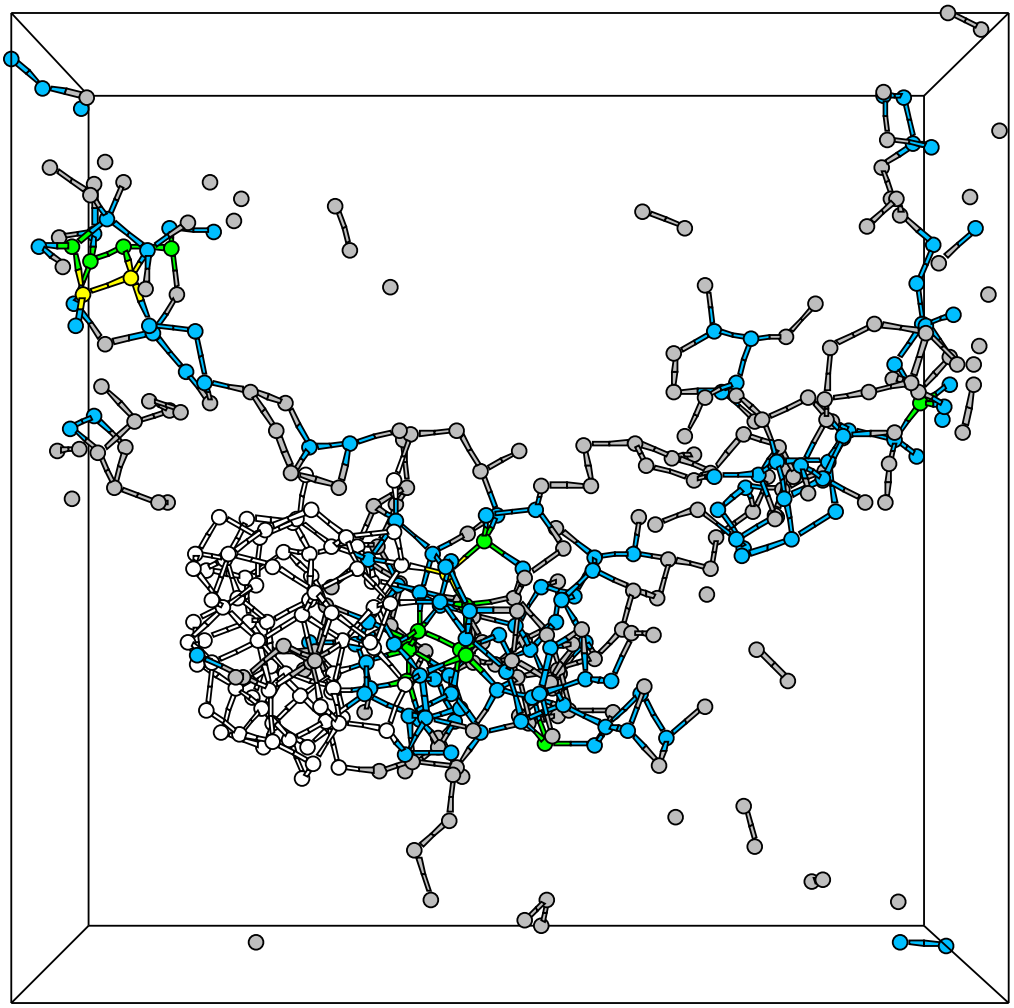

Figure 4.14: **Void-type mode for "small void" 4091 atom model. Phonon frequency is 10.58 cm^{-1}. IPR is 34.8. Color conventions the same as for Fig. 4.12.**

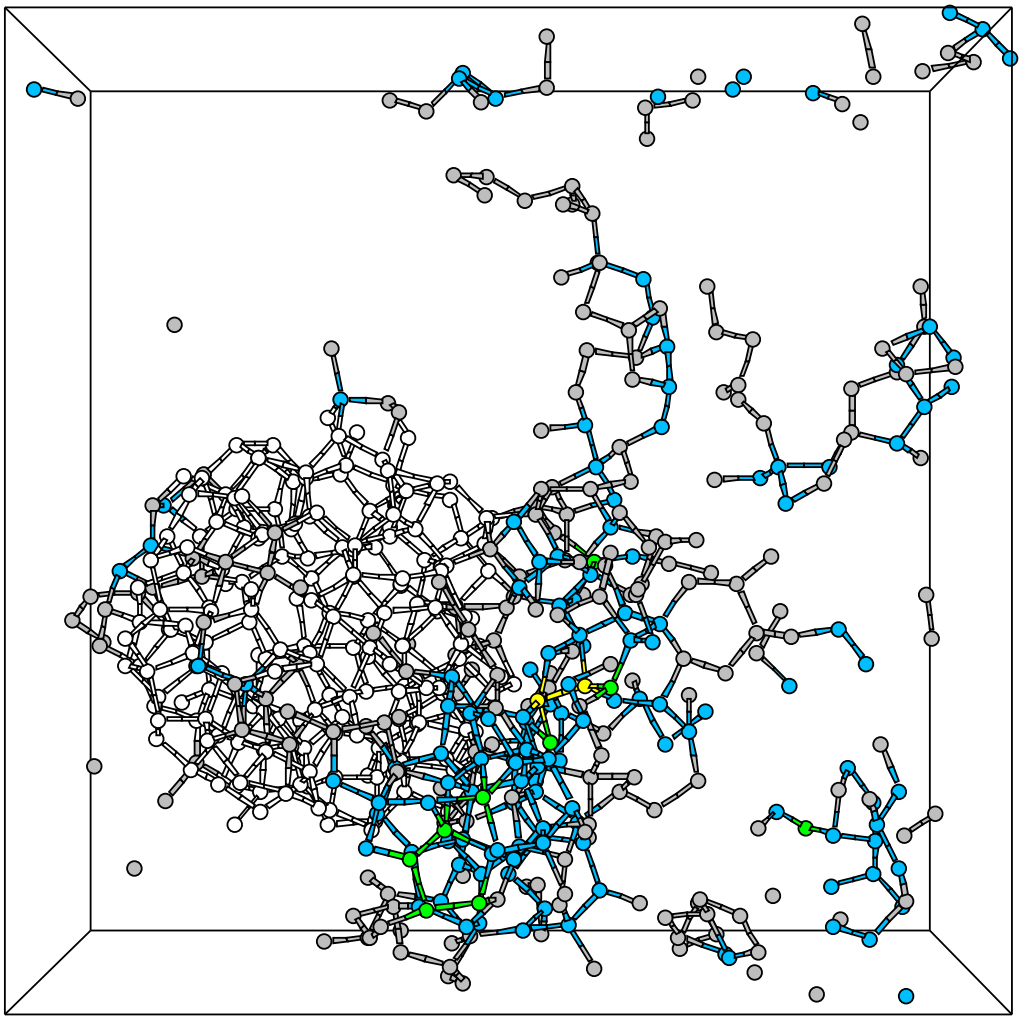

Figure 4.15: **Void-type mode for "medium void" 4069 atom model. Phonon frequency is 17.97 cm^{-1}. IPR is 15.9. Color conventions the same as for Fig. 4.12.**

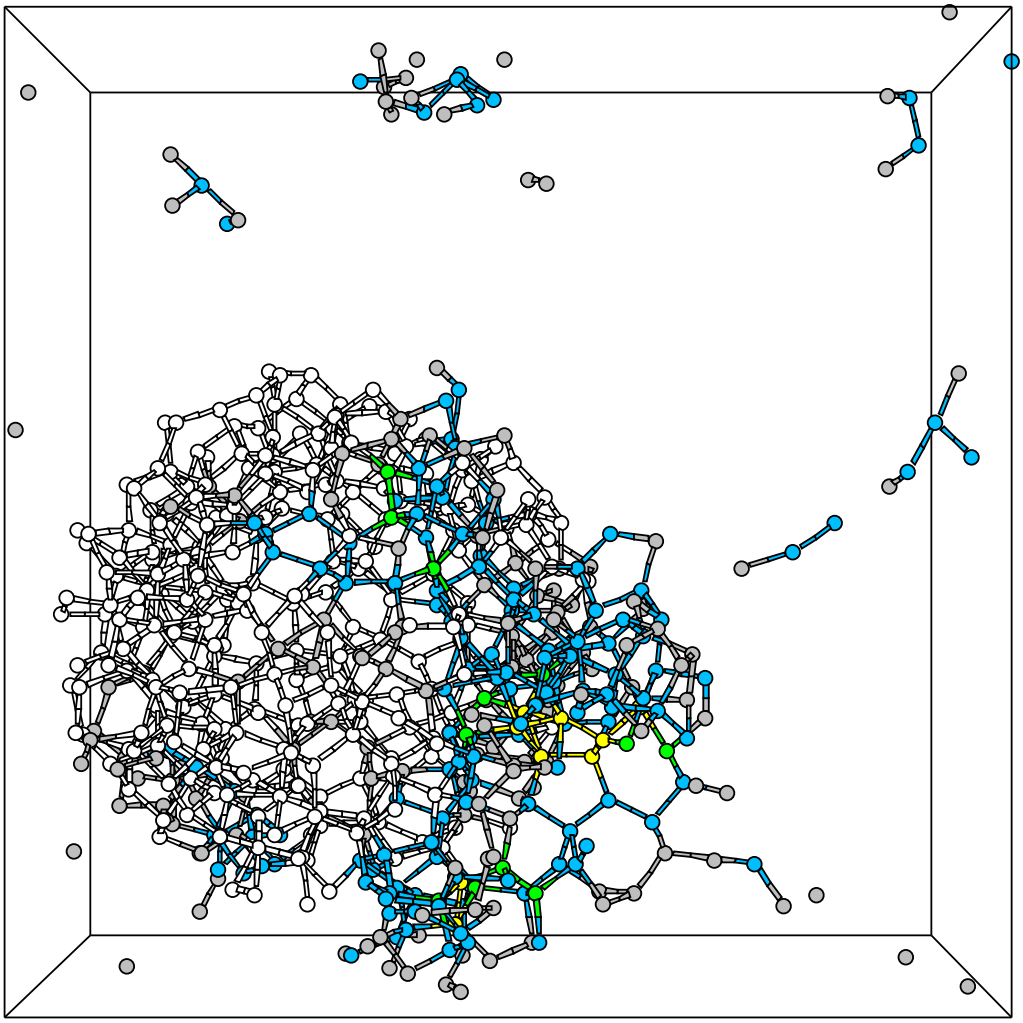

Figure 4.16: **Void-type mode for "large void" 4008 atom model. Phonon frequency is 2.34 cm^{-1}. IPR is 22.9. Color conventions the same as for Fig. 4.12.**

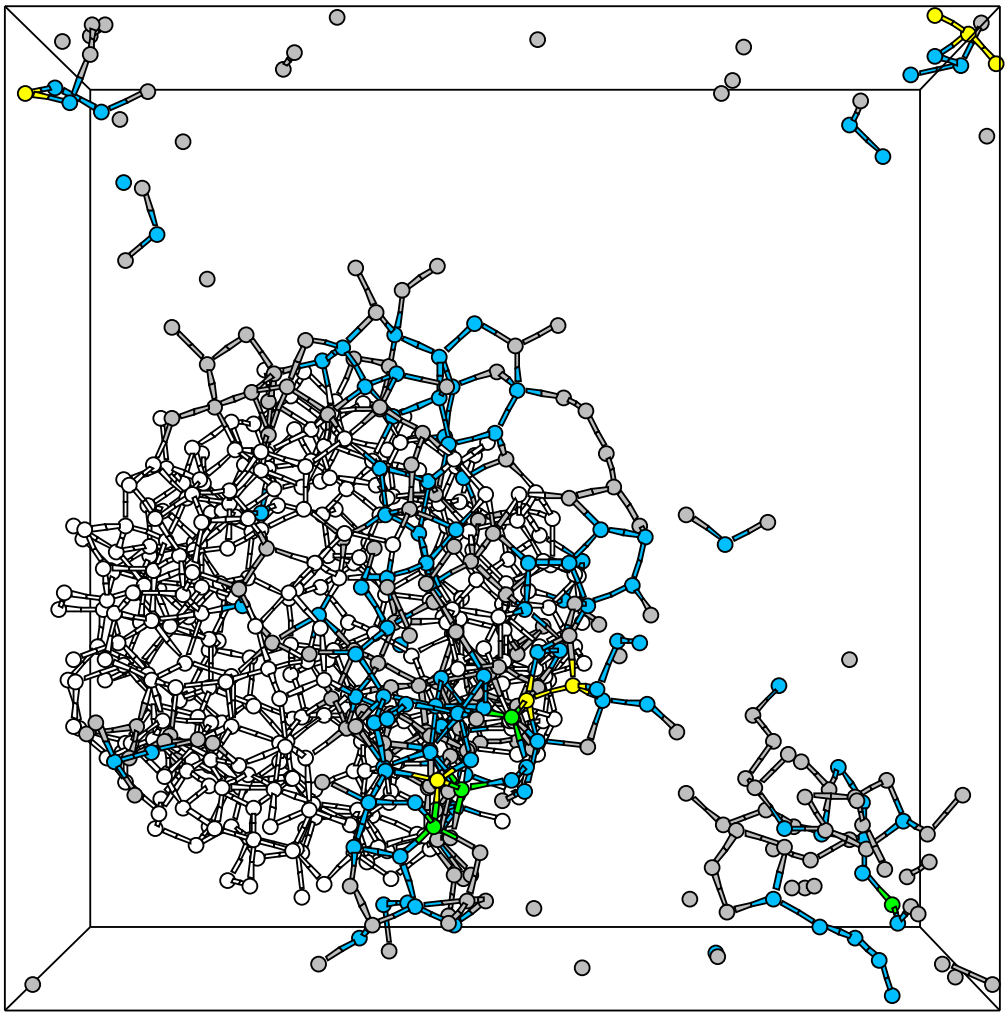

Figure 4.17: **Another void-type mode for "large void" 4008 atom model. Phonon frequency is 6.1 cm^{-1}. IPR is 15.4. Color conventions the same as for Fig. 4.12.**

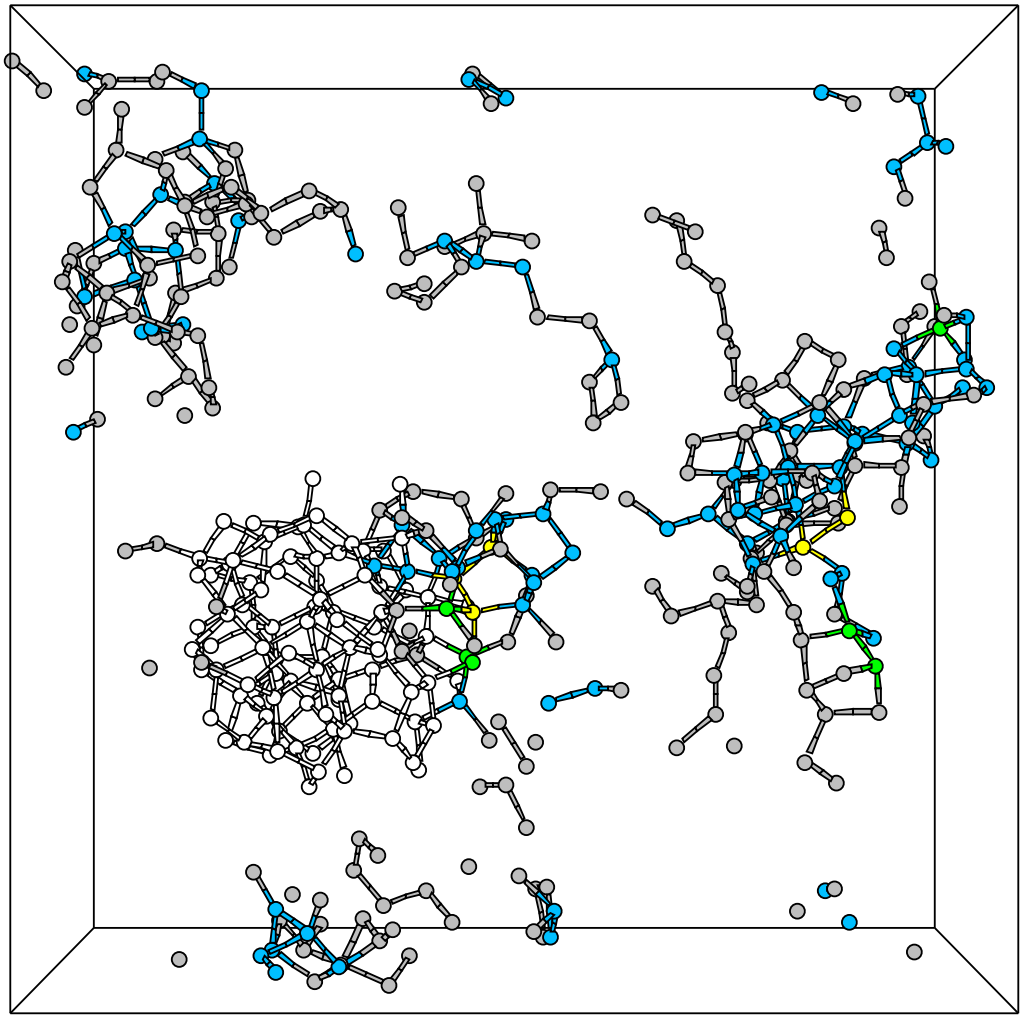

Figure 4.18: **Mixed-type mode for "small void" 4091 atom model. Phonon frequency is 14.43 cm^{-1}. IPR is 30. Color conventions the same as for Fig. 4.12.**

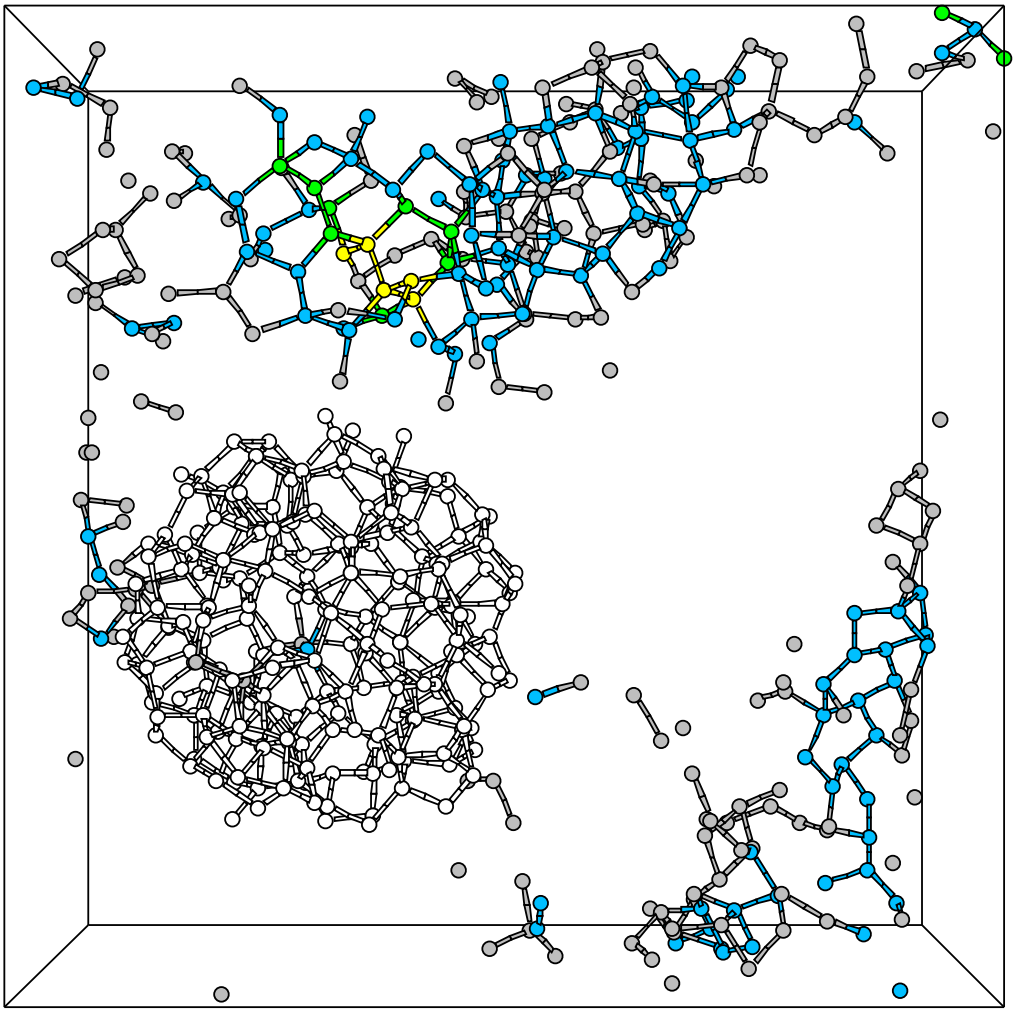

Figure 4.19: **Mixed-type mode for "medium void" 4069 atom model. Phonon frequency is 5.89 cm^{-1}. IPR is 22.3. Color conventions the same as for Fig. 4.12.**

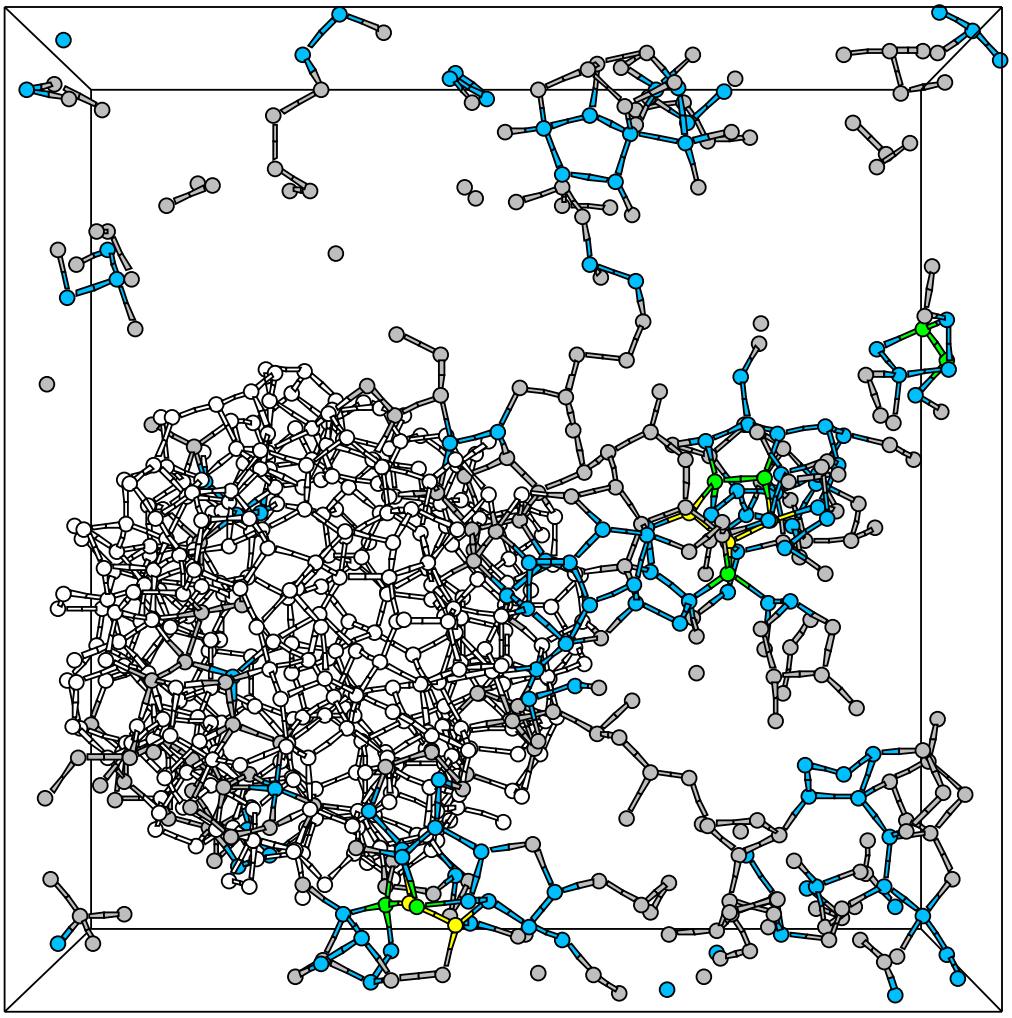

Figure 4.20: **Mixed-type mode for "large void" 4008 atom model. Phonon frequency is 15.8 cm^{-1}. IPR is 18.2. Color conventions the same as for Fig. 4.12.**

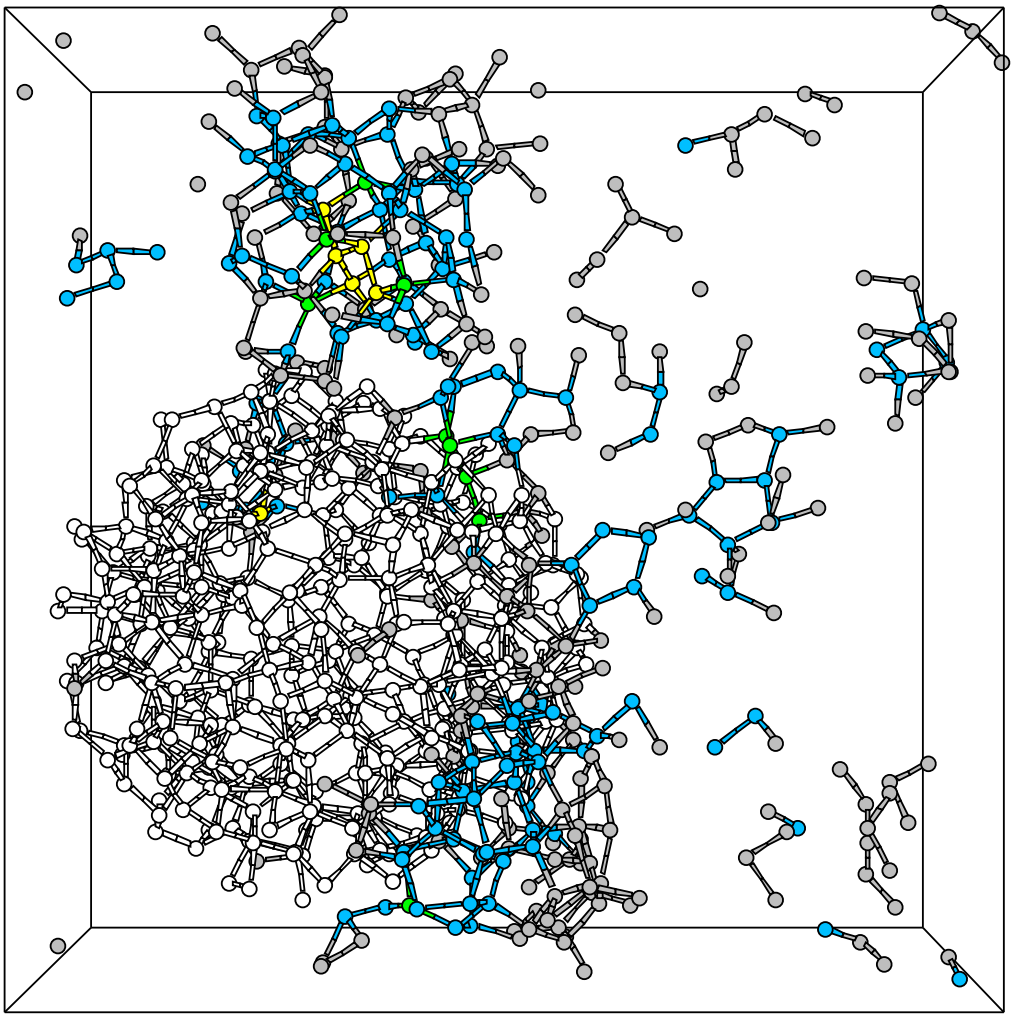

Figure 4.21: **Another mixed-type mode for "large void" 4008 atom model. Phonon frequency is 20.9 cm^{-1}. IPR is 19. Color conventions the same as for Fig. 4.12.**

Fig. 4.15). Finally in the "large void" model modes at 2.34 (Fig. 4.16) and 6.10 cm^{-1} (Fig. 4.17) are of void type and all the others, including a strongly localized mode at 10.28 cm^{-1}, exhibit mixed type behavior. We *speculate* that the network strain and geometrical peculiarities of any given model play a more important role in shaping the energy and type distribution of its localized vibrational modes than the actual size of the void — at least for the models with voids of comparable sizes, as we have here.

4.2.4 Specific heat

It is relatively easy to obtain specific heat $C(T)$ dependence for the model if the VDOS information for it is available[110]:

$$C(T) = 3R \int_0^{E_{max}} \left(\frac{E}{k_B T}\right)^2 \frac{e^{E/k_B T}}{\left(e^{E/k_B T} - 1\right)^2} g(E)\, dE,$$

where E is phonon frequency and VDOS $g(E)$ is normalized to unity. Nevertheless one thing should be treated with caution: the model VDOS one usually has is relevant for a system of *finite* size (i.e. our supercell). Vibrational excitations with wavelengths longer than the size of the supercell cannot be excited in this model and are consequently missing in its VDOS data. In order to receive the precise values for $C(T)$ one should correct VDOS for the *finite* size of the system. In our case it is done in the following fashion: all the delocalized (acoustic) vibrational modes of energy less than 20 cm^{-1} are cut out and substituted by a weak parabolic tail αE^2 in the routine to compute the VDOS. Parameter α can be obtained from a calculation of

the elastic constants of the model[111] but in this investigation we use a more simple approach, fitting α to provide a smooth transition between the low-energy parabolic tail and the rest of VDOS.

The overall temperature dependence for specific heat for all of our models is in good agreement with Dulong and Petit's law at high temperatures and Debye's law at low temperatures; our calculation also produces approximately the correct Debye temperature for a-Si. For the room temperature (300K) we receive practically the same value for specific heat for all of our models: 19.7 $JK^{-1}mol^{-1}$.

In the left panel of Fig. 4.22 the $C(T)/T^3$ low-temperature dependence for our models is presented. The most striking feature in this graph is the presence of sharp peaks at $T < 3K$ in the curves for the models *containing voids*. The model without voids *does not* have this peak, although it does demonstrate the presence of the well known excess specific heat bulge or "boson peak", the position and height of which are in qualitative agreement with experiment[112] as well as with recent computational results of Feldman, Allen and Bickham[109]. All of our models with voids also have these excess specific heat bulges. We were not able to find any experimental data for specific heat measurements in a-Si at temperatures below $2K$, but in order to make some general comparison to experiment for these new low-temperature features we obtain (which should be generic for *any* disordered system containing voids), we provide the experimental curve for vitreous silica[13] in our graph.

Unlike the previous void size vs. energy situation, we can find a clear connection between the presence of low-energy localized modes in vibrational spectrum of the

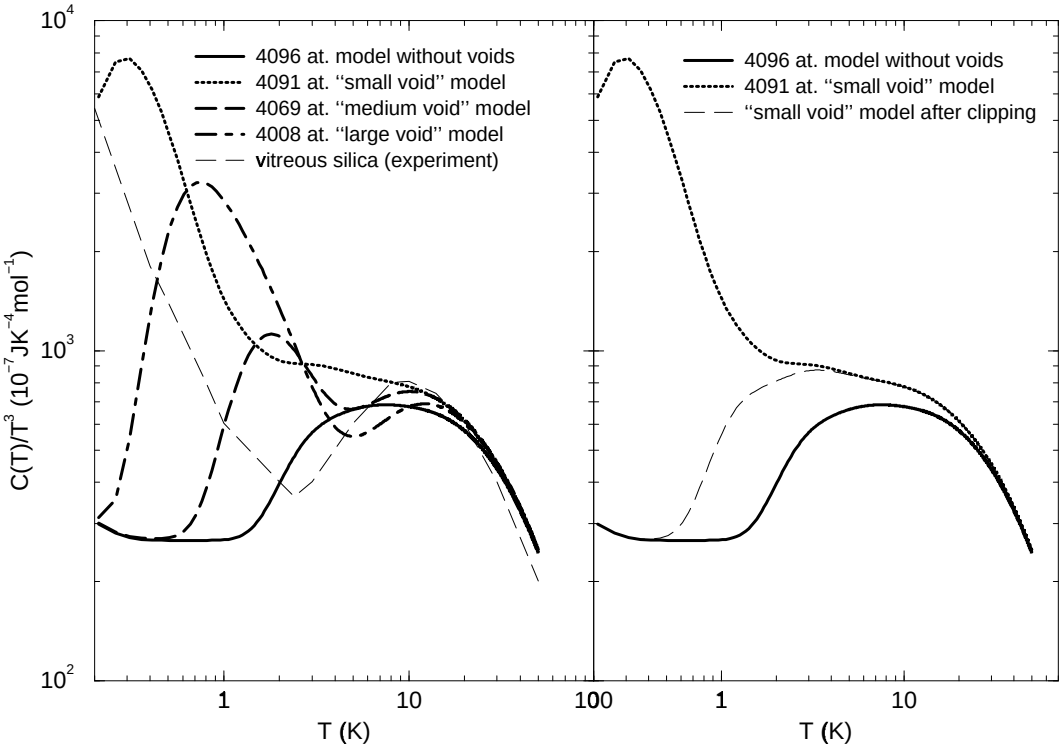

Figure 4.22: **Left panel: the low-temperature $C(T)/T^3$ dependence for the DTW4096 model and models with voids derived from it. The experimental curve for vitreous silica is taken from Ref. [13]. Right panel: the curves for 4091 atom "small void" model before and after clipping of the lowest energy localized mode eigenvalue. Curve for the model without voids is also shown for reference.**

model and the height (or even absence) of the low-temperature peak in its $C(T)/T^3$ graph. For the "small void" model we have a localized mode at 1.19 cm^{-1} (here and below, see Fig. 4.11) — the lowest energy at which we can see localized excitations in all our models — and the highest peak in $C(T)/T^3$ dependence. The "large void" model has its lowest energy localized excitation at 2.34 cm^{-1} and the peak of smaller height comparing to the previous model. The "medium void" model has two localized states but only at approximately 6 cm^{-1} and peak that is even less pronounced than in case of the first two models. Finally the model without voids has no localized states with energy lower than 11 cm^{-1} and *no low-temperature peak whatsoever.*

In order to investigate this connection in more detail we have performed a simple numerical experiment, which results are shown in the right panel of Fig. 4.22. We have clipped the eigenvalue at $1.19cm^{-1}$ from the eigenvalue set for the "small void" model and recalculated its VDOS and $C(T)$ receiving no low-temperature peak in $C(T)/T^3$ graph, much like in the situation with the model without voids. In our opinion these results provide enough evidence to attribute the existence of low-temperature ($T < 3K$) peak in $C(T)/T^3$ dependence for the model to the presence of localized low-energy ($E \sim 1 - 6\ cm^{-1}$) vibrational excitations — in our case produced by voids — in its spectrum.

We must note that the localized vibrational excitations we see, although having rather low energies, are *not* tunneling states, that are nonharmonic by nature and can not be obtained in harmonic approximation calculation. We do not claim that the whole tunneling states theory is incorrect, we rather propose an alternative

mechanism that explains the same experimental data. It seems that *any* mechanism that creates additional density of vibrational states (be this tunneling states or low-energy localized "void" vibrations in porous materials) at very low energies will produce the same effect on low-temperature specific heat behavior. In order to find out which mechanism of the two mentioned above *actually works* in real material, an experimental investigation of low-temperature thermal properties and *simultaneously* geometrical quality (i.e. presence of defects, voids, strained regions) of this material should be carried out. The works of X. Liu *et al.*[105] or Coeck and Laermans[113] for amorphous silicon can be regarded as the closest examples here.

4.2.5 Conclusions

We have studied vibrational and thermodynamical properties of 4096 atom DTW model for amorphous silicon and the family of models with voids based on it, employing Bazant-Kaxiras environment-dependent interatomic potential and empirical MD technique. We have found that the models with voids possess a complex spectrum of localized low-energy excitations that can be *roughly* divided into two groups — void and mixed type modes — according to their localization patterns. Our calculations show that there is no simple connection between the size of the void and the energy and type of its localized modes. It is most probable that not only the size of the void but also its local geometrical environment as well as strain distribution in the neighboring regions of the network play a paramount role in shaping the low-energy vibrational spectrum of the system. We have constructed specific heat $C(T)$ plots

for our models, that appear to be in good agreement with experiment. We have also plotted out our models' $C(T)/T^3$ dependencies for the low-temperature region, which seem to be in adequate agreement with experimental and other computational results for $T > 3K$ (the excess specific heat bulge) and predict new interesting features, undoubtedly connected with vibrational properties of voids present in the system, at lower temperatures. We must stress that our results are correct for model materials with a *uniform* distribution of voids of *one and the same size*, which is of course impossible to produce in real material. Nevertheless, employing our model data we can predict that in real material the localized low-energy vibrational states, connected to voids of different sizes, will fill out a band which will alter the parabolic VDOS tail properties at small energies and consequently manifest itself by changing the specific heat $C(T)/T^3$ dependence.

Chapter 5

Realistic models of paracrystalline silicon

Work presented in this chapter has been done in collaboration with P. M. Voyles, N. Mousseau and G. T. Barkema. Dr. Barkema has provided us the initial code for construction of CRN models of a-Si with the modified WWW method and the code for crystalline cluster analysis. The former code has been then modified by us to allow construction of paracrystalline silicon models. The experimental electron microscopy data as well as all the simulated normalized variance curves discussed in subsection 5.2.3 have been kindly provided by Dr. Voyles.

Recent fluctuation electron microscopy (FEM) experiments have shown signatures of medium range order (MRO) in as-deposited amorphous semiconductor thin films [10, 114]. These results have been interpreted as indicating the presence in the amorphous films of small (< 30 Å) topologically crystalline grains, which are distorted by strain and embedded in a disordered matrix. Such material is called

paracrystalline [114]. It has the structure factor of amorphous material, but nonetheless has significant MRO. It is difficult to verify this interpretation with other experimental techniques, so computer modeling has been used to study the structure of these complex systems and the traces of MRO in them. In this chapter we present the first large scale atomistic models of paracrystalline Si which are electronically realistic[115]. Simulated FEM on these models reproduces the experimental measurements more accurately than any other model tested.

Only a model that agrees with a whole set of experiments, including structural, optical, and vibrational characterizations, can reliably describe a real material. One of the most common methods for constructing CRN models of *a*-Si, the molecular dynamics (MD) "quench from the melt" procedure, does not meet this criterion, as it produces models with relatively poor electronic properties (see Chapter 2 for detailed discussion). The best large (1000 atoms and more) models created with this technique[44] tend to have at a least 3–4% concentration of coordination defects, as well as significant residual network strain which manifests itself as an increased width of the bond-angle distribution $\Delta\theta$ compared to the experimental value[3]. The electronic states associated with these structural defects fill out the optical gap of the model material[66, 67], practically turning the model from a semiconductor into a poor metal [116]. This is clearly unphysical. However, these models can have a reasonable phonon spectrum and pair-correlation function, which can be misleading, since the results of simulations for these models involving their electronic properties can not be fully trusted.

The only family of models of paracrystalline Si previously available was a set of models developed by Keblinski *et al.* [114, 117] using empirical MD with the Stillinger-Weber potential [40] and a "quench from the melt" procedure in which *c*-Si grains are introduced into the melt and not allowed to dissolve [118]. Recently, we have extensively studied the properties of these models [117] and found that, like CRN models produced in a similar way, these paracrystalline models have an unphysically high density of defect electron states in the bandgap region — see Fig. 5.1. They do, however, better reproduce the degree of MRO present in experimentally grown *a*-Si films [114] than a variety of CRN models. Now our challenge is therefore to create a model that would comply with all the experiments simultaneously. In order to do that we have employed the bond-switching algorithm of Wooten, Winer and Weaire [51], modified by Barkema and Mousseau [55], which produces the best current CRN models. The original WWW method has been used by Nomura *et al.*[119] to study electronic properties of nanocrystallites in *a*-Si but for unknown reasons produced poor results.

5.1 Model preparation

We generally follow the procedure of Barkema and Mousseau outlined in section 3.1 to create paracrystalline models, but before randomly seeding the supercell with atoms, we position inside it one or more crystalline grains, randomly oriented

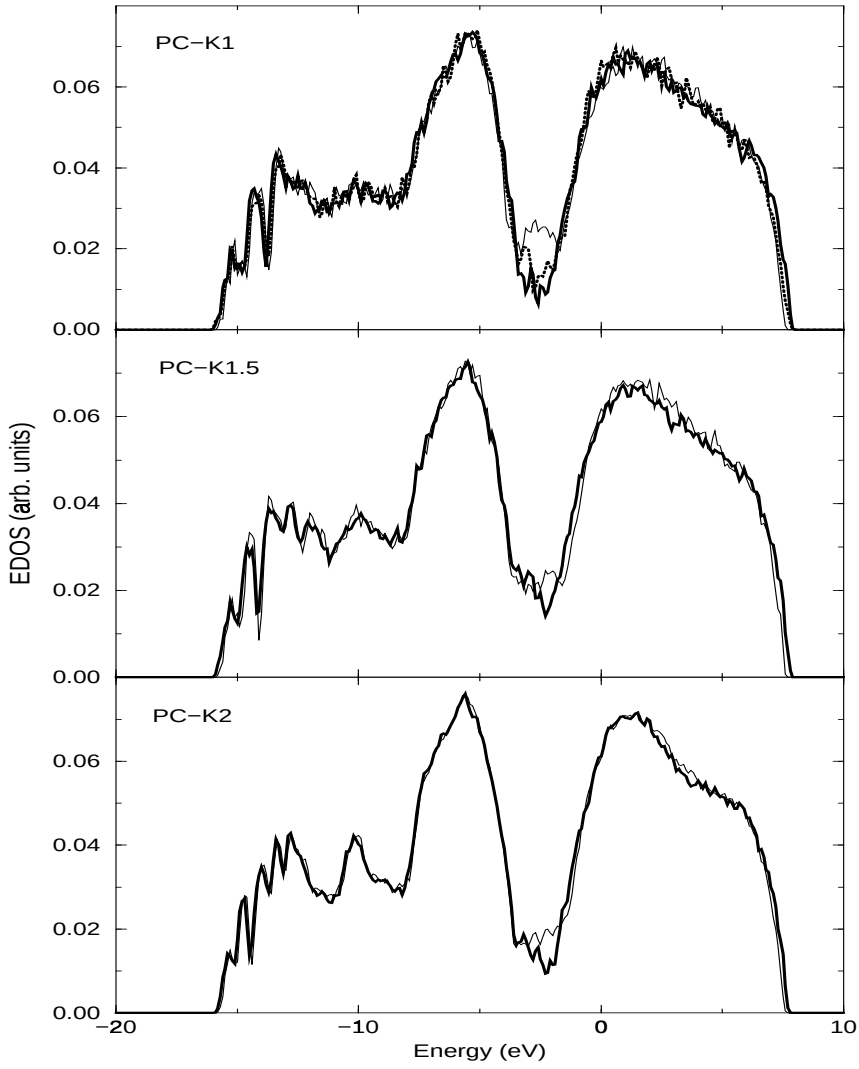

Figure 5.1: **The EDOS for paracrystalline and CRN models of Keblinski** *et al.* **Upper panel: 512 atom paracrystalline Si model PC-K1. Solid line: initial configuration, dashed line: after quench with FIREBALL, bold line: after anneal and quench with EDIP. Middle panel: 700 atom paracrystalline Si model PC-K1.5. Solid line: initial configuration, bold line: after anneal and quench with EDIP. Lower panel: 1000 atom paracrystalline Si model PC-K2 (solid line) and 512 atom CRN model CRN-K1 (long-dashed line).**

with respect to one another. The grains are created by starting with a spherical section of crystalline Si and keeping only those atoms that have two and more nearest neighbors which also belong to the grain. For reasons described below we also require the grain to contain an even number of atoms that have three nearest neighbors.

When the grain is positioned inside the box, a nearest neighbor list is created for it and the 2- and 3-fold coordinated atoms on the surface are identified. After the grains are set in place the remaining volume is randomly seeded with "matrix" atoms, which are then connected into a perfectly 4-fold network. The grains are at this point disconnected from the disordered matrix and need to be incorporated into it in such a way that all the atoms have exactly four nearest neighbors. This is done in two steps. First, for any 2-fold grain atom the closest bonded pair of matrix atoms is found, the bond between the matrix atoms is broken, and two new bonds between each of the matrix atoms and the grain atom are formed. Second, for each 3-fold grain atom the closest additional 3-fold grain atom is found, then the bonded pair of matrix atoms closest to both 3-fold grain atoms is found, and the bond between these atoms is broken and two new 3-fold grain atom/matrix atom bonds are formed. This requires an even number of 3-fold grain atoms. This algorithm creates a number of unphysically long bonds, but these high-energy bonds are sure to be broken during the bond-switching transpositions.

After the perfectly 4-fold network containing both the crystalline grains and the matrix is constructed, it is subjected to bond-switching moves in order to minimize the system's energy. Unlike in the WWW method, we constrain the bond switching in

order to preserve the crystalline topology of the grains during energy minimization. Bonds between grain atoms are not allowed to break; only bonds between a grain atom and a matrix atom or between two matrix atoms can be broken. An additional constraint is imposed on the positions of the grain atoms: during the initial phase of the relaxation, while strain in the system is relatively high, the coordinates of the grain atoms are fixed. When the energy of the system with fixed grain atoms reaches its minimum, the grain atoms are allowed to move and the energy is minimized again.

5.2 Discussion of results

5.2.1 Structure and vibrational properties

Using the procedure described in the previous section we have constructed three models of paracrystalline silicon. The first 400-atom model, called px400, has one grain consisting of 44 atoms, positioned in the center of a 20 Å cubic box. This model has been created mostly for testing purposes. The second model, px1000, has 1000 atoms, of which 86 belong to a single grain placed in the center of a cubic box with a side of approximately 28 Å. The third 4000 atom model, px4000_4, has 4 crystalline grains of roughly the same size (100 atoms), randomly oriented with respect to one another and positioned at the vertices of a tetrahedron the center of which lies at the center of the 43 Å cubic supercell. The two smaller models are 100% 4-fold coordinated while the largest one has eight 5-fold and two 6-fold coordinated atoms. All the models have $\Delta\theta < 10.6°$, which is in excellent agreement with experiment.

Our 1000 atom paracrystalline model, px1000, is shown in Fig. 5.2 to provide a visual example of the topological structure of such models.

The radial-distribution function $g(R)$ for our largest model px4000_4 is presented in Fig. 5.3. The curve computed for a 4096 atom CRN model of Barkema and Mousseau [55], BM4096, and the experimental curve[3] are shown for comparison. The curves for the models look almost exactly the same and both seem to be in very good agreement with the experimental data.

The bond-angle θ and the dihedral-angle ϕ distributions for px4000_4 and BM4096 are presented in Fig. 5.4. The bond-angle distributions for both models look identical while the dihedral-angle distribution for the paracrystalline model has a pronounced peak at 60 degrees which is not present in the distribution for the CRN model. This feature is explained by the fact that the paracrystalline model has a larger share of atoms (mostly the ones belonging to the grains) whose local environment is very close to crystalline thus favoring $\phi = 60°$. We should point out that except for the FEM simulations (see below), the calculation of dihedral-angle distribution (or any other triplet or higher correlation function) provides the only non-topological way to distinguish between CRN and paracrystalline structures.

The vibrational density of states (VDOS) curves for px4000_4 and a 1000 atom CRN model for a-Si of Barkema and Mousseau, BM1000, are shown in Fig. 5.5. The results for two smaller paracrystalline models are not presented because their VDOS curves are practically identical to the one of the largest model. The curves for both models shown in the figure look very similar as well. The VDOS for all the

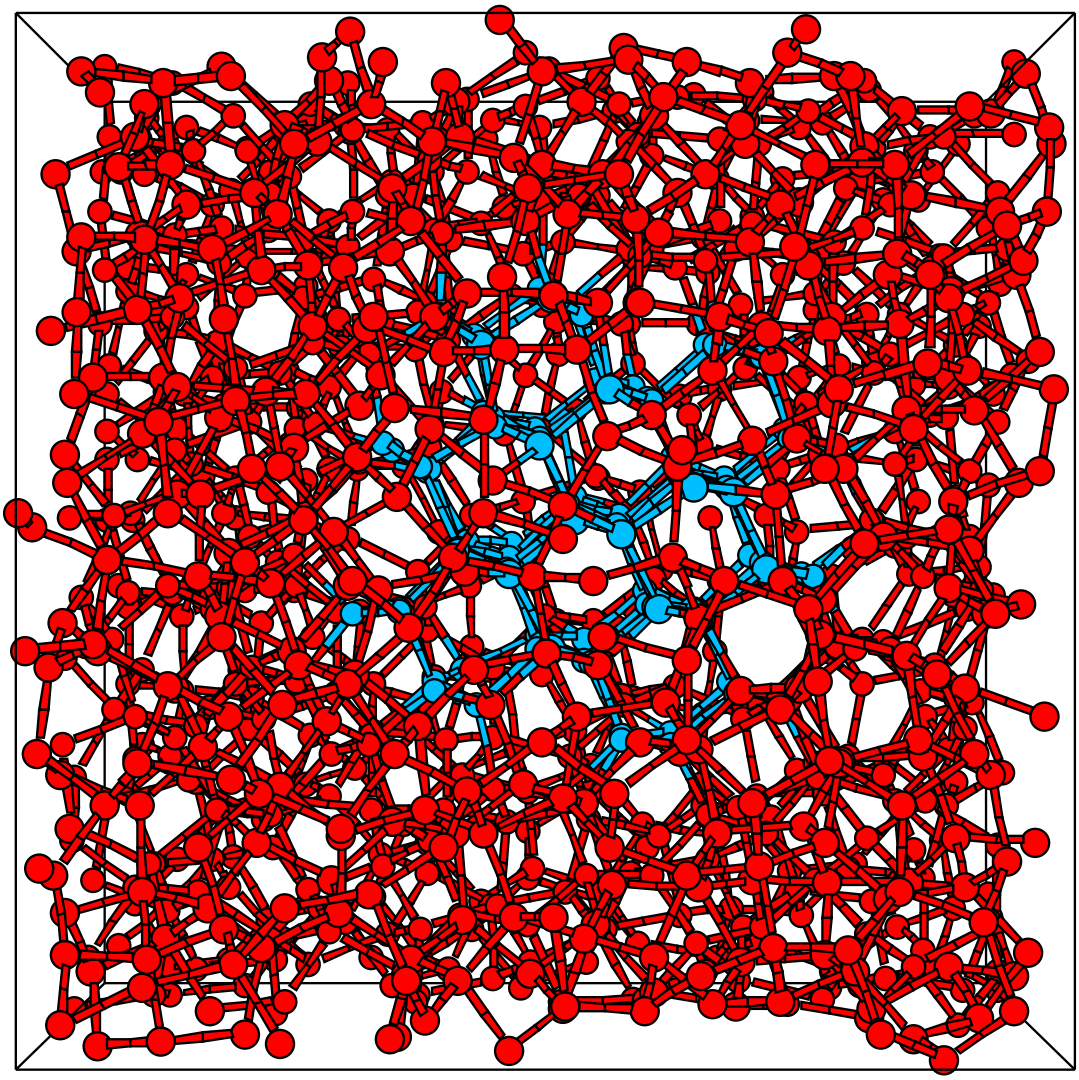

Figure 5.2: **The 1000 atom paracrystalline Si model, px1000, after simulated MD quench with the MSW potential. Atoms belonging to the grain are shown in blue, the disordered matrix atoms — in red.**

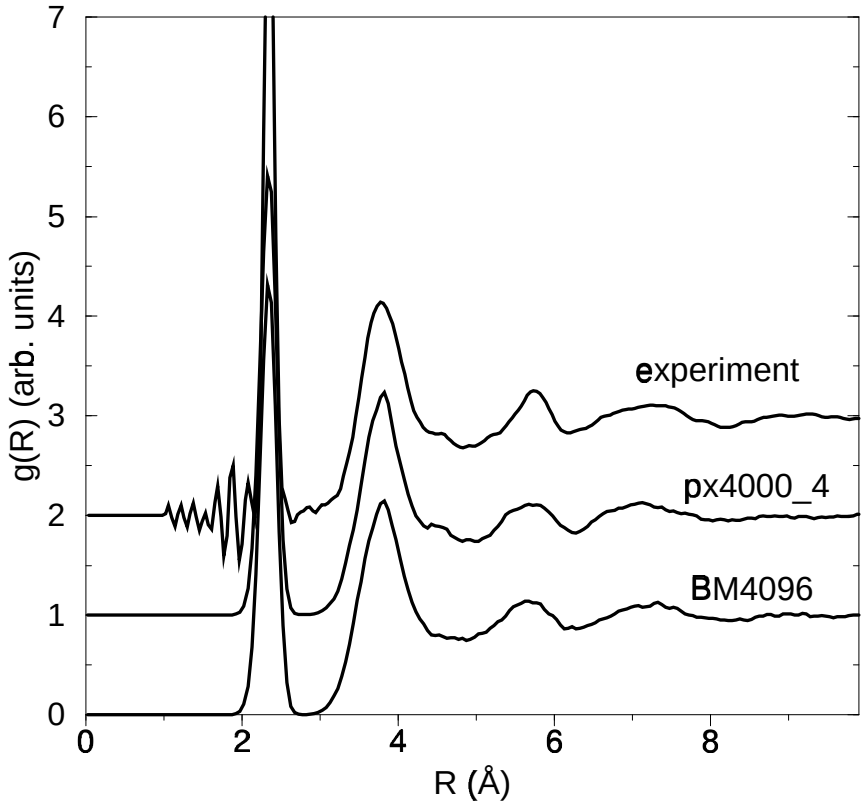

Figure 5.3: **Radial-distribution function $g(R)$ for 4000 atom paracrystalline model and 4096 atom CRN model. The experimental curve is taken from Ref. [3]. Note how the curve for px4000_4 model correctly reproduces the small peak at approx. 4.5Å present in the experimental data.**

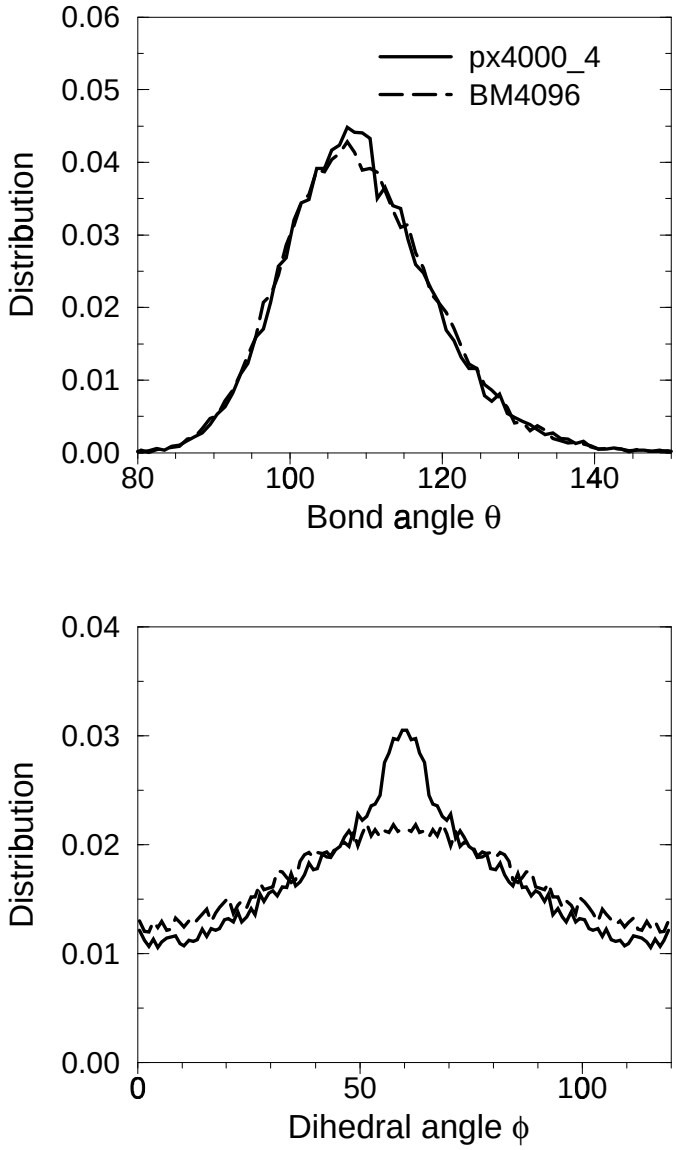

Figure 5.4: **Bond-angle (upper panel) and dihedral-angle (lower panel) distributions for 4000 atom paracrystalline and 4096 atom CRN models.**

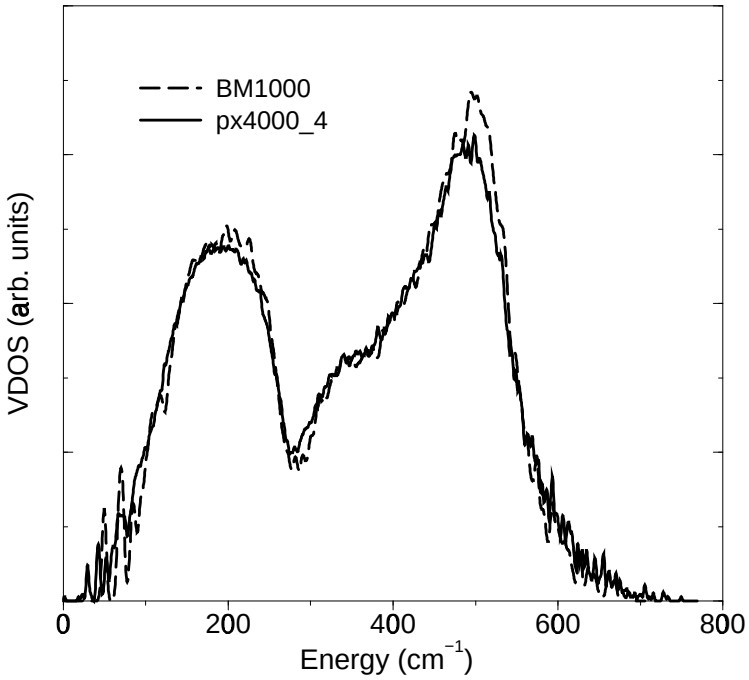

Figure 5.5: **The VDOS for 4000 atom paracrystalline and 1000 atom CRN models.**

models has been calculated by a direct diagonalization of their dynamical matrices computed with the modified Stillinger-Weber potential[48]. Prior to the dynamical matrix calculation the models were relaxed with the simulated MD quench employing the same potential.

5.2.2 Electronic properties

In the upper panel of Fig. 5.6, we present the bandgap region of the electronic density of states (EDOS) of px400, px1000, and BM1000. The total EDOS is shown in the inset; at this scale it is indistinguishable for all three models. The EDOS

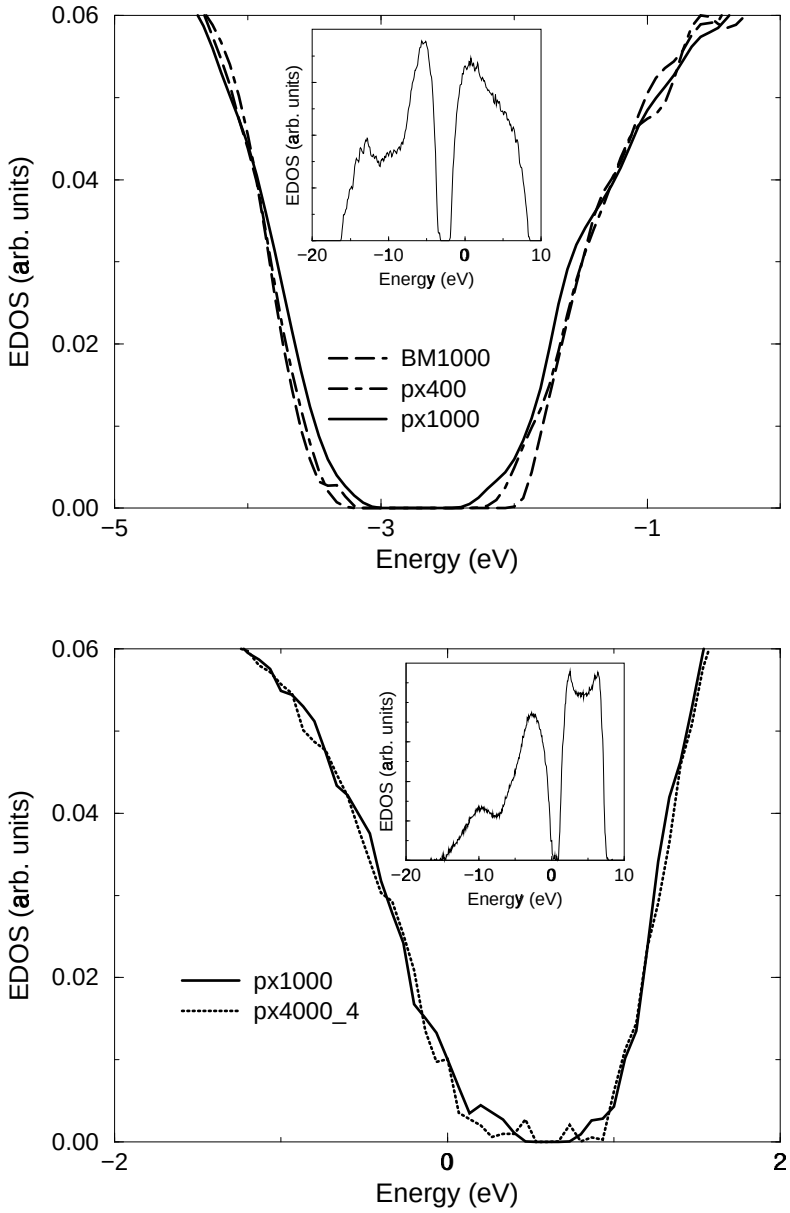

Figure 5.6: **The bandgap region of the EDOS calculated with local-basis** *ab initio* **method for 400 and 1000 atom models (upper panel) and with empirical tight-binding Hamiltonian for 1000 and 4000 atom models (lower panel). The total EDOS is shown on the panel inserts.**

for all these models has been calculated with the FIREBALL [23] local-basis *ab initio* code. In the lower panel of Fig. 5.6, the bandgap region for the EDOS of px4000_4 computed with empirical tight-binding Hamiltonian of Kwon *et al.* [33] is shown. The total EDOS for px4000_4 is presented in the inset to the lower panel. The EDOS bandgap region curve for px1000 calculated with the same method is also shown for reference — note how the empirical tight-binding calculation tends to underestimate the bandgap comparing to the more advanced *ab initio* method. We must point out that, of course, both methods produce bandgap widths that are quantitatively unrealistic (too narrow).

We have also studied the nature of the valence bandtail and bandgap states in our largest model, px4000_4. The IPR for all the states in the model is shown in Fig. 5.7. Focusing our attention on the bandtail and bandgap region of the graph (the energy interval between 0 and 1 eV) we can see that all of the states in this region are strongly localized compared to the states in the valence and conduction bands. In Fig. 5.8 we have plotted out the total charges (obtained as sums of squared components of an eigenvector for a given electronic state "belonging" to atoms of a particular group) for the matrix, grain and for so called "interface" atom groups. The interface atoms are identified as those having nearest neighbors of both — matrix and grain — groups. The matrix and grain groups of atoms used to create the figure have been contracted compared to our initial atomic groups: now an atom belonging to the matrix group can have nearest neighbors only from the matrix or interface groups, and a grain group atom — only from the grain or interface groups. As we can

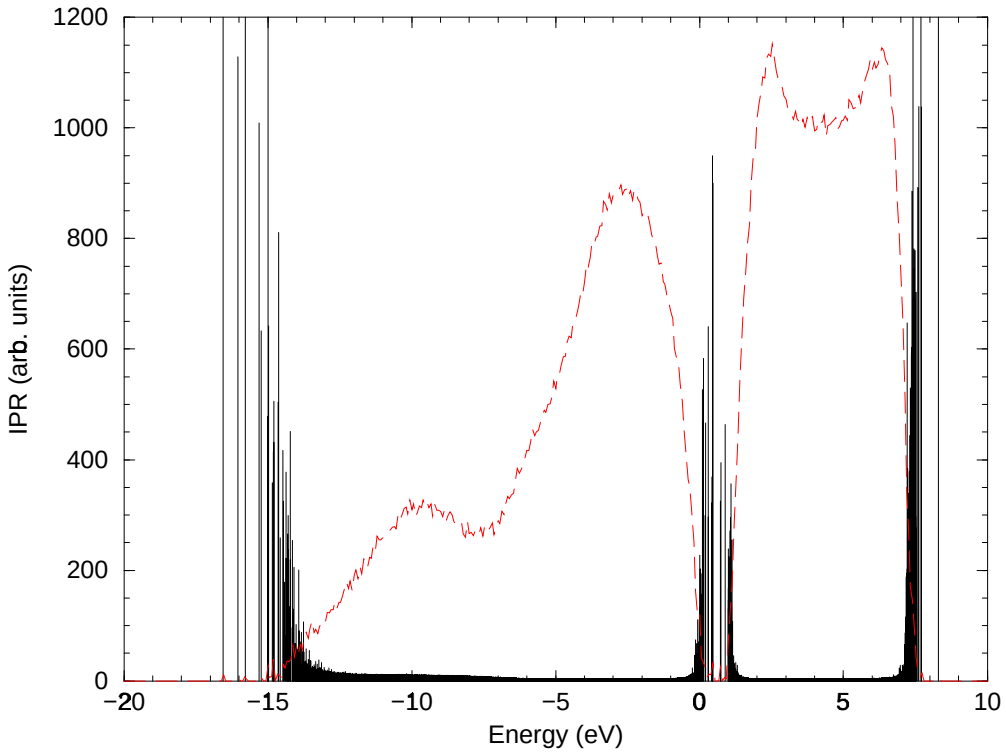

Figure 5.7: **The IPR for the electron states in px4000_4 model. The total EDOS curve for the model is also presented for reference (long-dashed red line).**

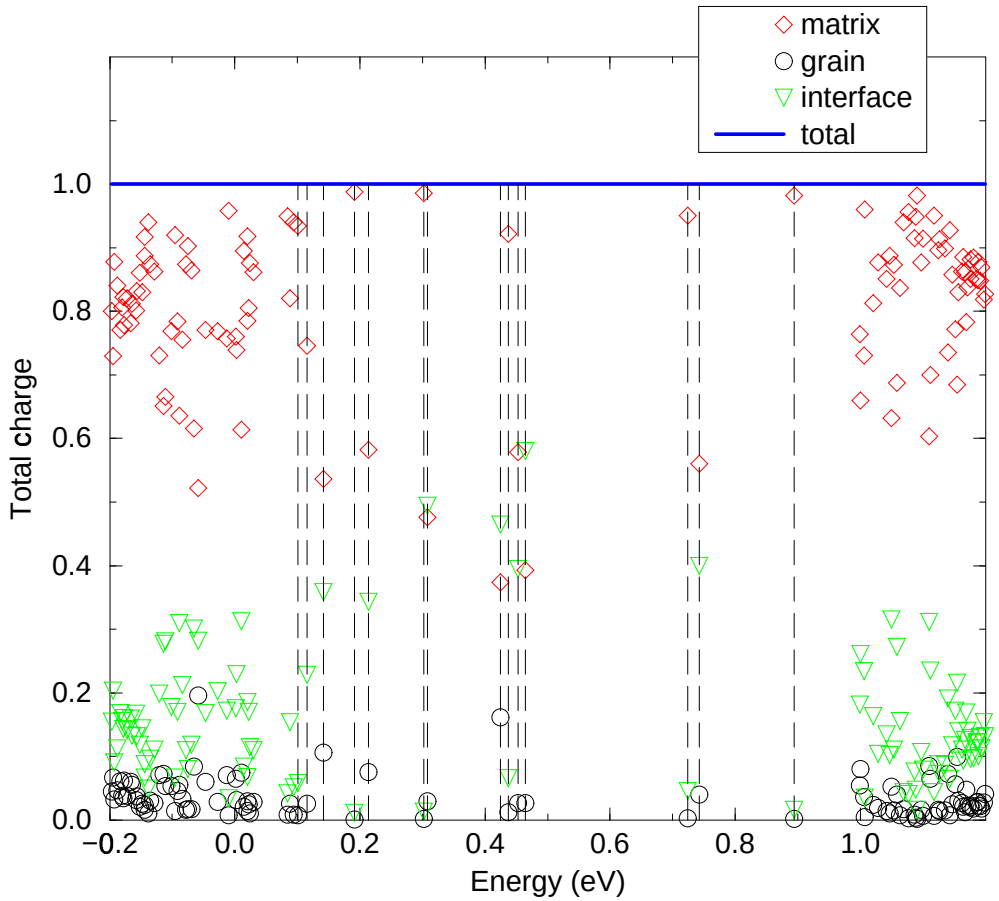

Figure 5.8: **The total charges for matrix, grain and interface groups of atoms in px4000_4 model. The total charge of the system for every electronic state is equal to unity (blue line). The most interesting bandgap states in 0–1 eV energy interval are marked with long-dashed black lines.**

see from Fig. 5.8, as we go across the bandgap from the valence to the conduction bandtail region, for some states the amount of charge localized on the interface atoms goes up — and consequently the amount of charge distributed among the matrix atoms goes down because the total charge for every state is 1 (all the eigenvectors are normalized to 1) — while for other states the amount of charge belonging to the matrix atoms becomes almost equal to the total charge of the supercell. Using our colormap technique we have examined spatial localization patterns for some states of both types (states marked with long-dashed black lines in Fig. 5.8) and found out that the states for which the matrix charge dominates localize on strained regions of the network in the disordered matrix, (such localization patters have also been observed in large CRN Si models[68]) while the states for which the interface charge dominates are localized on the grain boundaries, which obviously also contain some highly strained bonds. This leads us to believe that in paracrystalline Si the grain boundaries are electrically active, and that the electronic states localized on them govern the valence bandtail behavior of the material. Some examples of valence bandtail states localized on grain boundaries and in the disordered matrix are shown in Figs. 5.9,5.10 and 5.11. The figures also show the topologically crystalline nature of the grains, retained by construction during the model preparation.

5.2.3 Medium range order

P. Voyles have computed the simulated fluctuation microscopy signals $V(k)$ for our paracrystalline models (for brief introduction to fluctuation electron microscopy

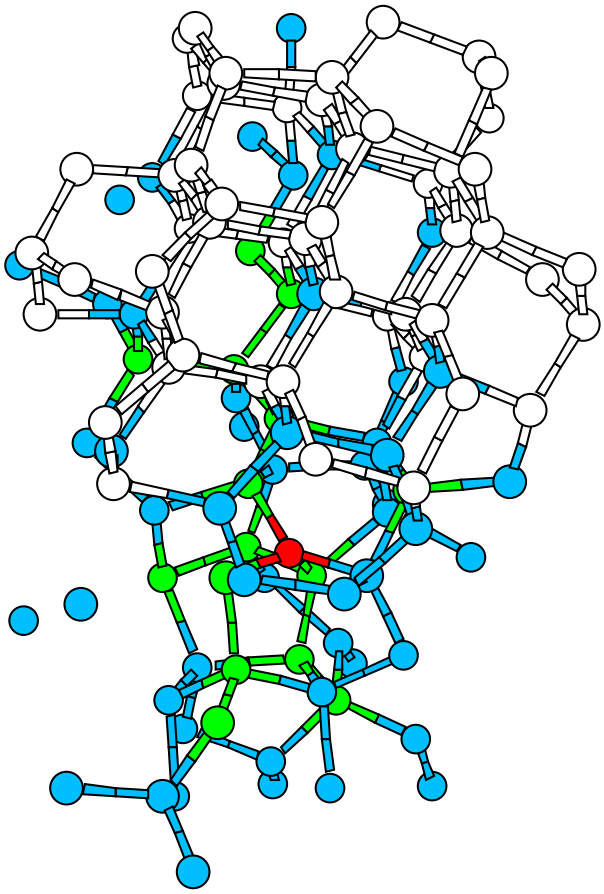

Figure 5.9: **Electronic bandgap state localized on the grain boundary. Each atom pictured in red, yellow, green and blue accounts for more than 20 %, between 10 and 20%, between 1 and 10 % and between 0.1 and 1 % of the total system charge respectively. The atoms pictured in white are all of the other atoms belonging to the grain.**

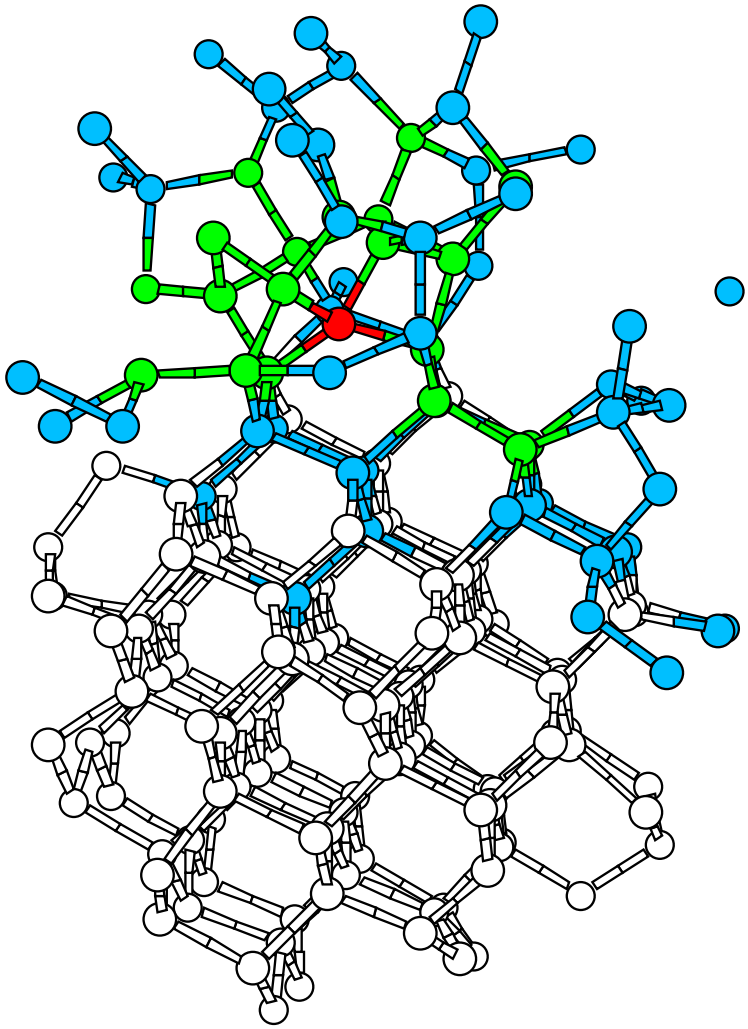

Figure 5.10: **Another bandgap state in 4000 atom paracrystalline Si model localized on a different grain. Color conventions are the same as for Fig. 5.9.**

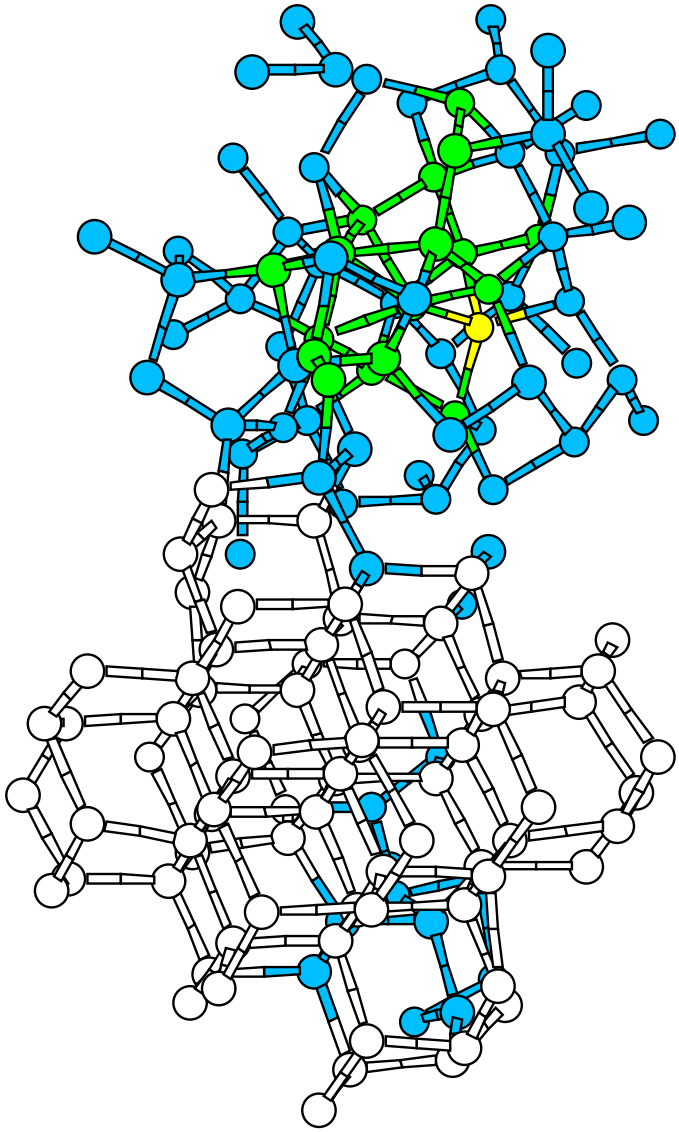

Figure 5.11: **An example of a bandgap state in 4000 atom paracrystalline Si model localized in the disordered matrix. Color conventions are the same as for Fig. 5.9.**

see Appendix B). The simulation results are shown in Fig. 5.12 together with experimental data from a sputtered a-Si thin film [120]. $V(k)$ is the normalized variance of mesoscopic-resolution hollow-cone dark field (HCDF) transmission electron micrographs as a function of the dark-field scattering vector magnitude k [10]. A large $V(k)$ with significant structure in k indicates the sample has significant MRO; a small $V(k)$ with little structure indicates the sample has little or no MRO [11]. Quantitatively, $V(k)$ depends on the three- and four-body atom distribution functions of the sample [121].

$V(k)$ for the models is found by computing the variance of a series of simulated HCDF images of the model. The images were computed in the phase-grating approximation[122], which is adequate for disordered models of this size since dynamical scattering and electron channeling are suppressed in the absence of a crystalline lattice. In an effort to better approach an ensemble average of structures, we compute images for each model in a large number of orientations. This is equivalent to assuming that the grain orientations are uncorrelated, which is also assumed in the model preparation. Images were computed at a resolution of 15 Å to match the resolution used in the experiment.

Despite the use of the phase-grating approximation, there are residual effects in $V(k)$ from the different number of unique atoms in the models. These have been corrected using a variation on the empirical thickness correction technique developed for a-Si thin film experimental measurements [123]. The thickness correction expression contains a parameter that allows for the formation of a surface oxide on the thin foil;

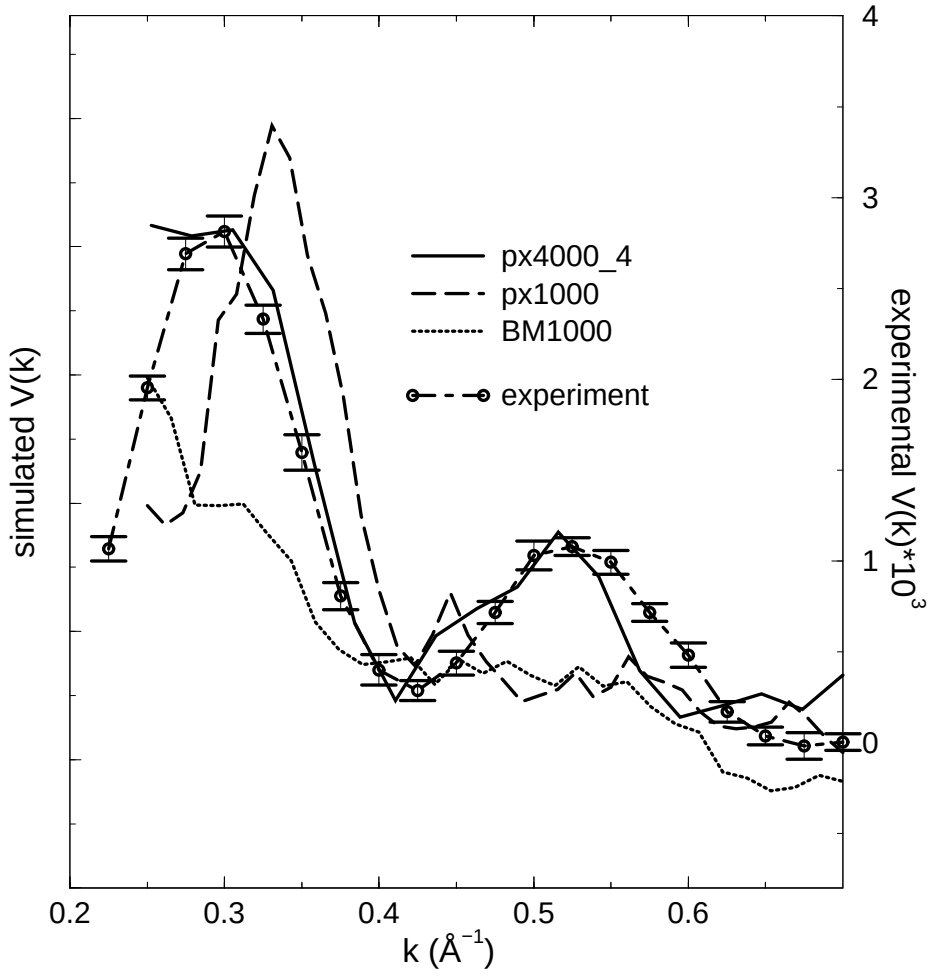

Figure 5.12: **Simulated fluctuation microscopy signal $V(k)$ for the models, and experimental measurements for a sputtered a-Si thin film, all at 15 Å resolution. All the data for this graph has been provided by P. M. Voyles and is reproduced by kind permission.**

that parameter has been set to zero for these calculations since the models have no oxide.

The raw simulated $V(k)$ is larger than the measured variance by approximately an order of magnitude. This is due to several effects, the first of which is the small size of the models (at most 43 Å) compared to the thickness of the experimental samples, which is ~200 Å. The empirical thickness correction cannot fully correct for this because the experimentally-determined fitting parameters employed are not sufficiently accurate, making the procedure unreliable for large thickness corrections. It has been employed in the experiments to correct for small thickness perturbations; it is used here in the same spirit to make the models comparable to one another. The experimental images are also bandpass filtered to remove experimental artifacts associated with sample non-uniformities, but the simulated images are too small for this treatment. The simulations also do not account for several sources of small angle scattering, including inelastic scattering, multiple scattering, and thermal diffuse scattering, which are present to some degree in the experimental measurement, and will tend to reduce the image variance. All of these effects (thickness, filtering, and small-angle scattering) are k independent, so in Fig. 5.12 we have simply scaled all the data by a multiplicative factor to get the best match to the experimental data for the best model, which is px4000_4 (see below). We then interpret the simulations only in terms of the positions and relative magnitudes of features in $V(k)$.

$V(k)$ for BM1000 shows the nearly featureless $V(k)$ that is typical of CRN models [114, 117]. px1000 shows the prominent peak at $k = 0.3$ Å^{-1} that is observed in

the experiment and is a measurable signature of paracrystallinity. It does not fully reproduce the second peak at $k = 0.55$ Å^{-1} seen in the data, likely because it has only one grain and a very small degree of MRO. The simulated $V(k)$ curve for our largest model, px4000_4, presents the best match currently available to the experiment: the simulated $V(k)$ closely follows the shape of the experimental curve and correctly reproduces the ratio of the first to the second peak heights and positions of the both peaks.

It is unlikely that the combination of grain size, density, shape, spatial distribution, and orientation distribution in px4000_4 is unique in producing a $V(k)$ with this level of agreement with experiment. Further simulations are required to explore the effects of all these parameters on the shape and magnitude of $V(k)$. Improved $V(k)$ simulations should also bring the simulated magnitude closer to the experimental value.

5.3 Crystallization of the paracrystalline and CRN models of Si

Another interesting question we can investigate using our paracrystalline models is what happens when we anneal the model material at constant temperature for a relatively long time. Will the crystalline grains grow or will they be completely absorbed by the disordered phase?

We have employed our empirical MD code based on the MSW potential to perform

all the simulations. The principle of least constraint[1] invented by Gauss[124] has been used to keep temperature constant throughout the simulation. The models have been first quenched to zero forces, then annealed at constant temperature for 1 ns and finally quenched to zero forces again.

We have used a program provided by G. Barkema to study the structure of the models before and after the simulated annealing. The program searches for traces of crystallinity in the system identifying the two degenerate ordered states in Si: the diamond-type (tetrahedral) state and the ice-type (hexagonal) state. The criterion used to identify a nanocrystal of the diamond structure, is that for six atoms in a native ring ABCDEF atoms A, C, and E have neighbors NA, NC, and NE, such that those three have a common neighbor X. The structure of these ten atoms is the smallest three-dimensional structure that is part of the diamond crystal. The criterion used to identify a nanocrystal of the hexagonal structure, is that there are two such six-fold rings, that are bonded in three places at alternating locations along the rings.

We start presenting our results with px400 model. In Fig. 5.13 we show the number of diamond-type and hexagonal crystalline clusters found in the model after 1 ns anneal at different temperatures. The 0 K points are for the initial configuration that has not been annealed (just quenched to zero forces). From the figure we can see that for px400 there exists a strong maximum in the number of diamond-type

[1] A fundamental dynamical principle allowing the nonholonomic (velocity-dependent) constraints to be used to maintain a steady nonequilibrium state of many-body system.

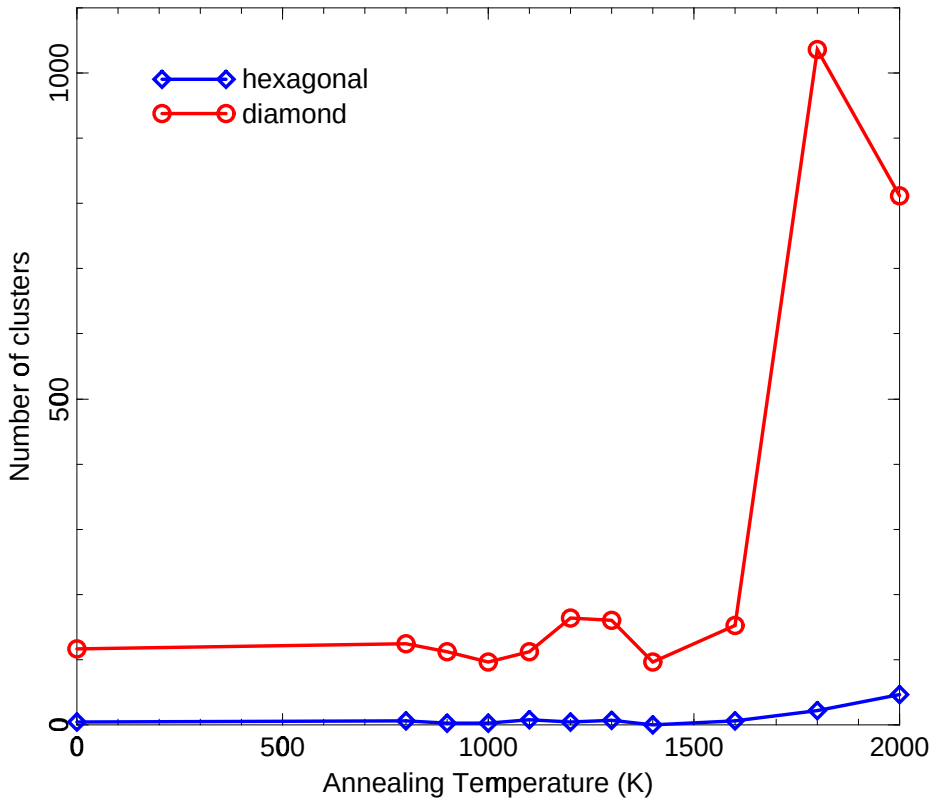

Figure 5.13: **The number of crystalline clusters for various anneal temperatures in px400 model.**

clusters at approximately 1800 K[2]. At temperatures higher than 2000 K the system starts to melt.

The colormaps for the initial configuration and for configuration after 1 ns anneal at 1800 K and subsequent quench are shown in Figs. 5.14 and 5.15 respectively. The former figure shows that there is a substantial amount of crystalline clusters in the initial (unannealed) configuration for the model and these clusters are concentrated in the area on the crystalline grain and around it. The latter figure shows that after annealing the system is almost completely crystallized — we believe that we have not been able to completely crystallize the model because it contains the number of atoms that can not form a perfect crystal with periodic boundary conditions applied (i.e. the number of atoms in the model is not n^3 like $6^3 = 216$ or $10^3 = 1000$).

In the next set of figures we present the analogous information for px1000 model. The diamond-type and hexagonal cluster concentration for different anneal temperatures is shown in Fig. 5.16. Just like for the previous model the number of diamond-type clusters grows very rapidly as we get into the temperature region of 1800-2100 K. For px1000 the best crystallization temperature (2100 K) is somewhat higher than for px400 which may be connected with the difference in size of the models: for a smaller system less thermal energy is required for atomic rearrangements.

The initial (unannealed) configuration colormap for px1000 model is shown in

[2]We must point out that the temperatures at which crystallization takes place in our models are higher than the *experimental* melting temperature for Si. This is because in computer simulations the system's temperature is derived from the interatomic potential which *may not be fitted* to reproduce the real melting temperature of the material and due to the finite size of the model system and the fact that it superheats before melting.

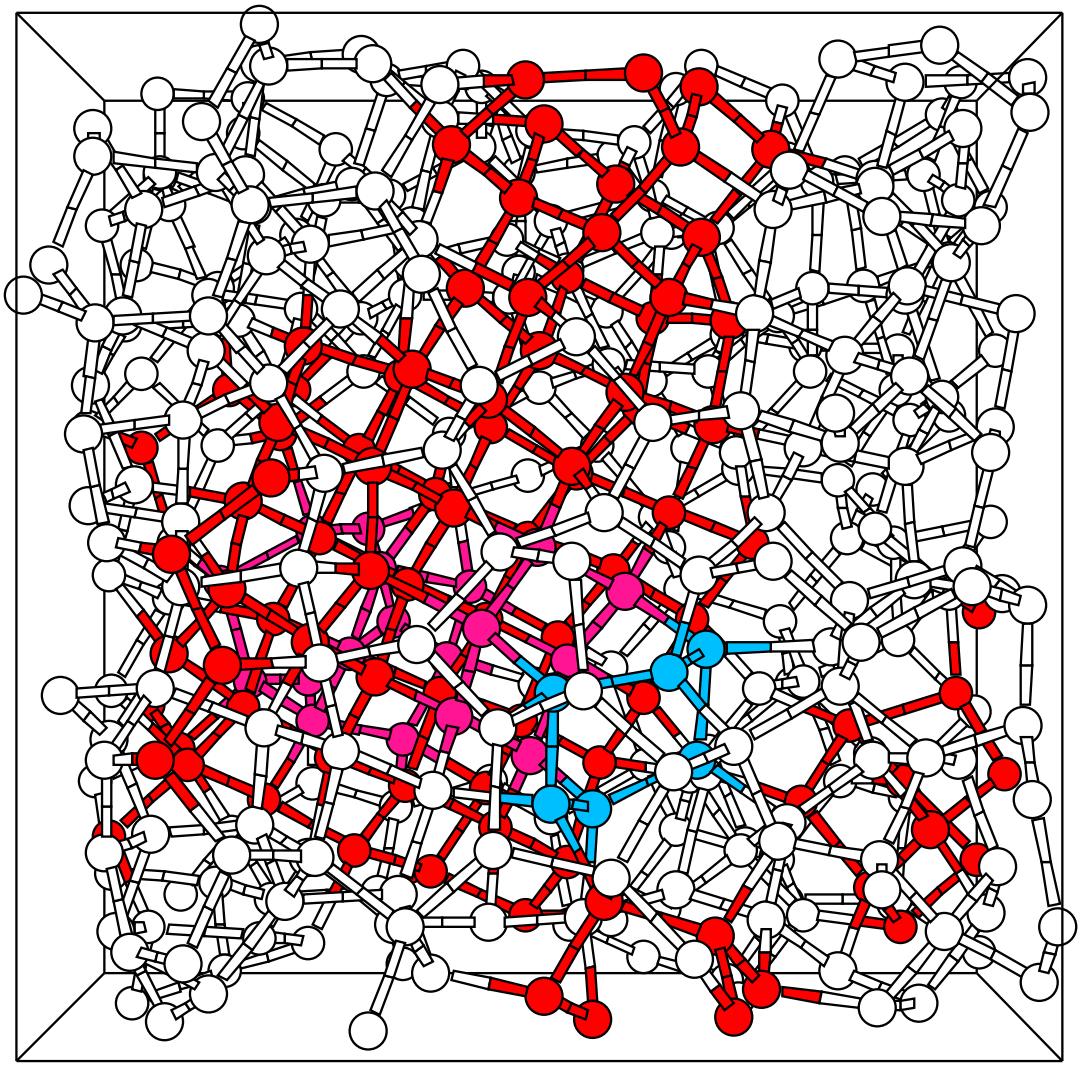

Figure 5.14: **Crystalline clusters in px400 model (unannealed configuration). Atoms pictured in red and blue are the members of diamond-type and hexagonal clusters respectively. Atoms pictured in pink are the members of both types of clusters simultaneously. Atoms pictured in white do not belong to any type of crystalline clusters.**

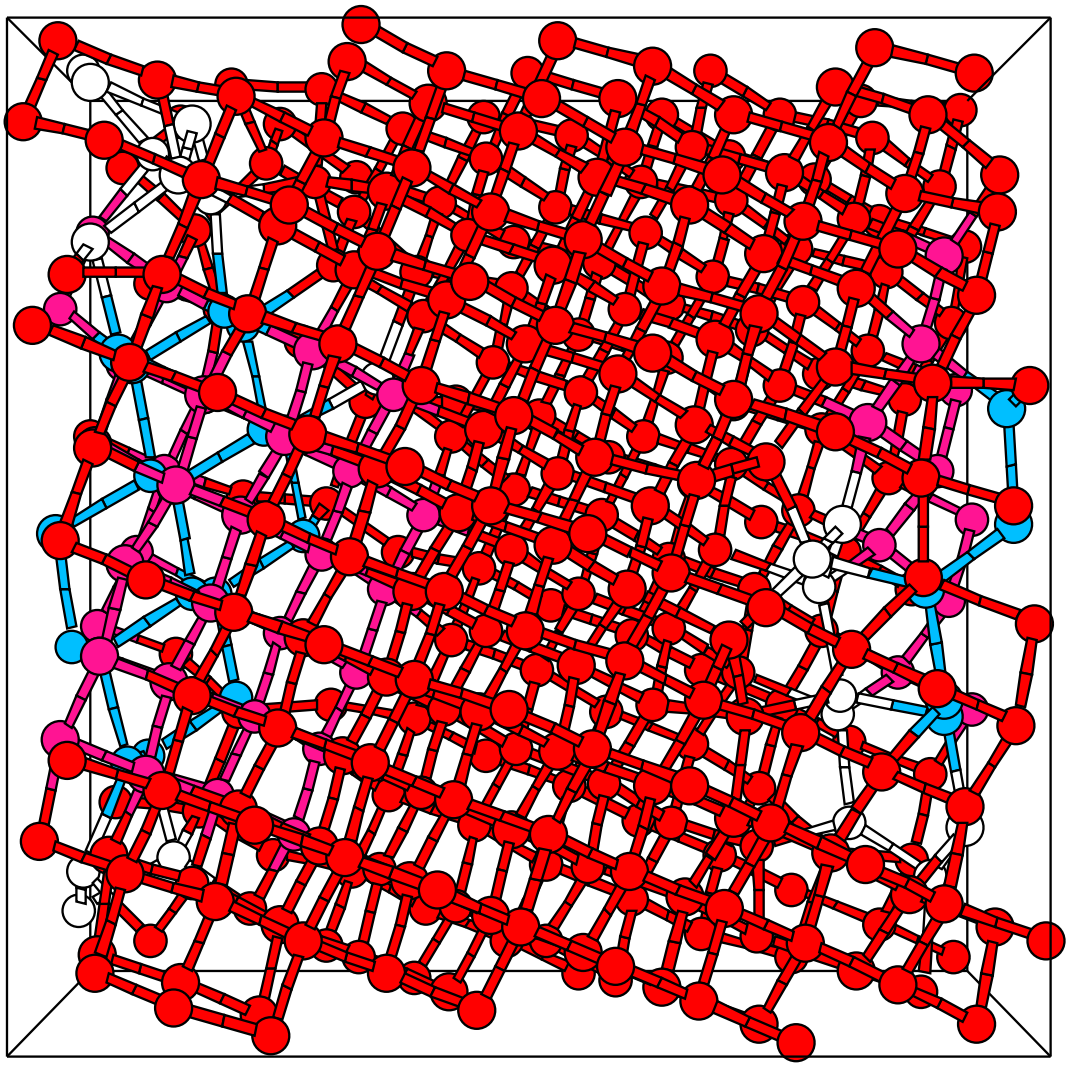

Figure 5.15: **Crystalline clusters in px400 model after anneal at 1800 K. Color conventions are the same as for Fig. 5.14.**

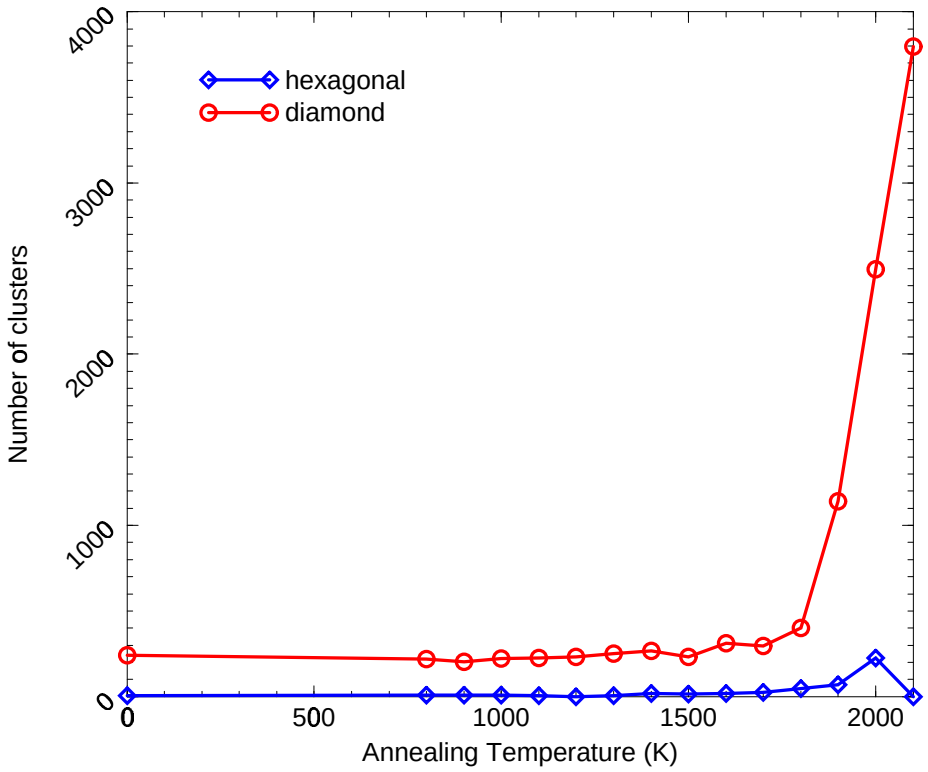

Figure 5.16: **The number of crystalline clusters for various anneal temperatures in px1000 model.**

Fig. 5.17, it looks very similar to the analogous colormap for the smaller model px400. The colormap for the model after 1 ns anneal at 2100 K and subsequent quench is presented in Fig. 5.18 — with an exception of a few defects a perfect diamond-type crystal.

As we have a good CRN model for a-Si (BM1000) with the same number of atoms as in px1000 we have performed the 1 ns anneal for it as well. The simulation was made at the same temperature at which full crystallization of px1000 had been observed, i.e. 2100 K. The initial (unannealed) configuration and a configuration after anneal and quench for BM1000 CRN model are shown in Figs. 5.19 and 5.20. The former figure shows that the CRN model indeed does have some network regions in it that look crystalline. Our opinion here is that possibly the energy minimization technique employed to create this model (see section 3.1) is so efficient that on final stages of the modeling process it eventually starts to crystallize the model even though the initial structure used to create the model is completely random. The latter figure for an annealed configuration shows that the CRN model has almost completely crystallized after 1 ns but not in a form of a perfect diamond-type crystal, like px1000, but rather as a random mixture of diamond- and ice-type crystalline phases. We would attribute this difference to the fact that obviously our paracrystalline model has a strong crystallization center in it — the grain, which sets the preferred crystallization phase and direction. As we can see from Fig. 5.19 there are some small crystallization centers in the CRN model as well but they are randomly scattered across the supercell, which probably triggers the "mixed phase" crystallization.

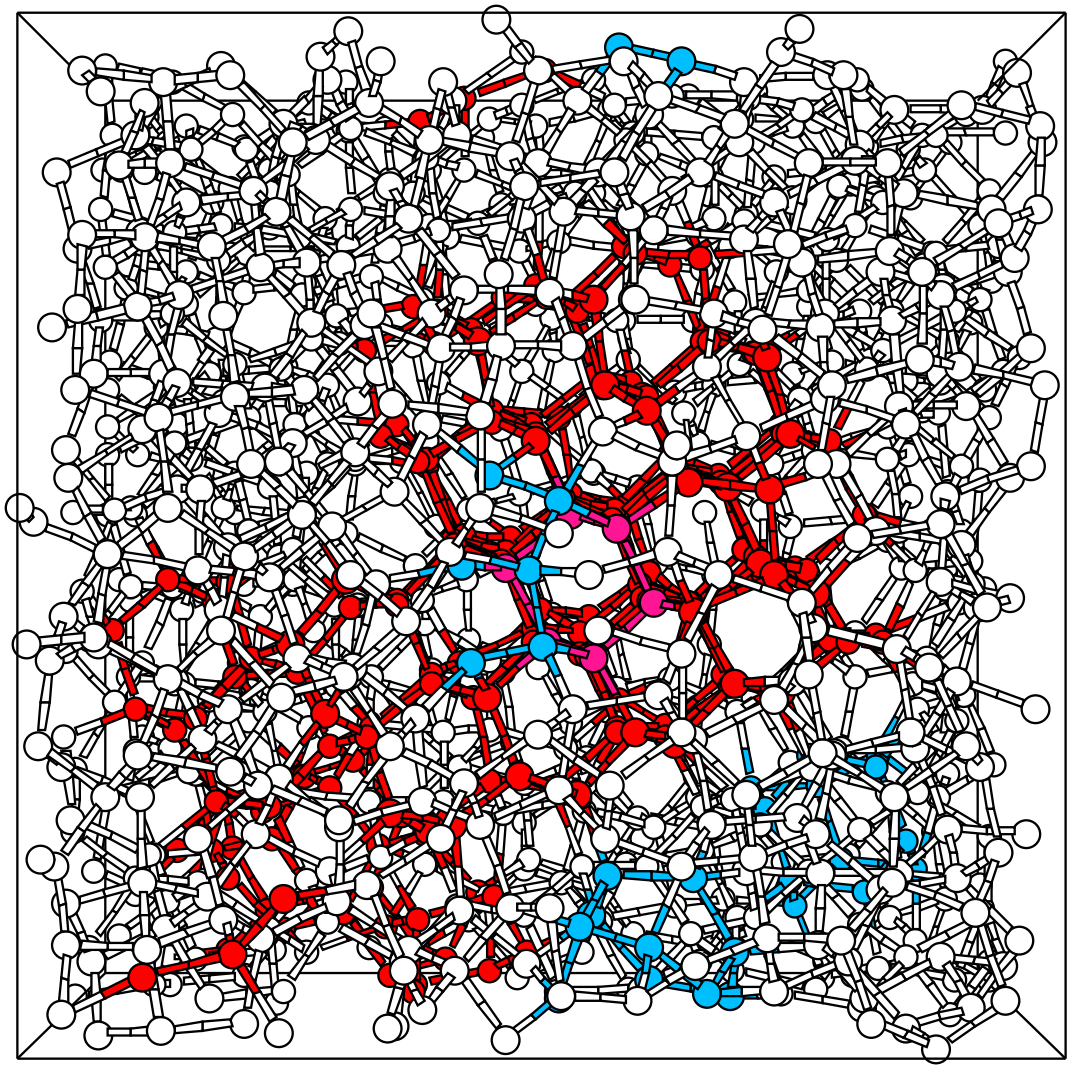

Figure 5.17: **Crystalline clusters in px1000 model (unannealed configuration). Color conventions are the same as for Fig. 5.14.**

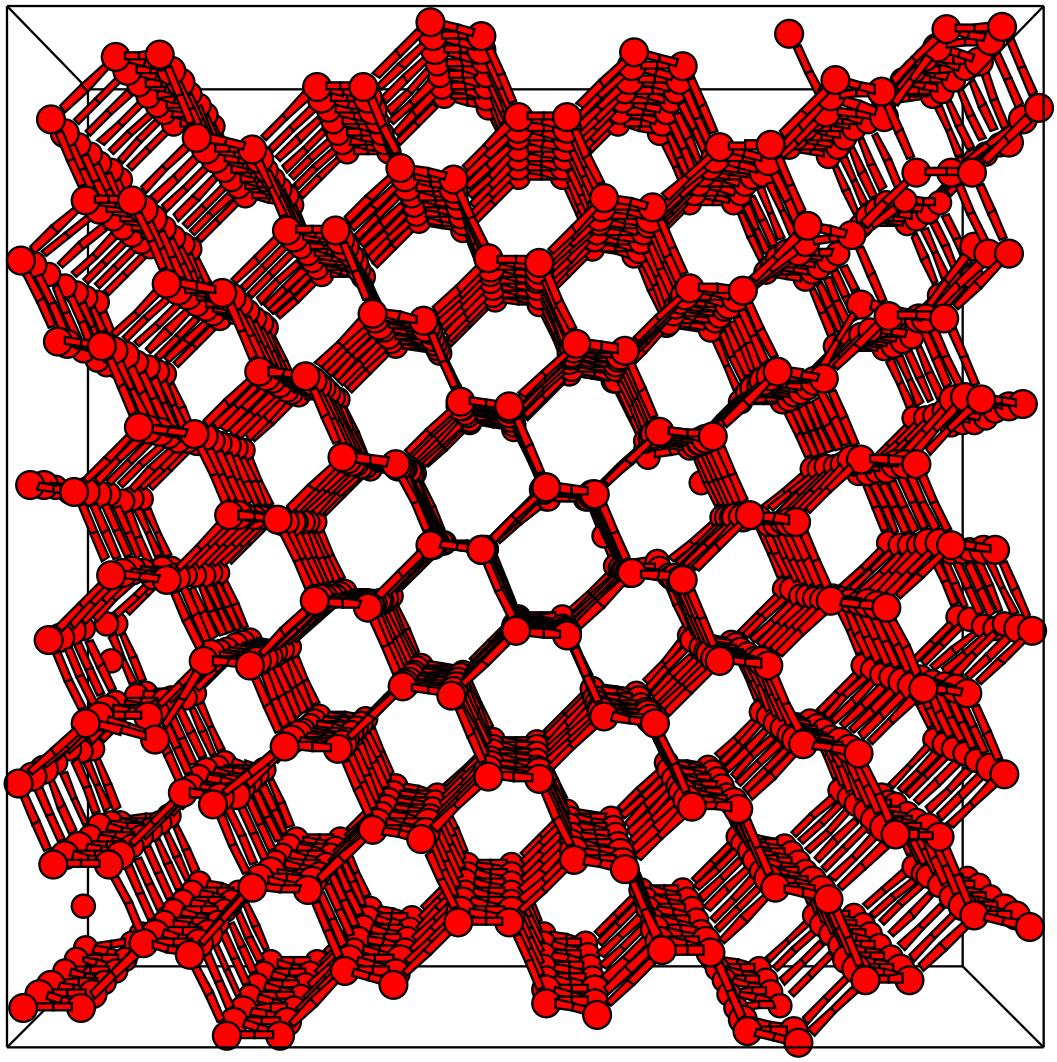

Figure 5.18: **Crystalline clusters in px1000 model after anneal at 2100 K. Color conventions are the same as for Fig. 5.14.**

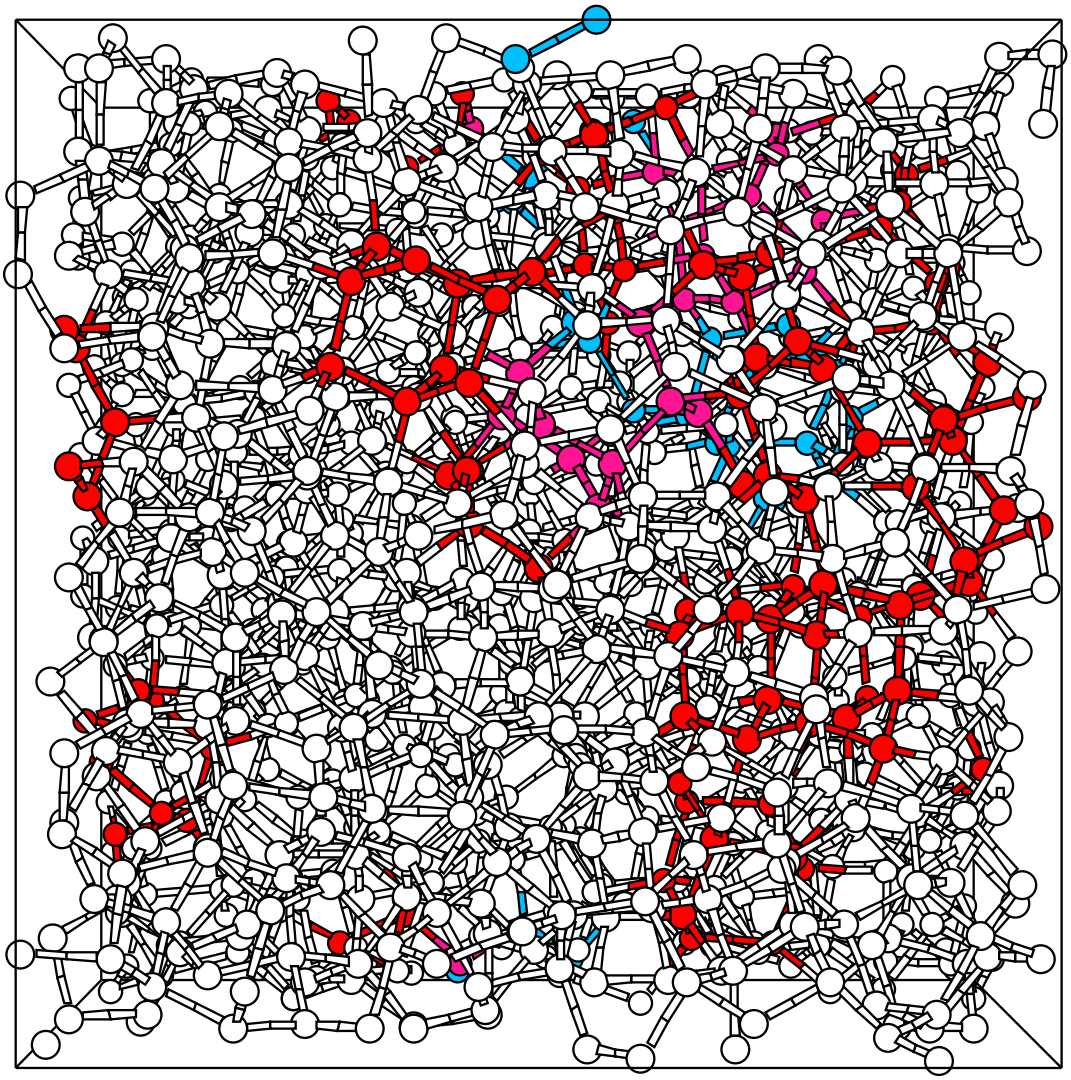

Figure 5.19: **Crystalline clusters in BM1000 model (unannealed configuration). Color conventions are the same as for Fig. 5.14.**

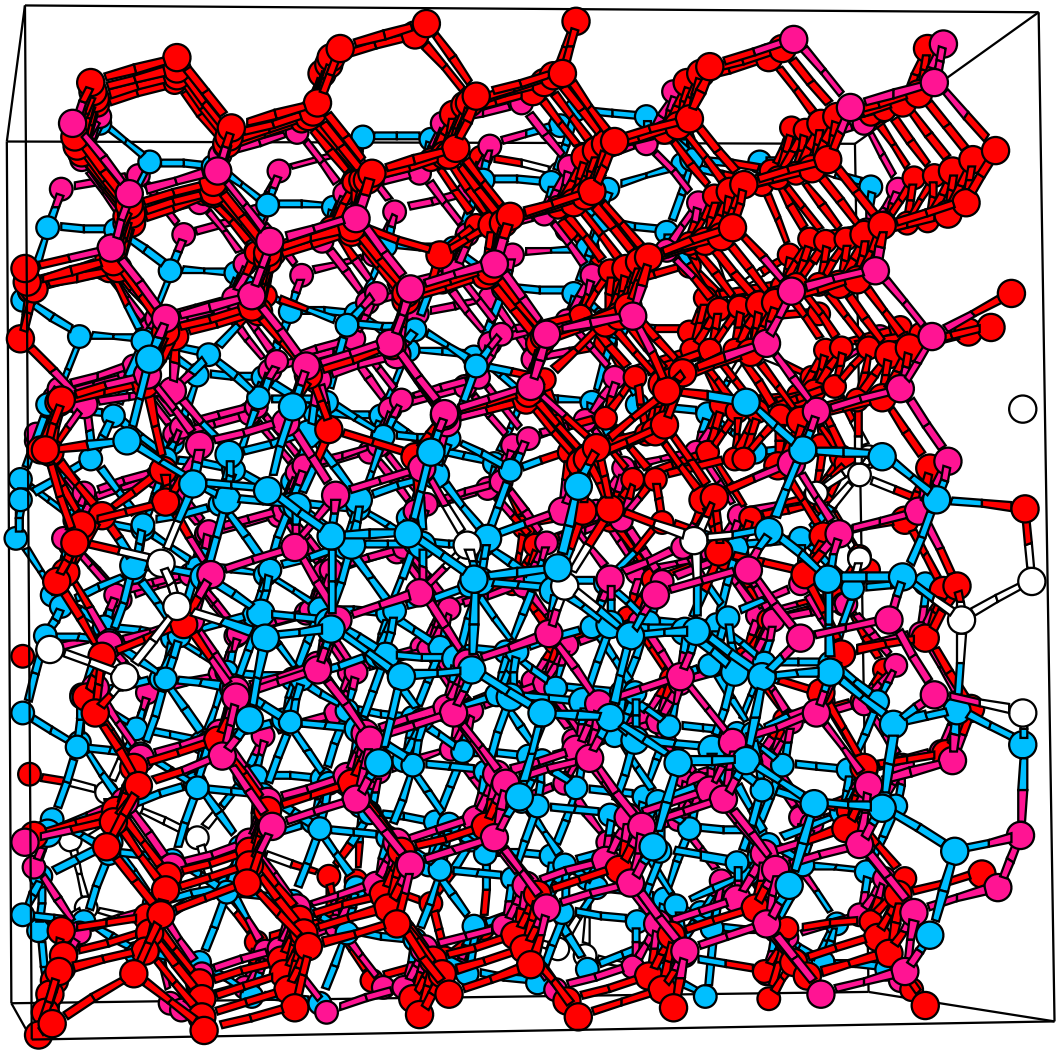

Figure 5.20: **Crystalline clusters in bm1000 model after anneal at 2100 K. Color conventions are the same as for Fig. 5.14.**

Finally we present the results for our largest 4000 atom paracrystalline model px4000_4. Due to heavy computational load we have performed only three 1 ns constant temperature anneal simulations for the model — at temperatures of 1800, 2000 and 2200 K. The colormap for the initial (unannealed) configuration for px4000_4 is shown in Fig. 5.21. The areas occupied by four crystalline grains can be clearly seen in the corners of the box as well as a number of smaller string-like crystalline clusters randomly positioned in the supercell. The latter ones most probably have the same nature as the clusters we have encountered in the CRN model BM1000 (see Fig. 5.19). The colormap for the model after 1 ns anneal at 2200 K and subsequent quench is presented in Fig. 5.22.

We can see that, much like in case of all the smaller models discussed above, the system has crystallized. It is hard to derive absolutely precise information from the picture but it looks like the initial crystalline grains started to grow ordering atoms around them — and these areas crystallized mostly in the diamond-type phase which, as we have seen before, also happens in small paracrystalline models that contain only one grain — until their regions of growth start to interpenetrate. Then the boundary regions between the diamond-type growth areas are formed, and it seems that these regions have the hexagonal phase as preferred crystallization phase. This is, of course, a very simplistic view on the problem. However we can *speculate* that with a simulation of the type we presented above one can construct a realistic model of nano- or polycrystalline silicon — materials that unlike paracrystalline Si contain approximately 90% of crystalline Si in a form of randomly oriented large (hundreds

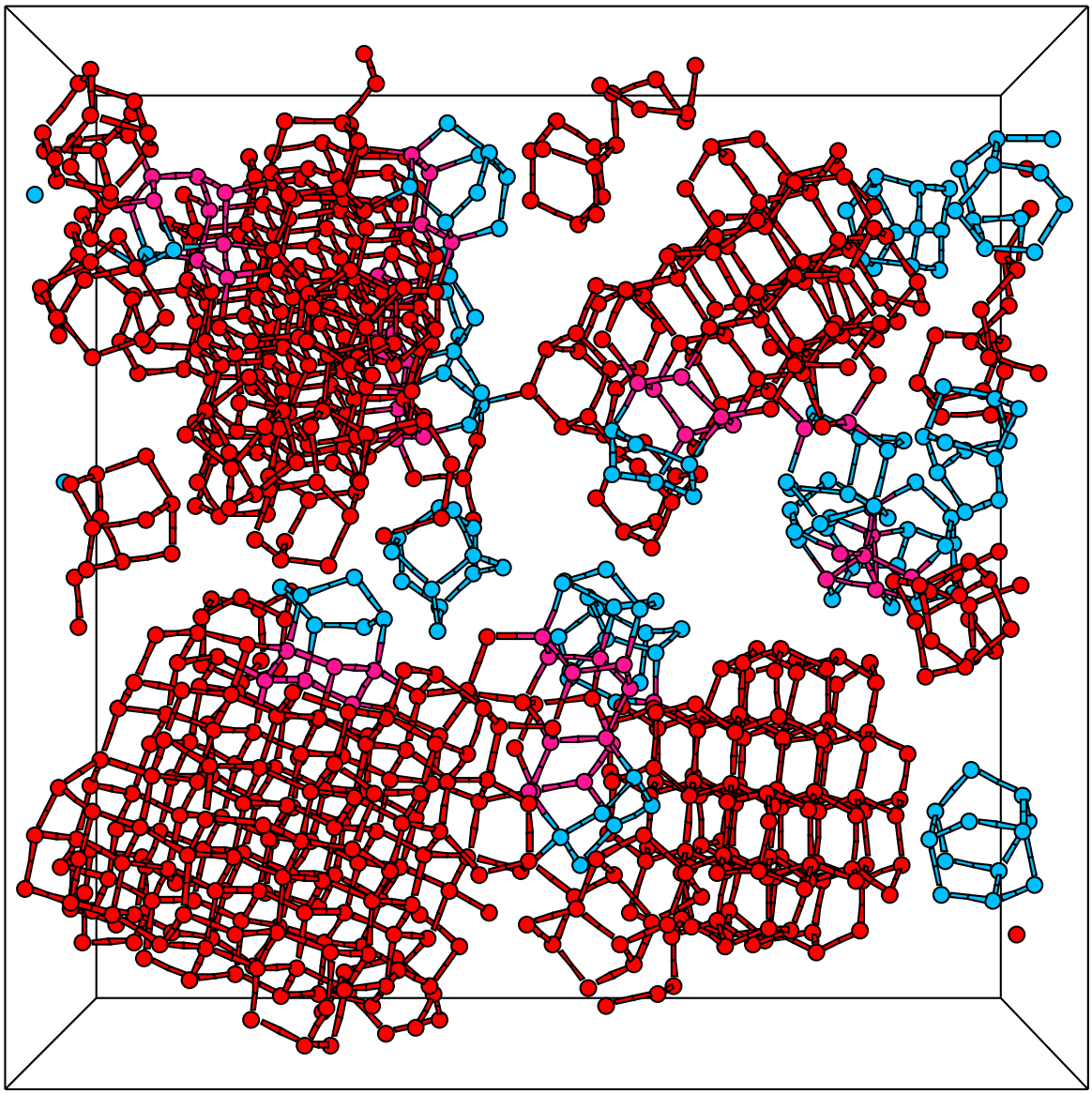

Figure 5.21: **Crystalline clusters in px4000_4 model (unannealed configuration). Color conventions are the same as for Fig. 5.14 except for atoms that do not belong to any crystalline clusters — these atoms are not shown.**

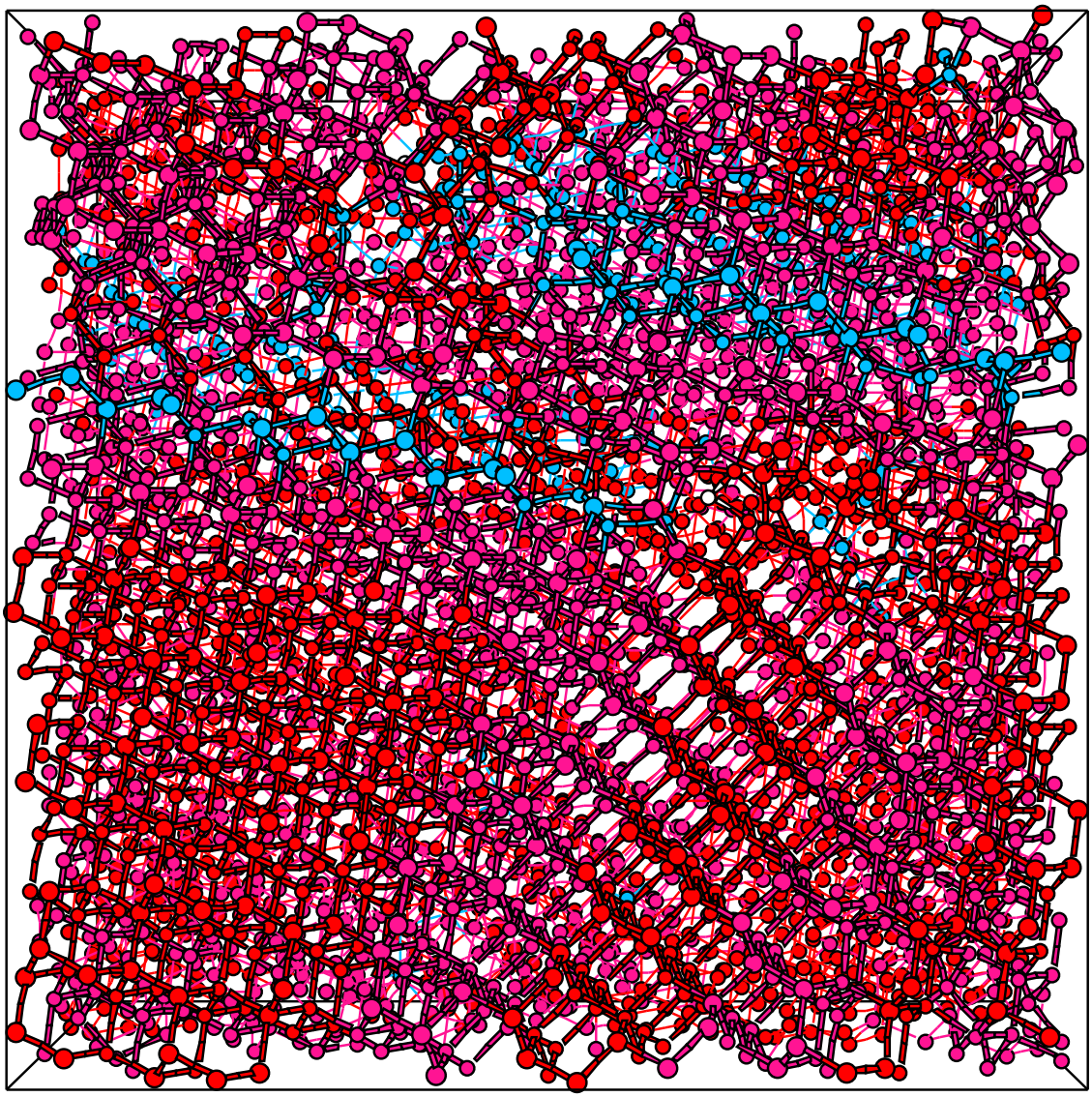

Figure 5.22: **Crystalline clusters in px4000_4 model after anneal at 2200 K. Color conventions are the same as for Fig. 5.21.**

or thousands of angstroms and more) crystalline grains separated only by a couple of atomic layers of severely strained disordered atoms.

For the sake of comparison in Fig. 5.23 we present the structural properties of px4000_4 model before and after the constant temperature anneal. The RDF of the annealed configuration looks much more like the RDF of the diamond crystal than for amorphous material, while the bond-angle distributions for it are strongly concentrated around the perfect crystalline angles.

5.4 Conclusions

To summarize, we have created a family of models for paracrystalline Si which not only have structural MRO in qualitative agreement with experiment, but also have realistic vibrational, structural and optical properties. The EDOS bandgaps are comparable in width with the gap for the best CRN models for *a*-Si. Except for measurements focused directly on the medium-range order, it is essentially impossible to distinguish between the amorphous and the paracrystalline models.

The evidence presented here shows that our models can serve as a reasonable description for tetravalent, paracrystalline, semiconducting material and as testing grounds for measurements of medium-range order in disordered semiconductors.

We should also point out that our method of constructing paracrystalline Si models can be also used to build perfectly connected crystalline-to-amorphous interfaces in Si or SiO_2.

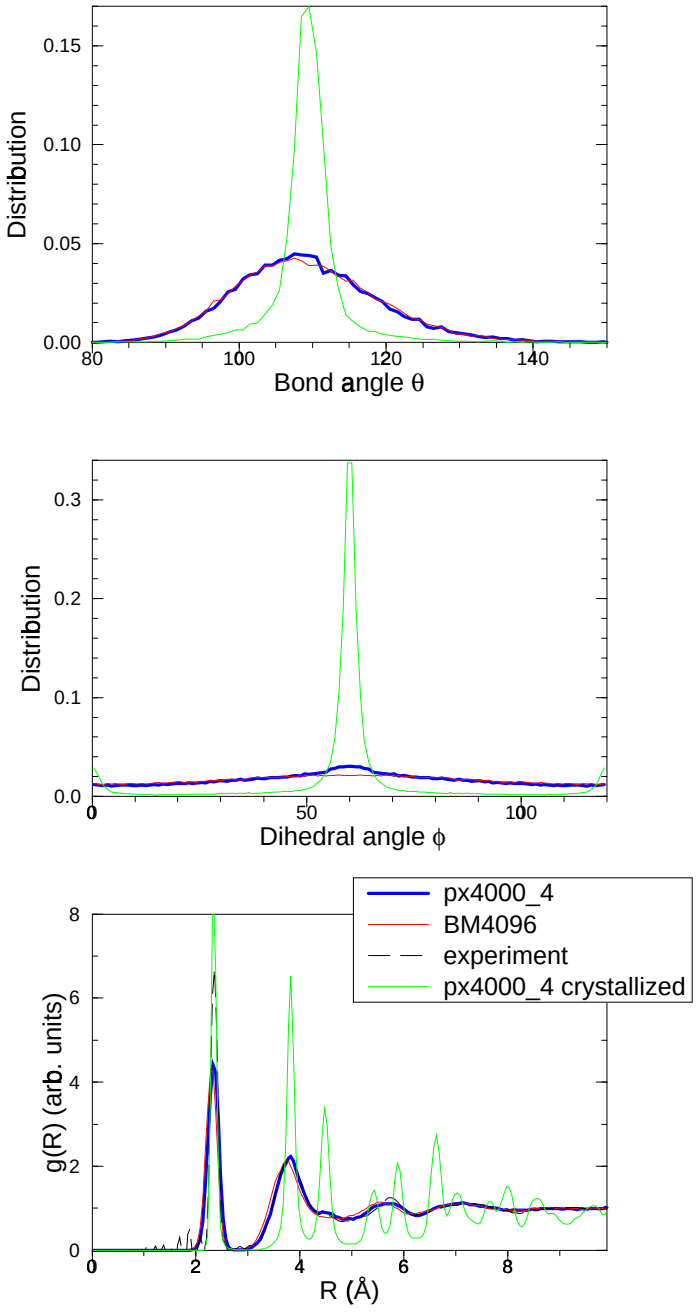

Figure 5.23: **Structural properties of px4000_4 model after 1 ns anneal at 2200 K. Note the scale change compared to Figs. 5.3 and 5.4.**

Chapter 6

Concluding remarks and speculations for future work

6.1 Summary

In this work we have constructed and studied various properties of atomistic models of amorphous silicon with voids and paracrystalline silicon (containing small crystalline grains embedded into disordered matrix). In both cases we have shown that incorporation of physically relevant defects, like voids or crystalline grains, into the structure of the models of disordered tetrahedral semiconductors provides better uniform agreement with known experimental data than for commonly used models for a-Si that contain no defects at all or only atomic coordination defects. We believe that only a model which properties *uniformly comply* with experimental results can serve as a credible representation of a real material for numerical simulations. Evidence presented in this dissertation as well as recent experimental data suggest that in order

to achieve a higher quality level of uniform compliance with experiment the next generation of large models for tetrahedral amorphous semiconductors should incorporate structural defects encountered in real materials which is particularly important for complex simulations of properties of nanoscale electronic devices which will undoubtedly be possible in the very nearest future. We hope that our investigation will help to change the standards in the field, favoring CRN-type models with no defects or even QFM models, and show that more advanced models are required to gain better understanding of internal structure and properties of disordered tetrahedral materials and, what is most important, methods and techniques needed to make some first steps to build and study these new models are readily available.

6.2 Possible future projects

- A straightforward extension of our modeling techniques described in chapters 4 and 5 of this dissertation will be to construct a family of large atomistic models for amorphous silicon containing various concentrations of both voids and crystalline grains embedded into the disordered matrix and study models' properties, especially the influence of the defect concentrations on the experimentally measurable quantities.

- Another computational project that can be easily implemented using our modeling method presented in chapter 5 of this dissertation is to build a family of models for paracrystalline silicon of the same relatively large size (thousands

of atoms) but with different ratios of crystalline-to-disordered phase concentrations. We believe that this investigation can shed some light on the exact nature of peaks of the fluctuation microscopy signal $V(k)$ (which is still unclear) and also determine possible concentrations of crystalline grains in real material.

- The ability of our modeling technique to produce realistic interfaces between disordered and crystalline phases of silicon and silicon oxide can be exploited by creating atomistic models of nanoscale semiconductor devices containing such interfaces (like a-Si based TFTs, for example) and studying their current-voltage characteristics with an *ab initio* technique recently introduced by Demkov, Zhang and Drabold[125]

- Finally, further studies of crystallization in paracrystalline silicon presented in section 5.3 of this dissertation may result in useful technique for modeling granular materials like polycrystalline or nanocrystalline silicon and/or grain boundary regions in them. Currently new semiconductor devices based on *polycrystalline* silicon are being introduced to electronics industry but to our knowledge no atomistic models of this material have been created.

Bibliography

[1] R. A. Street, *Hydrogenated Amorphous Silicon* (Cambridge University Press, Cambridge, 1991).

[2] K. Laaziri, S. Kycia, S. Roorda, M. Chicoine, J. L. Robertson, J. Wang, and S. C. Moss, Phys. Rev. Lett. **82**, 3460 (1999).

[3] K. Laaziri, S. Kycia, S. Roorda, M. Chicoine, J. L. Robertson, J. Wang, and S. C. Moss, Phys. Rev. B **60**, 13520 (1999).

[4] W. A. Kamitakahara, C. M. Soukoulis and H. R. Shanks, U. Buchenau, G. S. Grest, Phys. Rev. B **36** 6539 (1987).

[5] D. K. Biegelsen and M. Stutzmann, Phys. Rev. B **33**, 3006 (1896).

[6] S. T. Pantelides, Phys. Rev. Lett. **57**, 2979 (1986).

[7] P. D'Antonio and J. H. Konnert, Phys. Rev. Lett. **43**, 1161 (1979).

[8] T. A. Postol, C. M. Falco, R. T. Kampwirth, I. K. Schuller and W. B. Yellon, Phys. Rev. Lett. **45**, 648 (1980).

[9] A. J. Craven, A. M. Patterson, A. R. Long and J. I. B. Wilson, J. Non. Cryst. Solids **77–78**, 217 (1986).

[10] M. M. J. Treacy and J. M. Gibson, Acta Cryst. **A52**, 212 (1996).

[11] P. M. Voyles, J. M. Gibson and M. M. J. Treacy, J. Elec. Microscopy **49**, 259 (2000).

[12] S. Hunklinger, in M. F. Thorpe and M. I. Mitkova (eds.) *Amorphous Insulators and Semiconductors* (Kluwer, Dordrecht, 1997).

[13] W. A. Phillips, Rep. Prog. Phys. **50**, 1657 (1987).

[14] For the definition of dynamical matrix see, for example, N. W. Ashcroft and N. D. Mermin *Solid State Physics* (Holt, Rinehart and Winston, New York, 1976).

[15] M. C. Payne, M. P. Teter and D. C. Allan, T. A. Arias and J. D. Joannopoulos, Rev. Mod. Phys. **64**, 1045 (1992).

[16] M. Born, J. R. Oppenheimer, Ann. Phys. **84**, 457 (1927).

[17] P. Hohenberg, W. Kohn, Phys. Rev. B **136**, 864 (1964).

[18] W. Kohn, L. J. Sham, Phys. Rev. A **140**, 1133 (1965).

[19] D. M. Ceperley and G. J. Alder, Phys. Rev. Lett. **45**, 566 (1980).

[20] J. P. Perdew and A. Zunger, Phys. Rev. B **23**, 5048 (1981).

[21] R. Car and M. Parrinello, Phys. Rev. Lett. **55**, 2471 (1985).

[22] N. Trouillier and J. L. Martins, Phys. Rev. B **43**, 1993 (1991).

[23] O. F. Sankey, D. J. Niklewski, Phys. Rev B **40**, 3979 (1989); O. F. Sankey, D. A. Drabold and G. B. Adams, Bull. Am. Phys. Soc. **36**, 924 (1991).

[24] D. R. Hamann, M. Schlüter and C. Chiang, Phys. Rev. Lett. **43**, 1494 (1979).

[25] G. B. Bachelet, D. R. Hamann and M. Schlüter, Phys. Rev. B **26**, 4199 (1982).

[26] J. Harris, Phys. Rev. B **31**, 1770 (1985).

[27] W. A. Harrison, *Electronic Structure and the Properties of Solids: the physics of the chemical bond* (Freeman, San Francisco, 1980).

[28] J. C. Slater and G. F. Koster, Phys. Rev. **94**, 1498 (1954).

[29] R. P. Feynman, Phys. Rev. **56**, 340 (1939); H. Hellmann, *Einfuhrung in die Quantumchemie* (Franz Deutsche, Leipzig, 1937).

[30] D. J. Chadi and M. L. Cohen, Phys. Stat. Sol. (b) **68**, 405 (1975); D. J. Chadi, Phys. Rev. B **29**, 785 (1984) and references therein.

[31] L. Goodwin, A. J. Skinner and D. J. Pettifor, Europhys. Lett. **9**, 701 (1989).

[32] J. L. Mercer, Jr. and M. Y. Chou, Phys. Rev. B **49**, 8506 (1994).

[33] I. Kwon *et al.*, Phys. Rev. B **49**, 7242 (1994).

[34] C. Z. Wang, C. T. Chan and K. M. Ho, Phys. Rev. B **39**, 8586 (1989).

[35] T. J. Lenosky *et al.*, Phys. Rev. B **55**, 1528 (1997).

[36] M. Menon and K. R. Subbaswamy, Phys. Rev. B **50**, 11577 (1994).

[37] D. Porezag, Th. Frauenheim, Th. Köhler, G. Seifert and R. Kaschner, Phys. Rev. B **51**, 12947 (1995); Th. Frauenheim *et al.*, Phys. Rev. B **52**, 11492 (1995).

[38] N. Bernstein *et al.*, Phys. Rev. B **62**, 4477 (2000).

[39] P. N. Keating, Phys. Rev. **145**, 637 (1966).

[40] F. Stillinger and T. Weber, Phys. Rev. B **31**, 5262 (1985).

[41] R. Biswas and D. R. Hamann, Phys. Rev. Lett. **55**, 2001 (1985); R. Biswas and D. R. Hamann, Phys. Rev. B **36**, 6434 (1987).

[42] J. Tersoff, Phys. Rev. Lett. **56**, 632 (1986); J. Tersoff, Phys. Rev. B **37**, 6991 (1988); J. Tersoff, Phys. Rev. B **38**, 9902 (1988);

[43] M. Z. Bazant, E. Kaxiras and J. F. Justo. Phys. Rev. B **56**, 8542 (1997).

[44] J. F. Justo, M. Z. Bazant, E. Kaxiras, V. V. Bulatov and S. Yip, Phys. Rev. B **58**, 2539 (1998).

[45] E. R. Cowley, Phys. Rev. Lett. **60**, 2379 (1988).

[46] K. Ding and H. C. Andersen, Phys. Rev. B **34**, 6987 (1986).

[47] J. M. Holender and G. J. Morgan, J. Phys.: Condens. Matter, **3** 7241 (1991).

[48] R. L. C. Vink, G. T. Barkema, W. F. van der Weg and N. Mousseau, *to be published.*

[49] Zachariasen, W. H., J. Am. Chem. Soc. **54**, 3841 (1932).

[50] D. E. Polk, J. Non-Cryst. Solids **5**, 365 (1971).

[51] F. Wooten, K. Winer, D. Weaire, Phys. Rev. Lett. **54**, 1392 (1985).

[52] B. R. Djordjević, M. F. Thorpe and F. Wooten, Phys. Rev. B **52**, 5685 (1995).

[53] N. Metropolis, A. Rosenbluth, M. Rosenbluth, A. Teller and E. Teller, J. Chem. Phys. **21**, 1087 (1953).

[54] K. Winer, Phys. Rev. B **35**, 2366 (1987).

[55] G. T. Barkema and N. Mousseau, Phys. Rev. B **62**, 4985 (2000).

[56] B. J. Hickey, G. J. Morgan, D. L. Weaire and F. Wooten, J. Non-Cryst. Solids **77 & 78**, 67 (1985).

[57] S. K. Bose, K. Winer and O. K. Andersen, Phys. Rev. B **37**, 6262 (1988).

[58] For a review see, for example, J. M. Ziman, *Models of disorder: the theoretical physics of homogeneously disordered systems* (Cambridge University Press, Cambridge, 1979).

[59] J. K. Bording, Phys. Rev. B **62**, 7103 (2000).

[60] R. Alben *et al.* Phys. Rev. B **11**, 2271 (1975).

[61] M. Marinov and N. Zotov, Phys. Rev. B **55**, 2938 (1997).

[62] R. L. C. Vink, G. T. Barkema and W. F. van der Weg, *to appear in Phys. Rev. B.*

[63] O. F. Sankey and G. B. Adams, *unpublished.*

[64] N. Mousseau and D. A. Drabold, European Physical Journal B **17**, 667 (2000).

[65] ©1993 Research Equipment, Inc., Minnesota Supercomputer Center, Inc.

[66] R. Biswas, C. Z. Wang, C. T. Chan, K. M. Ho and C. M. Soukoulis, Phys. Rev. Lett. **63**, 1491 (1989).

[67] M. Fornari, M. Peressi, S. de Gironcoli and A. Baldereschi, Europhys. Lett. **47**, 481 (1999).

[68] J. Dong and D. A. Drabold, Phys. Rev. Lett. **80**, 1928 (1998).

[69] A. P. Sokolov, A. P. Shebanin, O. A. Golikova and M. M. Mezdrogina, J. Phys.: Condens. Matter **3**, 9887 (1991).

[70] D.A. Drabold and O.F. Sankey, Phys. Rev. Lett. **70**, 3631 (1993), and references therein; J. Dong and D.A. Drabold, *unpublished.*

[71] C. Lanczos, J. Res. Nat. Bur. Stand. **45**, 255 (1950); A sophisticated and convenient implementation of the Lanczos method is due to M. T. Jones and M. L. Patrick: 1989, available from netlib as "lanz".

[72] D.J. Thouless, Phys. Rept. **13** 93 (1974).

[73] R. Car and M. Parrinello, Phys. Rev. Lett. **60**, 204 (1988); I. Štich, R. Car and M. Parrinello, Phys. Rev. B **44**, 11092 (1991).

[74] D. A. Drabold, P. A. Fedders, O. F. Sankey and J. D. Dow, Phys. Rev. B **42**, 5135 (1990).

[75] I. Lee and K. J. Chang, Phys. Rev. B **50**, 18083 (1994).

[76] N. Takeuchi and I. L. Garzón, Sol. State. Commun. **98**, 591 (1996).

[77] N. C. Cooper, C. M. Goringe and D. R. McKenzie, Comp. Mat. Science **17**, 1 (2000).

[78] G. Servalli and L. Colombo, Europhys. Lett. **22**, 107 (1993).

[79] E. Kim and Y. H. Lee, Phys. Rev. B **49**, 1743 (1994).

[80] P. Klein, H. M. Urbassek, T. Frauenheim, Comp. Mat. Sci. **13**, 252 (1999); H. M. Urbassek and P. Klein, Phys. Stat. Sol. (b) **217**, 461 (2000).

[81] P. Klein, Modelling Simul. Mater. Sci. Eng. **6**, 405 (1998).

[82] M. D. Kluge, J. R. Ray and A. Rahman, Phys. Rev. B **36**, 4234 (1987); M. D. Kluge and J. R. Ray, Phys. Rev. B **37**, 4132 (1988).

[83] R. Biswas, G. S. Grest and C. M. Soukoulis, Phys. Rev. B **36**, 7437 (1987).

[84] W. D. Luedtke and U. Landman, Phys. Rev. B **37**, 4656 (1988); W. D. Luedtke and U. Landman, Phys. Rev. B **40**, 1164 (1989).

[85] H. C. Andersen, J. Chem. Phys. **72**, 2384 (1980).

[86] M. Parrinello and A. Rahman, Phys. Rev. Lett. **45**, 1196 (1980).

[87] J. Q. Broughton and X. P. Li, Phys. Rev. B **35**, 9120 (1987)

[88] J. L. Mercer, Jr. and M. Y. Chou, Phys. Rev. B **43**, 6768 (1991).

[89] M. Ishimaru, S. Munetoh and T. Motooka, Phys. Rev. B **56**, 15133 (1997).

[90] J. M. Holender and G. J. Morgan, J. Phys.: Condens. Matter, **3** 1947 (1991).

[91] J. M. Holender and G. J. Morgan, J. Phys.: Condens. Matter, **4** 4473 (1992).

[92] N. Zotov, in M. F. Thorpe and M. I. Mitkova (eds.) *Amorphous Insulators and Semiconductors* (Kluwer, Dordrecht, 1997).

[93] R. L. McGreevy and L. Pusztai, Molec. Sim. **1**, 369 (1988).

[94] R. L. McGreevy, M. A. Howe, D. A. Keen and K. Clausen, IOP Conference Series **107**, 165 (1990).

[95] L. Pusztai and S. Kugler, J. Non-Cryst. Solids **164–166**, 147 (1993); S. Kugler, L. Pusztai, L. Rosta, P. Chieux and R. Bellissent, Phys. Rev. B **48**, 7685 (1993); see also L. Pusztai in M. F. Thorpe and M. I. Mitkova (eds.) *Amorphous Insulators and Semiconductors* (Kluwer, Dordrecht, 1997).

[96] O. Gereben and L. Pusztai, Phys. Rev. B **50**, 14136 (1994); L. Pusztai and O. Gereben, J. Non-Cryst. Solids **192 & 193**, 640 (1995).

[97] V. Rosato and M. Celino, J. Appl. Phys. **86**, 6826 (1999).

[98] G. T. Barkema and N. Mousseau, Phys. Rev. Lett. **77**, 4358 (1996).

[99] N. Mousseau and G. T. Barkema, Phys. Rev. E **57**, 2419 (1998).

[100] N. Mousseau and L. J. Lewis, Phys. Rev. Lett. **78**, 1484 (1997); N. Mousseau and L. J. Lewis, Phys. Rev. B **56**, 9461 (1997).

[101] G. T. Barkema and N. Mousseau, Phys. Rev. Lett. **81**, 1865 (1998).

[102] R. Biswas *et al.* Phys. Rev. Lett. **60**, 2280 (1988).

[103] R. Biswas *et al.* Phys. Rev. B **39**, 5101 (1989).

[104] A. Chehaidar, M. Djafari Rouhani, A. Zwick, J. Non-Cryst. Solids **192 & 193**, 238 (1995).

[105] X. Liu, B. E. White, Jr., R. O. Pohl, E. Iwanizcko, K. M. Jones, A. H. Mahan, B. N. Nelson, R. S. Crandall and S. Veprek, Phys. Rev. Lett. **78**, 4418 (1997); X. Liu, P. D. Vu, R. O. Pohl, F. Schiettekatte and S. Roorda, Phys. Rev. Lett. **81**, 3171 (1998).

[106] S. M. Nakhmanson and D. A. Drabold, Phys. Rev. B **58**, 15325 (1998).

[107] S. M. Nakhmanson and D. A. Drabold, J. Non-Cryst. Solids **266–269**, 156 (2000).

[108] S. M. Nakhmanson and D. A. Drabold, Phys. Rev. B **61** 5376 (2000).

[109] J. L. Feldman, P. B. Allen, S. R. Bickham, Phys. Rev. B **59**, 3551 (1999).

[110] See, for example, Sec. IV of A. A. Maradudin *et. al.*, *Theory of Lattice Dynamics in the Harmonic Approximation* (Academic Press, New York and London, 1971).

[111] J. L. Feldman (private communication); for the elastic constants calculation details, see J. L. Feldman and J. Q. Broughton, F. Wooten, Phys. Rev. B **43**, 2152 (1991), and references therein.

[112] M. Mertig, G. Pompe and E. Hegenbarth, Solid State Commun. **49**, 369 (1984).

[113] M. Coeck, C. Laermans, Phys. Rev. B **58**, 6708 (1998).

[114] M. M. J. Treacy, J. M. Gibson and P. J. Keblinski, J. Non-Cryst. Solids **231**, 99 (1998).

[115] S. Nakhmanson, N. Mousseau, G. T. Barkema, P. M. Voyles and D. A. Drabold, to appear in Intl. J. Mod. Phys.; S. Nakhmanson, P. M. Voyles, N. Mousseau, G. T. Barkema and D. A. Drabold, submitted to Phys. Rev. B.

[116] The electronic density of states of the model, presented in Ref. [44], has been recently calculated by N. Bernstein *et al.* in Ref. [38].

[117] P. M. Voyles, N. Zotov, S. M. Nakhmanson, D. A. Drabold, J. M. Gibson, M. M. J. Treacy, P. Keblinski, *submitted to* J. Appl. Phys.

[118] P. Keblinski, S. R. Phillpot, D. Wolf and H. Gleiter, Acta Mater. **45**, 987 (1997).

[119] S. Nomura *et al.*, Phys. Rev. B **54**, 13974 (1996), Mat. Sci. Eng. B **51** 146 (1998).

[120] P. M. Voyles, J. E. Gerbi, M. M. J. Treacy, J. M. Gibson, and J. R. Abelson, *to be published.*

[121] J. M. Gibson, M. M. J. Treacy, and P. M. Voyles, Ultramicroscopy **83**, 169 (2000).

[122] David B. Williams and C. Barry Carter, *Transmission Electron Microscopy: A Textbook for Materials Science* (Plenum Press, New York, 1996), p. 485.

[123] P. M. Voyles, M. M. J. Treacy, J. M. Gibson, H-C. Jin, and J. R. Abelson, Mat. Res. Soc. Symp. Proc. **589**, *to be published.*

[124] D. J. Evans *et al.* Phys. Rev. A **28**, 1016 (1983); K. F. Gauss, J. Reine Angew. Math. **IV**, 232 (1829).

[125] A. A. Demkov, Xiaodong Zhang and David Drabold, *submitted to* Phys. Rev. Lett.

[126] D. A. Drabold and P. A. Fedders, Phys. Rev. B **60**, R721 (1999).

[127] S. Aljishi, J. D. Cohen, and L. Ley, Phys. Rev. Lett. **64**, 2811 (1990).

[128] N. F. Mott and E. A. Davis, *Electronic processes in non-crystalline materials*, 2nd ed. (Clarendon, Oxford, 1979).

[129] V. I. Arkhipov and G. J. Adriaenssens, J. Non-Cryst. Sol. **227**, 166 (1998); Phys. Rev. B **54**, 16696 (1996).

[130] D. A. Drabold, S. Nakhmanson and X. Zhang, NATO ASI proceedings, M. Thorpe and L. Tichy, Eds., Kluwer (2000).

[131] D. A. Drabold, P. A. Fedders, S. Klemm and O. F. Sankey, Phys. Rev. Lett. **67**, 2179 (1991).

[132] D. A. Drabold, J. Non.-Cryst. Sol. **266**, 211 (2000).

[133] M. Cobb and D. A. Drabold, Phys. Rev. B **56**, 3054 (1997).

[134] X. Zhang and D. A. Drabold, Phys. Rev. Lett. **83**, 5042 (1999).

[135] P. Ordejon, D. A. Drabold and R. M. Martin, Phys. Rev. Lett. **75** 1324 (1995).

[136] http://www.phy.ohiou.edu/~drabold/fluctuate.html

[137] E. Gibbon, *The Decline and Fall of the Roman Empire*, abridged edition by D. M. Low, (Harcourt Brace, New York, 1960).

[138] D. A. Drabold in *Insulating and Semiconducting glasses*, Edited by P. Boolchand, World Scientific, Singapore (2000).

[139] See, for example P. Thomas and S. D. Baranovskii, J. Non-Cryst. Sol. **164**, 431 (1996) and references therein.

[140] R. E. Allen, Phys. Rev. B **50**, 18629 (1994).

[141] See for example, K. Thompson and T. J. Martinez, J. Chem. Phys. **110**, 1376 (1999) and references therein.

[142] P. M. Voyles, PhD thesis, University of Illinois at Urbana-Champaign, 2001 (unpublished)

Appendix A

Structure of electron states in a-Si and a-Se. Finite temperature

There is abundant experimental evidence that lattice vibrations play an important role in the dynamics of electrons in amorphous materials[126]. Among other examples, Cohen and coworkers [127] observed a pronounced temperature dependence of the Urbach tails in a-Si:H (the conduction tails showing a very strong linear variation in exponential decay parameter with temperature). Of course electrical conductivity is well known to be very temperature dependent, and usually has multiple distinct regimes according to different conduction mechanisms [128]. From this point of view it is unsurprising that the electron energies and states can be very time and temperature dependent. This point has been independently recognized by Arkhipov and Adriaennsens [129] in their studies of carrier transport. In this appendix we build a microscopic picture of these effects, beginning with a conventional discussion of electron-phonon coupling and the first explicit computation of this quantity[130].

We then work beyond the harmonic approximation and study the development of electronic states as a consequence of a thermal MD simulation. We show that the electronic eigenvalues *and eigenvectors* can be profoundly sensitive to lattice vibrations. Our calculations have the advantage of being rather realistic, but the problem that they are restricted to very short (picosecond) time scales.

A.1 Electron-phonon coupling: *ab initio* deformation potential

Earlier work of Drabold *et al.* has shown that it is useful to link the thermal fluctuation of the LDA energy eigenvalues near the band tails to the extent (localization) of the band tails in amorphous Si[131] (as separately measured in total yield photoemission experiments[127]). It is now routine in *ab initio* simulations to compute both the electronic and vibrational eigenvalues and eigenvectors. We show here that it is entirely straightforward to compute the electron-phonon coupling, a sort of "*ab initio* deformation potential"[132].

Consider a particular electronic eigenvalue, λ_n, say in one of the band tails in a-Si. To estimate the sensitivity of λ_n to a coordinate distortion (supposedly thermally induced), we can use the Hellmann-Feynman theorem[29], which gives $\partial\lambda_n/\partial\mathbf{R}_\alpha = \langle\psi_n|\partial\mathbf{H}/\partial\mathbf{R}_\alpha|\psi_n\rangle$ (for this to be valid, we must assume that the basis is fixed (not moving with the atoms) and that the $|\psi_n\rangle$ are exact eigenvectors of $\mathbf{H}$; see

Ref. [23] for a more general case). Then clearly for small distortions $\delta\mathbf{R}_\alpha$, we have

$$\delta\lambda_n \approx \sum_\alpha \langle\psi_n|\partial\mathbf{H}/\partial\mathbf{R}_\alpha|\psi_n\rangle\delta\mathbf{R}_\alpha. \tag{A.1}$$

Here, $\mathbf{R}$ is the $3N$ vector of displacements for all of the atomic coordinates from equilibrium. If the displacements $\delta\mathbf{R}_\alpha(t)$ arise from classical vibrations, then one can also write:

$$\delta\mathbf{R}_\alpha(t) = \sum_\omega A(T,\omega)\ \cos[\omega t + \phi_\omega]\ \chi_\alpha(\omega), \tag{A.2}$$

where ω indexes the normal mode frequencies, $A(T,\omega)$ is the temperature dependent amplitude of the mode with frequency ω, ϕ_ω is an arbitrary phase, and $\chi_\alpha(\omega)$ is a normal mode with frequency ω and vibrational displacement index α. Using a temperature dependent squared amplitude $A^2(T,\omega) = k_BT/2M\omega^2$, it is easy to see that the trajectory (long time) average of the expression for $\delta\lambda_n^2$ is:

$$\langle\delta\lambda_n^2\rangle \sim (k_BT/4M)\sum_\omega(\Xi(\omega)/\omega)^2, \tag{A.3}$$

where the electron[n]-lattice[ω] coupling $\Xi_n(\omega)$ is given by:

$$\Xi_n(\omega) = \sum_\alpha \langle\psi_n|\partial\mathbf{H}/\partial\mathbf{R}_\alpha|\psi_n\rangle\chi_\alpha(\omega). \tag{A.4}$$

It would be straightforward for a particular collection of vibrational states to include the correct Bose terms to obtain a result valid at low temperatures $T < \Theta_D$ (for Θ_D a salient Debye temperature). These formulas give a transparent expression for

the thermally induced electron modulation as driven by the lattice-electron coupling $\Xi_n(\omega)$. If we follow Ref. [131] and make the coarse approximation of equating $\langle \delta\lambda_n^2 \rangle^{1/2}$ to the Urbach decay parameter, then this model would predict a square root dependence of the decay parameter with temperature, perhaps not easily distinguished from the linear dependence reported in Ref. [127].

It is easy to see why there is a correlation between an eigenstate's localization (as measured for example by inverse participation ratio) and its thermal rms fluctuation[133]. Note that $\Xi_n(\omega)$ will in general consist of a sum of many terms (for different α); the individual terms have no preferred sign, so that adding a large number of terms of comparable magnitude will lead to cancellation and a small sum. On the other hand, if only a very small number of terms are nonzero (as for the case when the electron state $|\psi_n\rangle$ is well localized), then there will be less cancellation and a larger contribution to the sum (and therefore to the fluctuation of the eigenvalue). This model is limited in many ways: it is classical, it is obviously strictly harmonic, and we are assuming no electronic level crossings or other departures from adiabatic (Born-Oppenheimer) dynamics[126]). Nevertheless, this simple model captures some of the right temperature dependent electronic effects observed and provides a useful new link to *ab initio* simulation methods.

The thermal effects on the electron *states* are more difficult to calculate with this approach, mostly because of problems with degeneracy if one tries to use perturbation theory. Still, the underlying "physics" is quite simple, just the effects of resonant mixing for close approach (in energy) of eigenvalues originating in cluster states[68] with

some overlap in space. In the language of the model Hamiltonian above, this means that there can be large mixing of cluster basis states when the energy denominator becomes small; here the thermal fluctuations can induce small energy denominators (and therefore mixing). Of course a mixed state involves more cluster states than a pure cluster state, so that it is more spatially extended.

We have explicitly computed $\Xi_n(\omega)$ for 216 atom models of a-Si[52] (DTW216) and a-Se[134]. We used the method of Sankey and coworkers for the interatomic potential[23] to compute the dynamical matrix[63, 135] and estimated $\partial\lambda_n/\partial\mathbf{R}_\alpha$ from finite differencing λ_n for each of the 3N (small) displacements $\delta\mathbf{R}_\alpha$ needed for computing the dynamical matrix. $\Xi_n(\omega)$ is then easily obtained from Equation A.4. Our results are summarized for a-Si in Fig. A.1 and for a-Se in Fig. A.2.

For the case of DTW216 a-Si model there are no coordination defects, though there are a small number of strained structures which lead to a reasonable distribution of localized tail and gap states. Note that (1) the electron-phonon coupling is larger for conduction tail states than valence tail states (the conduction tails are also more localized), 2) the *acoustic* phonons are evidently more important to the tail states than optical phonons. This is also borne out by a dominant low frequency (eg acoustic) modulation of the tail electronic energies in the next section. 3) The electron-phonon coupling falls off rapidly for electron energies away from band edges.

The case of a-Se is largely similar except for one very interesting difference: the high energy "optical" phonons induce a large second "hump" in the surface plot (for phonon energies exceeding 200 cm^{-1}. In this model there is one valence alternation

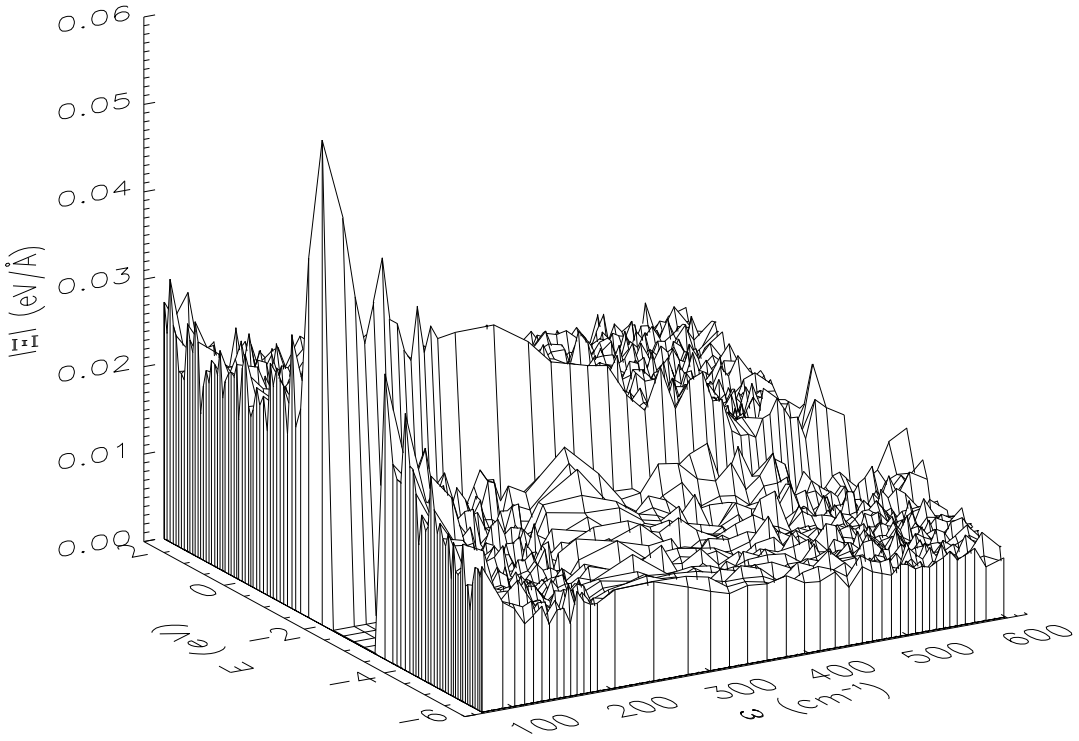

Figure A.1: **Electron-phonon coupling surface plot for 216 atom DTW model of amorphous Si. Phonon energy ω, electron energy E and absolute value of electron-phonon coupling Ξ (Equation A.4). The optical gap extends from -3.45 to -2.11 eV. Note the dominance of *acoustic* phonons to the coupling.**

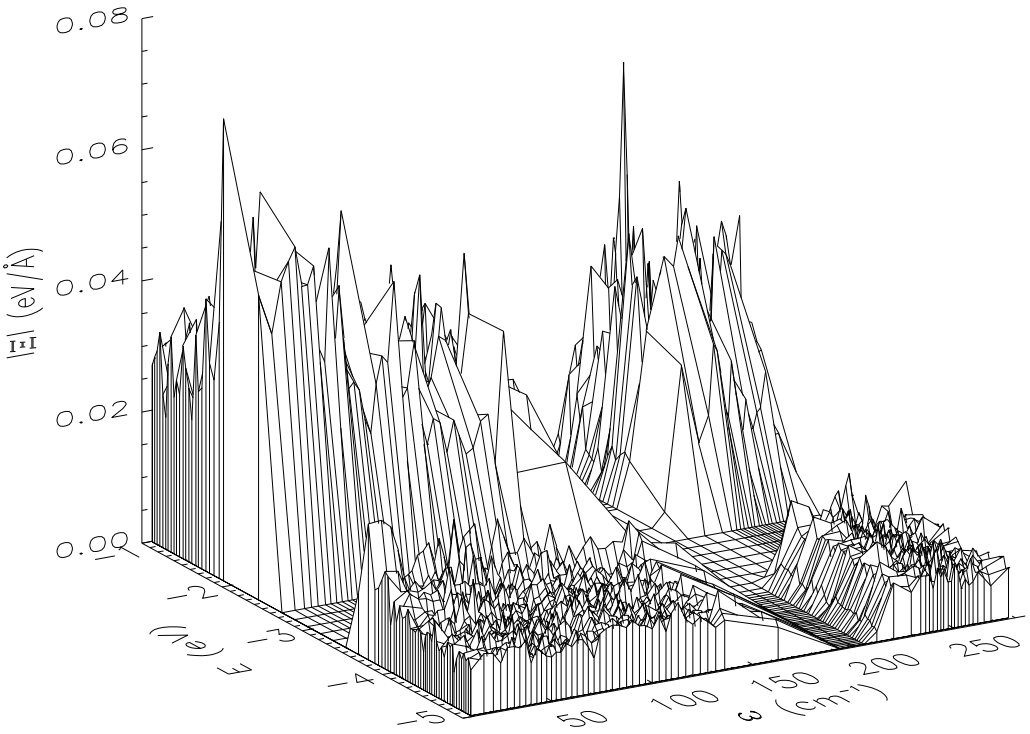

Figure A.2: **Electron-phonon coupling surface plot for 216 atom model of amorphous Se. Phonon energy ω, electron energy E and absolute value of electron-phonon coupling Ξ (Equation A.4). The optical gap extends from -3.63 to -2.50 eV. In contrast to a-Si, optical phonons play an important role in the electron-phonon coupling in Se.**

pair (threefold and onefold coordinated Se sites). It is possible that the spectacular photo-sensitivity of a-Se can be attributed in this framework to the simultaneous presence of localized electronic and vibrational modes *in the same region of space*, eg near the same defect. Note also that for a-Se, the conduction tail states (which derive mostly from positively charged threefold sites) are *much* better localized and exhibit a much larger electron-phonon coupling than the valence tail states. This large coupling is a primary reason for the photo-sensitivity of a-Se.

To directly estimate the fluctuations of the energy eigenvalues, we have evaluated Equation A.3 for the cases of both a-Si and a-Se using the $\Xi_n(\omega)$ as presented in Figures A.1 and A.2 (see Fig. A.3). The floppy nature of the Se network, and the strong emphasis of Equation A.3 on the *low frequency* phonons causes the rms variation of the localized energy eigenvalues to be very large (of order 3.0 eV for room temperature); this is obviously too large, and a consequence of the large number of floppy modes and expected anharmonic character of a-Se. The results for a-Si are very reasonable, and in semiquantitative agreement with the discussion of the next section.

A.2 Thermal MD simulation

An alternative approach which avoids the harmonic approximation is to study the thermal modulation of the eigenvalues and eigenvectors by tracking their (adiabatic) time development over the course of a few picosecond MD simulation. As illustrated

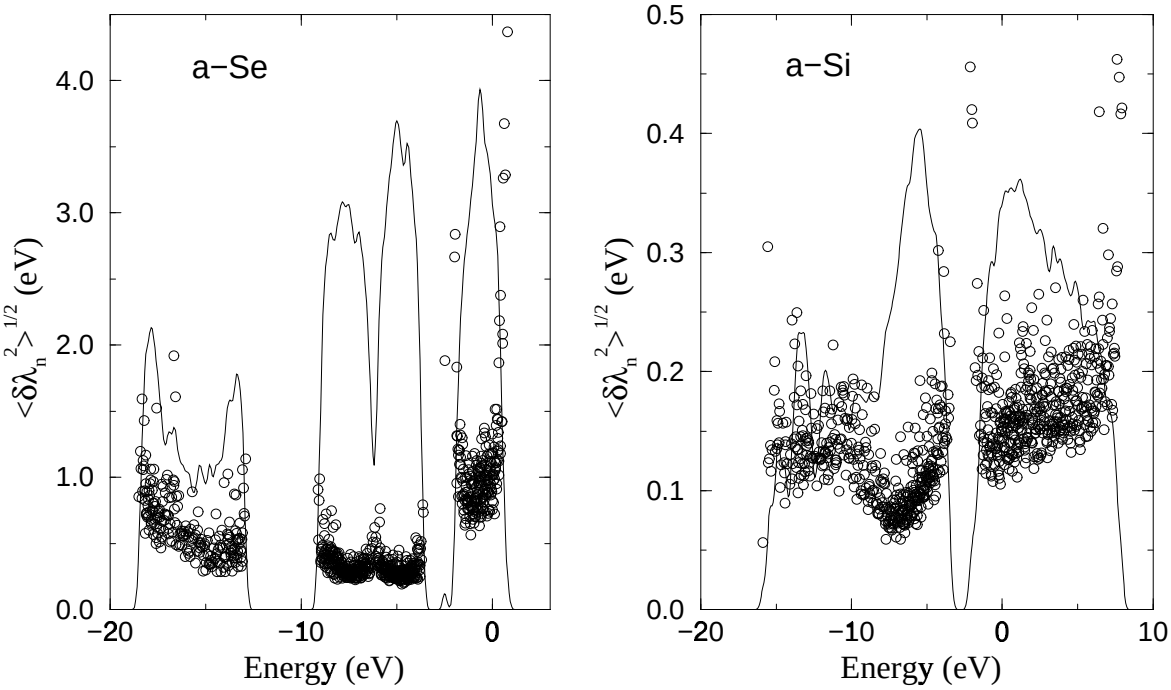

Figure A.3: **Crude estimates for RMS thermally-induced fluctuations in energy eigenvalues in the harmonic approximation from Equation A.3 (open circles). Left is for a-Se model, right a-Si; note the difference in scales of the vertical axes. The relevant states are near the optical gap (near -2.5eV for Se, near -3.0 for Si). Note the large fluctuations in the conduction tail states for a-Se, which probably arise from anharmonic vibrations in the floppy a-Se network. The electronic density of states for each system is depicted with the solid line.**

in Fig. A.4, there is strong time dependence of the LDA eigenvalues in the vicinity of the optical gap. The Fermi level is near the middle of the gap and several states near the Fermi level are appropriately described as bandtail states. These are much like the states which would be responsible for conduction in doped a-Si:H. As in earlier work of Drabold *et al.*[131] there is a roughly linear relation between rms temporal fluctuation and temperature. As expected, the higher temperature simulation leads to larger excursions in the positions of the energy eigenvalues. Note for 300K that the Lowest Unoccupied Molecular Orbital (LUMO) fluctuates in time by about $\sim$0.3eV, *much* larger than thermal energies ($\sim$10 meV). States deeper into either the valence or conduction bands show progressively less thermal modulation because they are less localized (Cobb and Drabold have noted[133] a very strong correlation between the rms fluctuation in the energy eigenvalues due to thermal disorder and the inverse participation ratio, a simple measure of localization in the T=0 model). The localization "amplifies" the electron-phonon coupling. Also, the conduction states fluctuate more than the valence states (suggesting that the conduction tails are more sensitive to thermal disorder than the valence tails which originate primarily from structural disorder), in pleasing agreement with total yield photoemission experiments[127] and earlier theory work[131]. We note that for a-Si, the harmonic approximation of the preceding section leads to semi-quantitative agreement with the rms fluctuations computed directly from the thermal simulations of this section. For amorphous Se, it is clear that the harmonic computation *overestimates* the electron-phonon coupling, this is not very surprising for the highly floppy a-Se network.

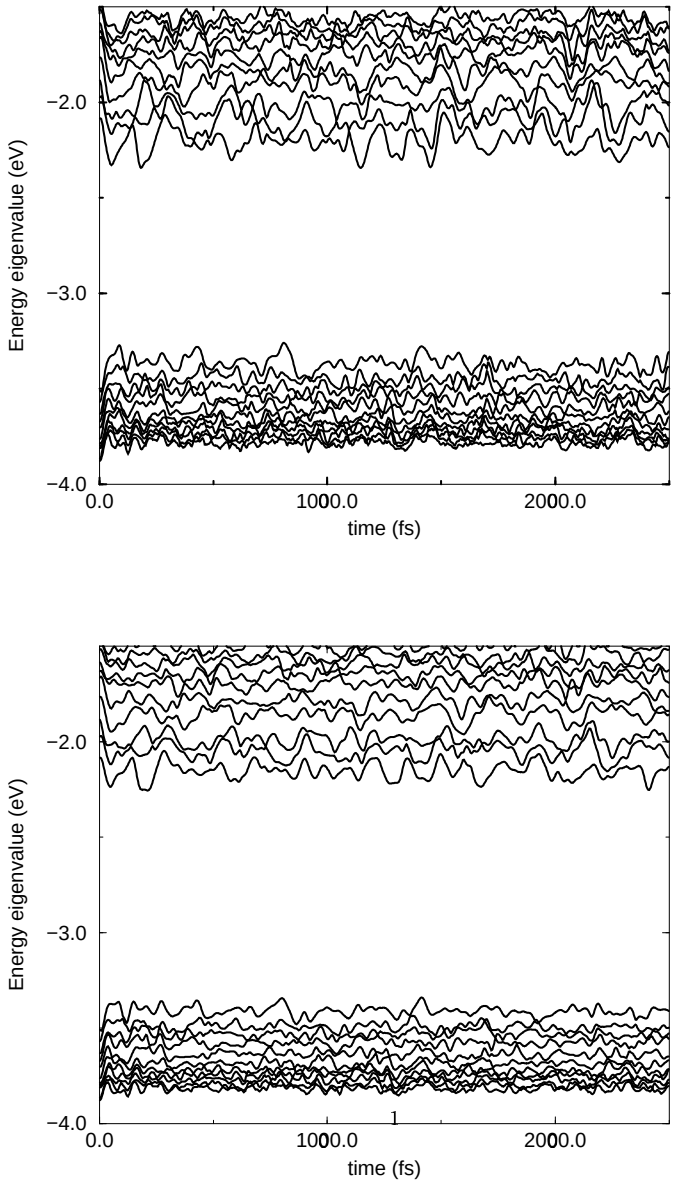

Figure A.4: **Adiabatic (Born-Oppenheimer) time evolution of LDA eigenvalues in 216 atom DTW model of a-Si. Top panel 300K, bottom panel 150K. Note the larger fluctuations in conduction tail states compared to valence edge states. The Fermi level is near -2.7 eV. Compare to Fig. A.1 and Fig. A.3.**

An additional point is that these thermal simulations lead to low energy (acoustic) modulation of the localized electron states (especially for the conduction tail) in agreement with the discussion of the preceding section. The importance of the low frequency vibrational modes is emphasized by the ω^{-2} factor in Equation A.3, also consistent with the very large predicted rms fluctuations in near-gap electron energies a-Se seen in the preceding section.

In Fig. A.5 we present snapshots of charge fluctuations in electron states near the gap for the system and dynamics described above. There are very substantial changes in the LUMO state in particular; there is a clear tendency for the LUMO state to alternately "accumulate" on a strained part of the network, sometimes becoming localized, but also occasionally developing a substantially more extended "stringlike" character. These are not the only two recognizable structures, but recur most frequently. The time between "characters" is not predictable, though it is of order tens to hundreds of fs. We have posted an animation of this state on the world wide web[136].

As we have pointed out before, structural disorder in a-Si gives rise to localized states with energies in the band tails[68]. These system eigenstates can involve *many* atoms and can have a Byzantine[137] structure. The "simple physics" of this study is that the strong (compared to mid-band electrons) electron-phonon coupling for localized band tail states *is sufficient* to cause strongly time/temperature dependent quantum mechanical mixing of cluster states when the thermal disorder is "just right" to make their energies nearly degenerate provided that they have some overlap in real

(a) A snaphot of the LUMO state:
time= 1147.5 fs

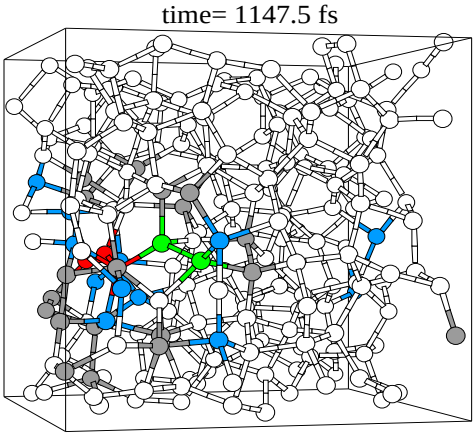

(b) A snaphot of the LUMO state:
time= 1032.5 fs

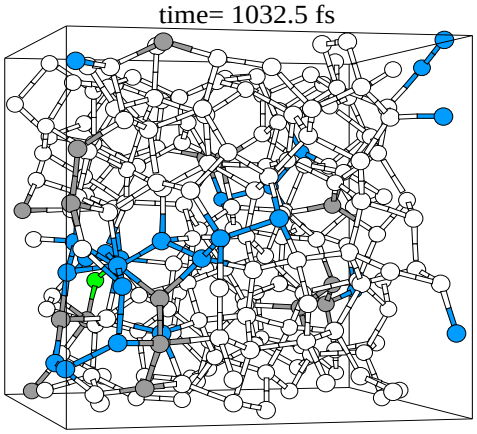

Figure A.5: **A representation of the LUMO energy eigenstate and the time dependence of its structure, as modulated by thermal disorder for DTW216 a-Si model from 300K simulation. Color coding reflects different amount of electron charge on a site: Red ($q > 0.1$), green ($0.05 < q < 0.1$), blue ($0.05 < q < 0.01$), grey($0.01 < q < 0.005$), white ($q < 0.005$). q is the total charge on the site. The charge summed over all sites is unity in all cases. Figs a and b are "snapshots" from the 2.5 ps simulation separated by about 100 fs. Fig. a — very localized compact cluster, Fig. b — much less localized "string"-like state.**

space. Strong mixing of course implies less localization and thus better prospects, at least while the more extended state survives, for conductivity and optical transitions. This work shows that transport and optical calculations based only on T=0 results can be quite misleading. Mott[128] and others have made fundamental contributions to the theory of transport in a noncrystalline medium; for example,variable range hopping. In the kind of simulation we present here, we can estimate the conductivity, including its temperature and frequency dependence *directly* from the electronic states through an appropriate thermal average of the Kubo formula[138]. It is also a complement to the phenomenological models of transport[129, 139]. In the latter work, transport is modeled as a hopping between localized tail states. Our work can be viewed as an explanation of the precise nature of the states among which electrons are hopping (the very complicated states of Ref. [68]). The waiting time between hops must be related to the time between eigenvalue "close encounters" near the Fermi level. It also points at an atomistic level to the dynamics of band tail defects and their kinetics.

The consequences of this work can be stated another way. If $|i\rangle$ ($|f\rangle$) are initial (final) electronic states with energy E_i (E_f), then for an electronic transition in a-Si, a Fermi golden rule argument leads quickly to the conclusion[128] that the transition rate is proportional to $|\langle i|\hat{T}|f\rangle|^2\delta(E_f - E_i - \hbar\omega)$, where $\hat{T}$ is a perturbation inducing the transition (to first approximation a momentum operator) and ω is the frequency of an external probe. Both the energies in the δ function and the transition matrix elements are affected by the instantaneous details of the structural disorder, and as

such transition probabilities are also strongly dependent on the time and temperature. The consequences of this to transport are under investigation; the discussion here is based upon first-order time dependent perturbation theory, which for the very strong electron-phonon coupling we discuss, could be inadequate.

A.3 Post adiabatic atomic dynamics — speculations for future work

The calculations and discussion of the preceding sections has been based on the adiabatic approximation (that the electrons are always in their instantaneous ground state determined by the external potential (eg the atomic nuclei), and that the forces "felt" by the nuclei arose from the instantaneous electronic structure of the system.

To see that this might be an imperfect assumption, consider a doped system with a small concentration of dopants for which the Fermi level is pushed into one one of the band tails. Then the thermal modulation of the atomic coordinates may produce level crossings or close approaches of the LDA energies. In the doped case, there would normally be (occupied) levels below the Fermi energy and (unoccupied) levels above. In the case of a level crossing at the Fermi level, the adiabatic approximation would immediately transfer charge from one state to another (even if spatially remote), which would induce changes in the dynamics (since the levels with changed occupation would typically be at least somewhat localized); and perhaps could lead to a structural change, even a long lived change if the new structure was

"self-trapping". In practical calculations such charge transfer would not have be quite so large an affect, since one would usually smear the Fermi function slightly from the $T = 0$ Heaviside step form. The dynamics are then affected by such level crossings or close approaches even in the adiabatic approximation. A better theory[140] is due to Allen, in which interatomic forces are computed from mixed state wave functions obtained by a direct integration of the *time-dependent* Schrödinger equation (rather than the "pure" states computed anew at each new time step for the atomic dynamics in the adiabatic picture). This approach was formulated to model the dynamical response of a system to light (in which the simplest model of light-solid interactions would just involve promotions of electrons to low-lying conduction states), but the formalism is similar (and much simpler) for the case of purely phonon-induced level crossings as in our problem. It is possible in fact that the adiabatic approximation may often be satisfactory for this kind of problem, but the question has not yet been properly investigated because of difficulties with post-adiabatic calculations. One case for which nonadiabatic dynamics is *essential* is in the modeling of the thermalization of excited carriers to tail states. This process has never been realistically modeled despite its manifest importance to a host of problems in crystalline and non-crystalline semiconductor physics. More sophisticated methods for non-adiabatic dynamics are discussed in the quantum chemistry literature[141]; while fundamentally sound, these are currently too difficult to implement for the large model systems we must consider here.

Appendix B

Introduction to fluctuation electron microscopy

We have based this short introduction on the materials presented in the dissertation of P. M. Voyles (see Ref. [142]) which gives an exhaustive description of fluctuation electron microscopy theory and experimental techniques.

As we already know from subsection 3.2.1 of this dissertation the X-ray diffraction provides us information about atomic position correlations in a material by measuring the radial-distribution or pair-correlation function $g_2(r)$ for it[2, 3]. In a disordered material like a-Si $g_2(r)$ gives us useful knowledge of material's structure only for $r \leq 8$Å but at distances beyond that it becomes featureless (see, for example, Fig. 5.3). If we are interested in studying the traces of ordering in such material that have length scales lying between the short-range order (6–8Å) and long-range disorder (hundreds of angstroms) — we call this length scale interval medium-range order (MRO) — we need a different experimental technique able of measuring position-correlation

functions of higher order, like $g_3(r_1, r_2)$ and $g_4(r_1, r_2, r_3)$, which could obviously be a much richer source of information on the structure (and consequently probable ordering) of the material than $g_2(r)$.

The technique possessing such capabilities already exists and is called fluctuation electron microscopy (FEM)[10, 11]. In FEM the information related to $g_3(r_1, r_2)$ and $g_4(r_1, r_2, r_3)$ can be extracted by statistical analysis of low-resolution, hollow-cone dark-field (HCDF) transmission electron microscopy (TEM) micrographs. A "dark-field" image is formed only by electrons scattered by the sample through a particular diffraction vector $\vec{k}$. Low-resolution means that the resolution of the microscope is relatively low compared to both the characteristic interatomic distances in the material and to the resolution limit of the microscope. In a dark-field technique volumes of the sample diffracting strongly at vector $\vec{k}$ will show up as bright areas in the image, while volumes diffracting weakly will be dim. To make sure that only the diffracted radiation continues down the microscope's optic axis to the recording device in a TEM the electron beam is tilted with respect to the surface of the sample and the angle of the tilt governs the diffraction condition for vector $\vec{k}$. In the hollow-cone illumination mode the tilted beam is swung in a cone with constant inner angle which helps to reduce the effect of random long-range atomic correlations. The low microscope resolution is used in search for MRO with FEM because when looking for presence of ordered structures in the material at some certain length scales it is better to match the resolution with the characteristic size of the ordered structure one is trying to find (10–15Å in recent experiments for a-Si).

The value measured in the FEM experiments is the image intensity $I(k, Q)$ at the hollow-cone vector magnitude k and the microscope resolution $0.61/Q$. In the HCDF microscopy theory this value depends on the incoming illumination, the effects of the microscope and the sample structure described with function $g_2(r)$.

A simple statistical measure which is sensitive to MRO and can be computed using diffraction intensities $I(k, Q)$ is the normalized variance

$$V(k, Q) = \frac{\langle I^2(k, Q) \rangle}{\langle I(k, Q) \rangle^2} - 1,$$

where $\langle \ \rangle$ indicates averaging over the image. In this formula $I^2(k, Q)$ represents a measure of the fluctuations in the diffracted intensity and depends not only on $g_2(r)$ but also on the higher order correlation functions $g_3(r_1, r_2)$ and $g_4(r_1, r_2, r_3)$ which contain information about MRO.

To gain basic understanding how $V(k, Q)$ is sensitive to MRO we can conduct a simple imaginary experiment. Let's first consider a sample consisting of a random assortment of atoms. In such a sample each mesoscopic volume will have a statistically similar structure and hence a similar diffraction intensity. This will produce an image with a low normalized variance with little structure in k or Q since there are no characteristic length scales in the sample. Then let's consider a sample consisting of randomly oriented ordered clusters of atoms. Obviously for some of the cluster orientations the Bragg diffraction condition will be satisfied and these clusters will diffract very strongly, leading to a bright spot in the image. Some other clusters will be far away from the Bragg condition and will diffract very weakly (weaker than

average), which will lead to a very dark spot in the image. Overall, the image will have high variance with relatively large excursions away from the mean value. The variance will also show structure in k as k passes through various extremums in the structure factor of the clusters and also structure in Q as more and more of each cluster and the groups of clusters are sampled by a particular resolution.

Of course, the qualitative picture presented above is an oversimplification but the general rule can be applied for real experimental data: low variance with little structure in k or Q is the sign of little or no MRO while high variance with significant structure in k or Q is the sign of MRO presence.

Finally, it would be useful to make a note about two different "flavors" of the FEM experimental setup. In the first type of setup, called variable coherence microscopy, $V(k)$ is estimated at constant resolution Q which gives information on the degree of MRO in the sample (at a given resolution). In the second setup variant, called variable resolution microscopy, $V(Q)$ is evaluated at fixed diffraction vector k (fixed beam tilt angle) which provides information about characteristic MRO length scales in the material. Technically the former variant is much easier to implement because the beam tilt can be changed electronically while the change of microscope objective aperture, that can be done mechanically, is a much more challenging engineering task.

Appendix C

Related publications

[1] S. Nakhmanson and D. A. Drabold, *Approximate ab initio calculation of vibrational properties of hydrogenated amorphous silicon with inner voids,* Phys. Rev. **B 58** 15325 (1998). [chapter 4]

[2] P. A. Fedders, D. A. Drabold and S. Nakhmanson, *Theoretical study on the nature of band-tail states in amorphous Si,* Phys. Rev. **B 58** 15624 (1998).

[3] D. A. Drabold, U. Stephan, J. Dong and S. Nakhmanson, *Electronic structure of amorphous silicon,* J. Mol. Graphics Mod. **17,** 285, (1999). [Appendix A]

[4] S. Nakhmanson and D. A. Drabold, *Computer simulation of low-energy excitations in amorphous silicon with voids,* J. Non. Cryst. Sol. **266-269** 156 (2000). [chapter 4]

[5] S. Nakhmanson and D. A. Drabold, *Low-temperature anomalous specific heat without tunneling modes: a simulation for a-Si with voids,* Phys. Rev. **B 61** 5376 (2000). [chapter 4]

[6] D. A. Drabold, S. Nakhmanson and X. Zhang, *Electronic structure of amorphous insulators and photostructural effects in chalcogenide glasses,* NATO ASI proceedings, M. Thorpe and L. Tichy, Eds., Kluwer (2000). [Appendix A]

[7] P. M. Voyles, N. Zotov, S. M. Nakhmanson, D. A. Drabold, J. M. Gibson, M. M. J. Treacy, P. J. Keblinski, *The Structure and Physical Properties of Paracrystalline Atomistic Models of Amorphous Silicon,* Submitted to J. Appl. Phys. (Sep 2000). [chapter 5]

[8] S. Nakhmanson, N. Mousseau, G. T. Barkema, P. M. Voyles and D. A. Drabold, *Models of Paracrystalline Silicon with a Defect-Free Bandgap,* to appear in Intl. J. Mod. Phys. (Sep 2000). [chapter 5]

[9] S. Nakhmanson, P. M. Voyles, N. Mousseau, G. T. Barkema and D. A. Drabold, *Realistic Models of Paracrystalline Silicon,* Submitted to Phys. Rev. B (Jan 2001). [chapter 5]